Nano-Micro Letters

e-ISSN 2150-5551
CN 31-2103/TB

REVIEW

https://doi.org/10.1007/s40820-025-01772-7

Cite as
Nano-Micro Lett.
(2025) 17:275

Received: 28 January 2025
Accepted: 16 April 2025
© The Author(s) 2025

Advances in Metal Halide Perovskite Scintillators for X-Ray Detection

Ting Wang[1], Guoqiang Zeng[3], Yang Michael Yang[6], Zhi Yang[5], Tianchi Wang[4], Hao Li[4], Lulu Han[4], Xue Yu[7], Xuhui Xu[4] ✉, Xiaoping Ouyang[2] ✉

HIGHLIGHTS

- The review highlights recent advancements in enhancing the intrinsic physical properties of metal halide perovskite scintillators, such as improving light yield and response times, to improve their X-ray detection performance.
- It discusses innovative engineering strategies to effectively optimize radioluminescent light management for high-resolution X-ray imaging.
- The problems encountered in the application of metal halides perovskites materials for X-ray detection are summarized, and the potential development direction in the future is prospected.

ABSTRACT The relentless pursuit of advanced X-ray detection technologies has been significantly bolstered by the emergence of metal halides perovskites (MHPs) and their derivatives, which possess remarkable light yield and X-ray sensitivity. This comprehensive review delves into cutting-edge approaches for optimizing MHP scintillators performances by enhancing intrinsic physical properties and employing engineering radioluminescent (RL) light strategies, underscoring their potential for developing materials with superior high-resolution X-ray detection and imaging capabilities. We initially explore into recent research focused on strategies to effectively engineer the intrinsic physical properties of MHP scintillators, including light yield and response times. Additionally, we explore innovative engineering strategies involving stacked structures, waveguide effects, chiral circularly polarized luminescence, increased transparency, and the fabrication of flexile MHP scintillators, all of which effectively manage the RL light to achieve high-resolution and high-contrast X-ray imaging. Finally, we provide a roadmap for advancing next-generation MHP scintillators, highlighting their transformative potential in high-performance X-ray detection systems.

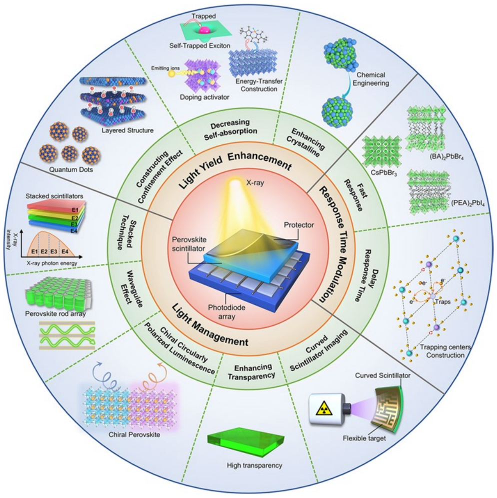

KEYWORDS Metal halide perovskites; X-ray detection; Scintillators; Radioluminescence properties; Engineering strategies

---

✉ Xuhui Xu, xuxuh07@126.com; Xiaoping Ouyang, oyxp2003@aliyun.com
[1] College of Materials and Chemistry & Chemical Engineering, Nuclear Technology Key Laboratory of Earth Science, Chengdu University of Technology, Chengdu 610059, People's Republic of China
[2] State Key Laboratory of Intense Pulsed Radiation Simulation and Effect, Northwest Institute of Nuclear Technology, Xi'an 710024, People's Republic of China
[3] Nuclear Technology Key Laboratory of Earth Science, Chengdu University of Technology, Chengdu 610059, People's Republic of China
[4] Faculty of Materials Science and Engineering, Key Laboratory of Advanced Materials of Yunnan Province, Kunming University of Science and Technology, Kunming 650093, People's Republic of China
[5] Key Laboratory of Materials Physics of Ministry of Education, Laboratory of Zhongyuan Light, School of Physics, Zhengzhou University, Zhengzhou 450051, People's Republic of China
[6] State Key Laboratory of Modern Optical Instrumentation, Institute for Advanced Photonics, College of Optical Science and Engineering, Zhejiang University, Hangzhou 310027, People's Republic of China
[7] School of Mechanical Engineering, Institute for Advanced Materials, Chengdu University, Chengdu 610106, People's Republic of China

Published online: 23 May 2025

1 Introduction

The imperative for sophisticated X-ray detection technologies has never been more critical, with applications spanning the realms of medical imaging, security surveillance, scientific research, and industrial non-destructive testing [1, 2] Based on their detection mechanisms, X-ray detectors are broadly categorized into direct and indirect types. Direct detectors use semiconductors to immediately convert X-rays into electrical signals, whereas indirect systems employ scintillators to first transform X-rays into visible light, then detected by photodetectors [3]. Despite faster response times in direct detection, indirect detectors dominate commercial applications use due to their higher efficiency, better stability, and lower costs [4–7]. In the realm of scintillators, however, traditional scintillators each have limitations that hinder their effectiveness across the practical applications. For instance, columnar CsI: Tl is commonly utilized in medical radiography for its high light yield and good resolution [8, 9], but its hygroscopic nature can degrade performance over time. Ceramic Gd_2O_2S (GOS), used in X-ray computed tomography (CT), offers high light output and stability [10–13], but has a relatively long decay time and can be costly to produce, limiting its use in cost-sensitive applications. Similarly, single crystalline $Lu_{1.8}Y_{0.2}SiO_5$:Ce (LYSO: Ce) is favored in positron emission tomography (PET) for its high light yield and fast decay time [14, 15], yet it is expensive and challenging to grow in large, defect-free crystals, affecting its widespread adoption. These limitations underscore the need for ongoing research and development to create new scintillator materials that better meet the diverse demands of various imaging applications. The evolving demand for detecting intricate structures, high-precision equipment, irregular geometries, and efficiently storing imaging information necessitates the development of scintillators with exceptional characteristics. Therefore, developing novel scintillators with high light yield, high resolution, tunable response time, and adaptability is essential for pushing the boundaries of X-ray detection technology and for broadening their application scope.

Metal halide perovskites (MHP), with their exceptional optical properties and unparalleled X-ray detection capabilities, have risen to prominence as the forefront of scintillation materials. This is attributed to their high effective atomic number (Z_{eff}) and near-unity luminescence efficiency [16, 17], which can be demonstrated by comparing the scintillation properties of commonly used materials and the recently reported MHPs (Table 1). The journey of perovskite materials in X-ray applications began in 2002 with the introduction of the hybrid organic–inorganic perovskite $(C_6H_{13}NH_3)_2PbI_4$, by Shibuya et al. [18]. Fast forward to 2016, Birowosuto et al. [19] discovered a MHP material with an unprecedented light yield of up to 120,000 Ph MeV^{-1}, setting a new benchmark for efficiency in scintillation-based radiation detection. Subsequently, a series of studies have been reported on optimizing the light yield, timing, and detected resolution of MHP scintillators [20–23]. The ability to tailor MHP properties through meticulous compositional adjustments and structural engineering has since opened up unprecedented opportunities for enhancing detection performance across a spectrum of modalities [24–27]. More importantly, researchers have been able to flexibly manipulate the bandgap, decay kinetics, and improve the stability of these materials, making them more viable for practical applications in medical imaging, security systems, and industrial inspection [28–30].

Numerous reviews have explored methods to enhance the performance of MHP scintillators for X-ray detection, focusing on aspects such as imaging resolution and detection limits [50]. These reviews often emphasize optimizing the light yield of the scintillators. However, improving intrinsic properties like light yield alone is not sufficient. The response time, another critical intrinsic property, plays a vital role in determining the effectiveness of X-ray detection, impacting both real-time and delayed detection capabilities. Additionally, the design and implementation of engineering techniques for effective radioluminescent (RL) management, encompassing the optimal collection and transmission of the light signals generated by the scintillators, are crucial for maximizing the detector's overall performance. Therefore, a comprehensive overview of the cutting-edge advancements and strategic approaches, integrating both the intrinsic physical properties and RL engineering techniques, is urgently needed to summarize current research progress and explore future prospects in this field.

This review begins with an elucidation of the MHP scintillation mechanism and the fundamental requirements of scintillators. It then summarizes recent research focused on strategies to effectively engineer the intrinsic physical

© The authors

https://doi.org/10.1007/s40820-025-01772-7

Table 1 RL peak, density, light yield, decay time, spatial resolution, and detection limit for commonly used scintillator materials

Scintillators	Emission peak (nm)	Density (g cm^{-3})	Light yield (Ph Mev^{-1})	Decay time (ns)	Spatial resolution (lp mm^{-1})	Detection limit (nGy$_{air}$ s^{-1})	References
$Bi_3Ge_3O_{12}$(BGO)	480	7.13	8,500	300	11	376	[31–33]
Lu_2SiO_5(LYSO)	420	7.4	29,000	40	3.8	1.33×10^4	[33–35]
Gd_2O_2S: Eu	610	6.7	60,000	1×10^6	–	–	[12]
CsI: TI	470	4.51	65,000	10^3	10	180	[9, 31]
$Y_3Al_5O_{12}$: Ce	550	4.57	46,400	70	–	–	[36]
$CsPbBr_3$	520	4.55	26,000	5.97	12.5	120	[37, 38]
$(BA)_2PbBr_4$	427	4.05	7,900	2.52	–	318.3	[29, 39]
$(BA)_2(Pb_{0.9}Mn_{0.1})Br_4$	618	4.05	85,000	7.28×10^5	10.7	16	[40]
$Cs_3Cu_2I_5$	445	5.6	127,376	9.6×10^2	17	48.6	[39, 41]
$CsCu_2I_3$	570	5.01	36,000	110	15.6	88.9	[42, 43]
Rb_2CuBr_3	385	5.97	91,056	4.14×10^7	27.9	63	[4, 40]
Cs_2AgI_3:Cu(I)	470	4.62	82,900	192.8	16.2	77.8	[33, 41]
$(BPTP)_2MnBr_4$	515	1.684	136,000	3.18×10^5	10.1	282	[44]
$(C_8H_{20}N)_2Cu_2Br_4$	468	1.944	91,300	5.6×10^4	9.5	52.1	[45, 46]
$(C_{25}H_{22}P)_2MnBr_4$	512	1.586	78,937	3.3×10^5	25.6	108.2	[4, 47]
Cs_2ZrCl_6	447	3.94	49,400	1.56×10^6	18	65	[48, 49]
Cs_2ZrCl_6: Lu^{3+}	460/90	3.94	94,190	9.0×10^4	17.2	15.8	[23]

properties of MHP scintillators, such as enhancing light yield and optimizing response times. These light yield enhanced strategies are summarized, which include optimizing crystallinity, constructing confinement effects to reduce non-radiative recombination pathways, suppressing self-absorption by exploiting self-trapped exciton (STE) emission, doping with emitting centers, and constructing an energy transfer (ET) channel. Additionally, the pivotal role of response time modulation in scintillators elucidates its impact on the dynamics of response and the overall effectiveness of detection systems, and details how the modulation of decay times can be tailored to meet the demands of various applications, from high-speed imaging to long-term radiation detection. Furthermore, the pursuit of high-resolution X-ray detection has driven the development of innovative engineering techniques, such as the construction of stacked imaging, waveguide effects, chiral circularly polarized luminescence (CPL), and the improvement in transparency. The emergence of flexible scintillators has further expanded the applicability of X-ray detection technologies, enabling conformal imaging on curved surfaces and in hard-to-reach areas. Ultimately, the review delineates the prevailing challenges and offers insightful perspectives for the future evolution and applications of MHP scintillators.

2 Mechanism of MHP Scintillators

In indirect-type X-ray detectors, scintillators serve as critical photon transducers that convert high-energy X-ray photons into detectable ultraviolet/visible photons through three sequential processes: X-ray-to-light conversion, charge transport dynamics, and radiative luminescence (Fig. 1a). This section systematically summarizes the fundamental mechanisms governing MHP-based scintillator operation.

Scintillation Process Fundamentals. Under X-ray irradiation, the first process in MHP scintillation involves the interaction of incident radiation with the scintillator. X-rays interact with matter through a number of physical processes including photoelectric effects, Compton scattering, and pair production [51]. At energies below several hundred keV, photoelectric absorption typically prevails. Conversely, beyond this range, Compton scattering becomes the dominant mechanism, wherein incident high-energy photons impart a fraction of their energy to the material. During photoelectric absorption, electrons in the inner shells of atoms are excited and ejected, leaving the atom ionized. Subsequently, an intricate electron–hole multiplication process occurs, involving secondary X-ray emission, Auger non-radiative decays, and inelastic electron scattering. When the photon energy exceeds 1.02 MeV, electron–positron pairs will be generated. Below this threshold, electrons primarily lose energy through Coulomb scattering. Electron–electron scattering and Auger processes generate a large number of secondary electrons, leading to the creation of charge carriers with lower kinetic energy. Subsequently, the energy of these charge carriers is thermally dissipated through interacting with the phonons. During this process, numerous low-kinetic energy electrons and holes gradually accumulate at the conduction band and valence band, respectively. In the second stage, the generated electron and hole migrate toward luminescent centers, transferring energy in the process. This stage, referred to as the transport stage, spans nanoseconds to picoseconds (10^{-9}–10^{-12} s). During the transport stage, the migrating charge carriers can be captured by defects in the scintillator such as ionic vacancies and grain boundaries or self-trapped in the crystal lattice, thus leading to non-radiative losses and possibly radiative recombination delay. This final stage involves the emission of scintillation photons. The stored energy in excited states is released via radiative emission or non-radiative decay. Radiative photon emission can occur via the recombination of electrons and holes with luminescent ions. Finally, the emitted light can then be detected and measured using various techniques, such as photomultiplier tubes, photodiodes, or charge-coupled devices (CCDs). The intensity and wavelength of the emitted light can provide information about the type and energy of the incident radiation, as well as the properties of the MHP scintillator. Here, four predominant luminescence mechanisms in MHPs are illustrated in Fig. 1b–e: exciton recombination, STE emission, thermally activated delayed fluorescence (TADF), and long-persistent radiative luminescence (LPRL).

Exciton Recombination. Exciton recombination is one of the most common luminescence mechanisms in MHPs. When perovskite materials are excited by X-rays, electrons are promoted from the valence band to the conduction band, forming electron–hole pairs, known as excitons. These excitons migrate within the material and eventually release energy through a radiative recombination process, emitting photons (Fig. 1b).

STE emission. STE are a luminescence mechanism commonly observed in soft lattice perovskites. In this process, when a material is excited by X-rays, electrons and holes are generated. Instead of forming free excitons, these charge carriers can become localized in a distorted local lattice environment, forming a bound state with lower energy. This localization enhances the overlap of the electron and hole wavefunctions, leading to longer lifetimes and broader emission spectra (Fig. 1c).

TADF emission. TADF is a special luminescence mechanism where triplet excitons are converted to singlet excitons through a process called Reverse Intersystem Crossing (RISC). In MHPs, TADF is observed in systems with a narrow singlet–triplet energy gap (Δ_{EST}), such as Zr-based variants. When the material is excited by X-rays, electrons are promoted from the ground state (S_0) to the excited singlet state (S_1). The excited singlet state (S_1) can undergo intersystem crossing to form a triplet state (T_1). This non-radiative process involves a spin-state transition of the electron. Subsequently, the triplet state (T_1) can be thermally activated to return to the singlet state (S_1) through reverse intersystem crossing (RISC). This process is facilitated by the small energy difference between the triplet and singlet states. Finally, the singlet state (S_1) formed through RISC can then undergo radiative recombination, emitting a photon and returning to the ground state (S_0) (Fig. 1d).

LPRL emission. LPRL is a phenomenon where a material continues to emit light for a prolonged period after the X-ray source is removed. This luminescence mechanism is typically associated with defect states or trap states of the perovskites. When the material is excited by X-rays, electrons are promoted from the valence band to the conduction band, forming electron–hole pairs (excitons). Some of these excitons are captured by trap states, acting as trapping centers, within the material. The trapped excitons remain in these trapping centers for a significant period, which can range from seconds to hours. The depth and number of trapping centers determine the duration of the energy storage. Deeper and more numerous trap states can lead to longer persistence times. Over time, the trapped excitons can be thermally activated, meaning they gain enough energy to escape from the trapping centers. Once the excitons escape from the trap states, they can return to the valence band through radiative recombination, thereby emitting persistent luminescence (Fig. 1e).

3 Intrinsic Physical Properties Modulation

Light yield and response time, as the core performance parameters of scintillators, critically determine the spatial resolution and detection limit of X-ray imaging [52]. Light yield, which reflects the efficiency of converting X-ray

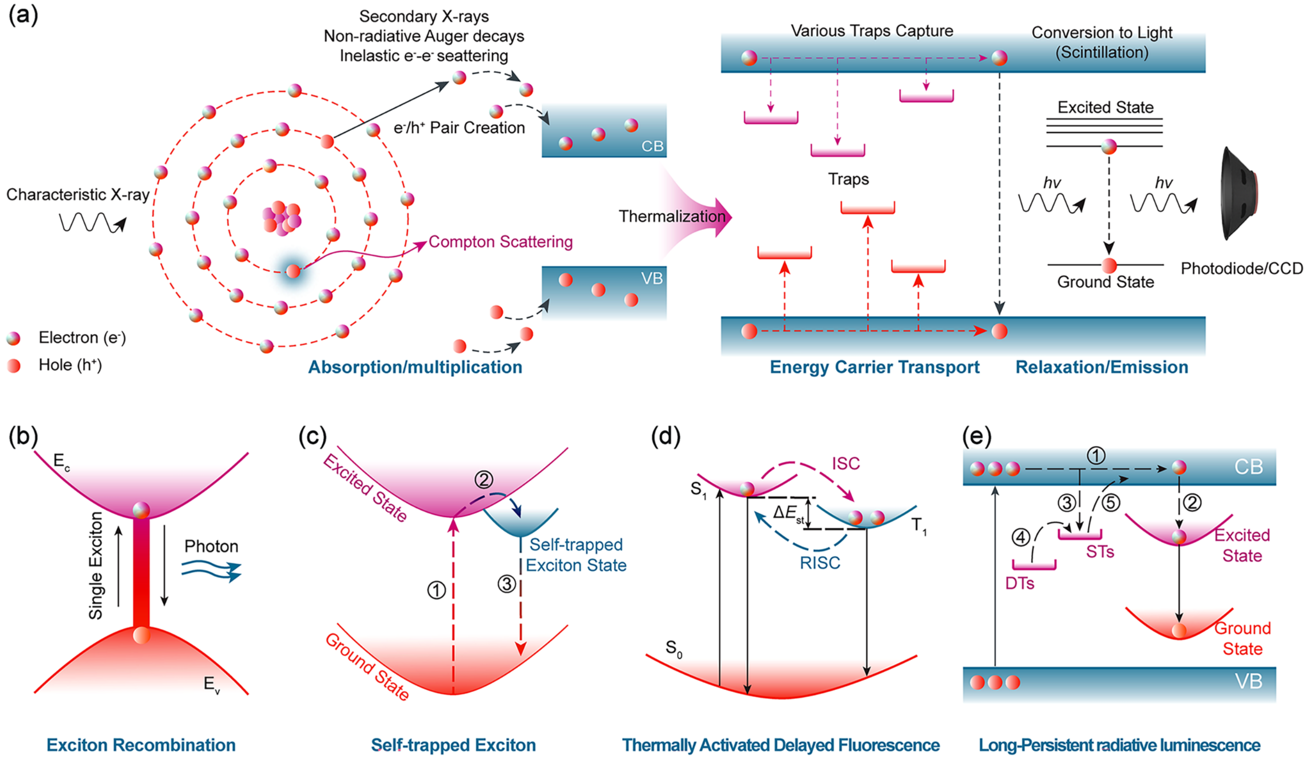

Fig. 1 Mechanism of MHP Scintillators for X-ray Detection. **a** Three-stage scintillation processes: conversion of X-rays to UV/visible photons, transport of charge carriers, and luminescence via radiative recombination. **b** Exciton recombination mechanism: Excitons formed by electron–hole pairs migrate and emit photons upon recombination. **c** STE emission: Electrons and holes localize in a distorted lattice, forming a low-energy bound state that leads to longer lifetimes and broader emission. **d** TADF emission: Triplet excitons convert to singlet states via RISC, resulting in delayed radiative emission. **e** LPRL emission: Excitons are captured by trap states and released over time through thermal activation, leading to persistent radiative emission

energy into visible light, directly enhances the signal-to-noise ratio (SNR) of imaging systems by reducing statistical noise, thereby improving spatial resolution. For instance, in medical CT scans, higher light yield enables the identification of microtumors or microcalcifications in soft tissues. Simultaneously, elevated light yield lowers the detection limit, allowing the system to capture low-dose X-ray signals, which is vital for radiation-sensitive applications such as mammography and pediatric imaging. Response time, governing the decay rate of scintillation emission, refers to how quickly the scintillator can emit light after absorbing X-ray energy. A fast response ensures image clarity in real-time angiography or high-speed industrial CT scans. Moreover, rapid response time enhances detection sensitivity by enabling precise temporal discrimination between weak signals and background noise, making it indispensable for time-resolved X-ray fluorescence imaging or transient process studies, such as in operando observations of battery charging/discharging. Therefore, by synergistically optimizing light yield and response time, next-generation scintillators can meet the dual requirements of emerging technologies like photon-counting CT (enabling energy discrimination and multispectral imaging), X-ray fluorescence tracking (trace element detection), and real-time industrial inspection (e.g., 3D printing process monitoring). In this section, we focus on strategies for enhancing light yield and modulating response time, aiming to optimize these intrinsic properties to meet the demands of advanced X-ray imaging technologies.

3.1 Light Yield Enhancement

The pursuit of enhanced light yield in MHPs represents a critical pathway toward high-sensitivity X-ray detection. The light yield quantifies the efficiency of converting absorbed radiation energy into detectable light.

Specifically, it measures the yield of UV/Visible photons for every unit of energy absorbed, a critical factor for scintillator performance. Typically, the yield of UV/Visible photons, denoted as N_{ph}, generated during the scintillation process for each incoming X-ray photon's energy E, is quantified using following equation: $N_{\mathrm{ph}} = (E/\beta E_{\mathrm{gap}}) \times SQ$ [53], which takes into account the scintillator band gap (E_{gap}), the transmission efficiency of electron–hole pair energy to the luminescent center (S), and the quantum efficiency (Q) [51]. Besides, the parameter β, which represents the average energy required to generate one electron–hole pair, proves in a range of 2–3 in most scintillator. MHPs exhibit inherent advantages for light yield optimization compared to conventional scintillators, as evidenced by their narrow bandgaps (1.5–3.2 eV) versus $LaBr_3$ (5.90 eV), $Bi_4Ge_3O_{12}$ (4.9 eV), NaI (3.9 eV), and CsI (5.14 eV). The inverse correlation between bandgap and theoretical light yield suggests extraordinary potential (129,000–250,000 Ph MeV^{-1}) [54], yet practical achievements remain constrained by several challenges, such as non-radiative recombination losses, obvious self-absorption processes with the crystals, optical loss during optical transmission process, etc. Recent advances address these limitations through three key approaches [1, 16, 55]: implementing confinement effects to enhance photon emission, increasing Stokes shift to minimize self-absorption, and enhancing crystallization to suppress non-radiative pathways.

3.1.1 Constructing Confinement Effect

The strategic construction of confinement effects has proven effective for enhancing light yield in MHP scintillators. By spatially localizing excitons and suppressing non-radiative recombination, confinement engineering significantly improves radiative efficiency. Two primary strategies are widely adopted: (1) synthesizing MHP nanocrystals (NCs) or quantum dots (QDs) to exploit quantum confinement and (2) designing layered perovskite structures to decouple light absorption and emission processes. This section systematically examines these strategies and their transformative impact on MHP scintillator performance.

3.1.1.1 Nano MHP Reducing three-dimensional of 3D MHP to QDs represents an effective strategy for confining X-ray-generated excitons through spatial quantum confinement [56]. This approach enhances exciton wavefunction overlap by compressing carriers within dimensions below the Bohr radius, thereby significantly increasing exciton binding energy. This enhancement not only mitigates the impact of thermal energy on exciton stability but also augments the material's ability to efficiently convert and retain the energy from X-ray generated excitons. In 2017, Tang et al. [57] pioneered systematic investigations of $CsPbBr_3$ QDs under diverse solvents, concentrations, and X-ray irradiation environments. Their study revealed a significant linear correlation between RL intensity and X-ray tube current, establishing MHP QDs as promising scintillator materials. Subsequent advancements by Liu et al. [58] demonstrated solution-processable $CsPbX_3$ QDs (X = Cl, Br, I) with tunable X-ray-induced emissions (Fig. 2a and b). Unlike conventional bulk scintillators, these nanostructures enable low-temperature processing and spectral tunability through anion composition engineering. These features allow the fabrication of flexible and highly sensitive X-ray detectors with a detection limit of 13 $nGy_{air}\ s^{-1}$ (Fig. 2c), a fast decay time (Fig. 2d), and a high spatial resolution of 2.0 lp mm^{-1}. Notably, the color-tunable perovskite $CsPbX_3$ QDs scintillators can provide a convenient visualization tool for X-ray radiography (Fig. 2e). Sang et al. [21] further optimized $CsPbBr_3$ QDs (9 ± 1.5 nm) using a solution chemistry method and fabricated a scintillator film through photopolymerization. The engineered nanostructure minimized light scattering while achieving a higher spatial resolution of 9.8 lp mm^{-1}, a faster response time of 200 ns, and > 95% of photoluminescence quantum yield (PLQY). In addition to QDs, Omar F. Mohammed et al. [59] developed $CsPbBr_3$ nanoplatelets scintillators (Fig. 2f) for high-resolution X-ray imaging screens, which can be readily cast into uniform, crack-free, large-area films with the necessary thickness. These two-dimensional (2D) architectures demonstrated an ultrahigh light yield (~21,000 Ph MeV^{-1}) (Fig. 2g) and sustained performance under prolonged irradiation. While these studies highlight the exceptional scintillation properties of MHP NCs, their practical implementation faces critical challenges. The inherent soft lattice structure of MHPs makes them susceptible to degradation under harsh conditions including high temperature, moisture, and intense irradiation. In X-ray imaging applications, such instability not only compromises spatial resolution, but also increases operational costs through frequent component replacement. These limitations underscore the imperative for developing robust encapsulation strategies.

© The authors

https://doi.org/10.1007/s40820-025-01772-7

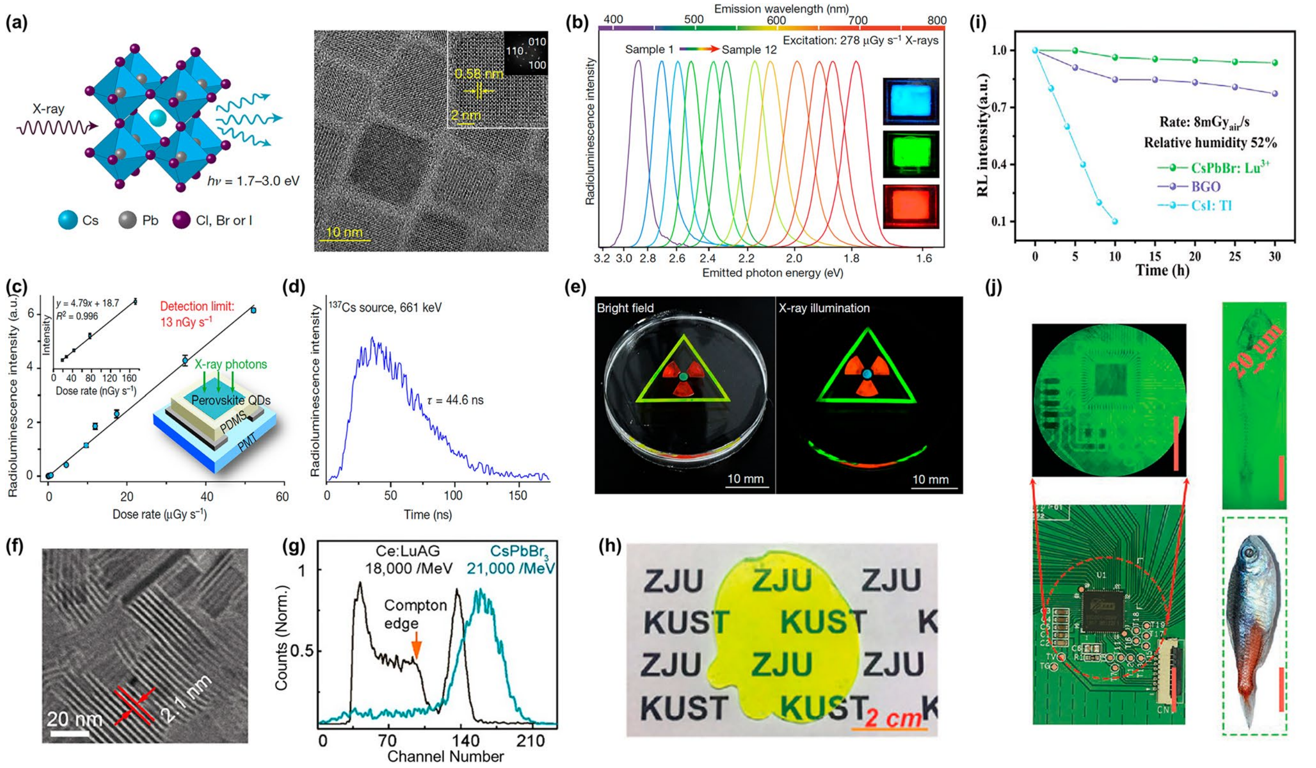

Fig. 2 Scintillator performances of MHP NCs. **a** Structural schematic and corresponding TEM image of synthesized $CsPbBr_3$ QDs. **b** Tunable X-ray-induced luminescence spectra of $CsPbX_3$ QDs. **c** RL intensity versus X-ray dose rate for $CsPbBr_3$ QDs. **d** RL decay kinetics of $CsPbBr_3$ QDs under ^{137}Cs irradiation. **e** Multicolor X-ray scintillation from $CsPbX_3$ QDs: orange ($CsPbBr_2I$), green ($CsPbBr_3$), blue ($CsPbClBr_2$) [58]. **f** TEM image of assembled $CsPbBr_3$ nanoplatelets. **g** Pulse height spectra comparing $CsPbBr_3$ nanoplatelets with LuAG:Ce scintillator [59]. **h** Photographs of $CsPbBr_3$ CG. **i** Normalized RL intensity under prolonged X-ray exposure for $CsPbBr_3$ CG, CsI: Tl, and BGO. **j** Photographs of a transistor panel in a cellphone and a fish recorded under daylight and X-ray irradiation, respectively [38, 60]

Xu et al. [38, 60, 61] addressed these challenges through a self-limited growth strategy that embeds $CsPbBr_3$ QDs within inorganic glass matrices (Fig. 2h). The encapsulation of $CsPbBr_3$ QDs within glass matrix ensures complete isolation from the external environment, simultaneously blocking atmospheric/water infiltration and preventing lead leakage. This architecture enables groundbreaking performance with a low detectable dose of 50 nGy$_{air}$ s^{-1} (Fig. 2i), and a spatial resolution of 16.8 lp mm^{-1} (Fig. 2j) is realized [38, 61]. The matrix-encapsulated design not only enhances operational stability but also addresses toxicity concerns, establishing a viable pathway for commercial deployment of perovskite-based radiation detectors.

3.1.1.2 Layered Structures Layered perovskites, particularly 2D MHPs, exhibit a quantum well architecture comprising alternating inorganic halide layers and organic ammonium spacers [62]. In this sandwich structure, the organic layers act as barriers due to their higher energy gap, while the inorganic layers act as wells due to their lower energy gap. Thus, the excitons can be confined in the inorganic layers. Subsequently, excitons from the inorganic layer have a high binding energy and oscillator strength, which endow the excitons in 2D MHPs with high light yield. This section will discuss how such structural engineering enables advanced radiation detection.

Soci et al. [19] pioneered comparative studies of 3D ($MAPbI_3$ and $MAPbBr_3$) and 2D $(EDBE)PbCl_4$ perovskites under X-ray excitation (Fig. 3a). It is observed that low-temperature X-ray excited luminescence measurements have shown that the X-ray luminescence yield can be as high as ~ 120,000 Ph MeV^{-1} in $(EDBE)PbCl_4$ at $T = 130$ K, and in excess of 150,000 Ph MeV^{-1} in $MAPbI_3$ and $MAPbBr_3$ at $T = 10$ K. While light yield of 3D perovskite $MAPbI_3$ and $MAPbBr_3$ is significantly reduced at room temperature (< 1,000 Ph MeV^{-1}), the 2D MHP $(EDBE)PbCl_4$ is less affected by thermal quenching (~ 9,000 Ph MeV^{-1} at room temperature) thanks to its large exciton binding energy

(Fig. 3b). This demonstrated that the large exciton binding energy in 2D perovskite makes them more robust against thermal quenching compared to their 3D counterparts, opening a new door for the application of 2D MHPs in scintillators. Subsequently, researchers have persistently pursued the development of novel 2D MHP and investigated strategies to augment their light yield, thereby pushing the boundaries of their performance. For instance, Liu et al. [63] designed an airflow-controlled solvent evaporation system to grow an inch-sized 2D $(PEA)_2PbBr_4$ SC (Fig. 3c), resulting in high light yield of 73,226 Ph MeV^{-1} (Fig. 3d) and a fast response time of 14 ns (Fig. 3e). Additionally, capitalizing on these superior properties, a high-resolution X-ray imager was fabricated by incorporating a $(PEA)_2PbBr_4$ SC with dimensions of 57 × 41 mm^2, and a high spatial resolution of 11.1 lp mm^{-1} is achieved. Liang et al. [40] demonstrated that the Mn^{2+}-doped BA_2PbBr_4 2D MHP demonstrates an ultrahigh sensitivity for X-ray, with a high X-ray scintillation light yield of up to 85,000 Ph MeV^{-1} and low detection limits of 16 nGy_{air} s^{-1}.

Recently, Birowosuto et al. [65] engineered dual-cation 2D perovskites by incorporating benzylammonium (BZA) into phenethylammonium (PEA) frameworks. The lattice contraction and bandgap widening from BZA doping enhanced electron–hole transfer efficiency by 60%, yielding > 70% fast decay components. Liang et al. [66] synthesized $(C_4H_9NH_3)_2PbBr_4$ (BPB) scintillators exploiting heavy-element inorganic layers for superior X-ray absorption. As a result, the BPB scintillator exhibited excellent performance, including a high light yield (22,000 Ph MeV^{-1}) and fast response times ($\tau_{decay} = 10.3$ ns) and high resolutions of 17.3 lp mm^{-1}; these are among the highest resolution levels for 2D MHP scintillators. Beyond their application in X-ray detection, this perovskite exhibits promising potential for high-energy radiation detection, encompassing the detection of alpha particles (α-particles), neutrons, and gamma rays, thereby extending their utility across a broader spectrum of radiation detection scenarios.

Additionally, process optimization can further enhance their scintillator performance. Niu et al. [64] presented a novel strategy for developing sub-nanosecond 2D MHP scintillators through dielectric engineering. The introduction of benzimidazole (BM) effectively reduced the polarity and dipole moment of the organic molecules, leading to a decrease in the dielectric permittivity and an increase in exciton confinement (Fig. 3f, g). This approach resulted in a significantly large exciton binding energy of 360.3 ± 4.8 meV, a light yield of 3,190 photons MeV^{-1} (Fig. 3h), and an ultrafast emission decay time of 0.97 ns. Additionally, this scintillator also demonstrated excellent performance in detecting γ-rays, neutrons, and α-particles, with a theoretical coincidence time resolution (CTR) of 65.1 ps for PET applications.

3.1.2 *Decreasing Self-absorption*

Due to the need for substantial thickness to ensure complete X-ray attenuation, MHP experience reduced light output efficiency, as the emitted light is partially absorbed within the structure itself. This issue highlights the critical need for strategies that can reduce self-absorption via expand the Stokes shift. To address this challenge, researchers have been exploring various approaches to minimize self-absorption, such as the development of STE emission in novel MHP materials, the introduction of emitting centers, and constructing the ET process. The following subsections will delve into these approaches in detail.

3.1.2.1 Self-trapped Exciton Emissions The quest to enhance scintillation light yield in MHP scintillators has placed significant emphasis on leveraging STE emissions. These materials exhibit a large Stokes shift and high PLQY, which are pivotal for efficient scintillation. During MHP emission process, excitons in MHPs strongly interact with phonons (lattice vibrations), leading to self-trapping and inhibition of their movement within the crystal. This results in the formation of local lattice deformations around the exciton. The key scintillation parameters of typical STE MHPs are summarized in Table 2.

STEs generally exist in materials with a soft lattice and strong exciton–phonon coupling. They are small polarons trapped by a local potential in the distorted lattice, which can be viewed as “excited-state defects.” When the exciton strongly couples to the phonon, the soft lattice will distort with the exciton self-trapped into a potential minimum it creates. Once the lattice is distorted, due to the lower energy, excitons will be quickly self-trapped and then relax back to the ground state accompanied by emitting photons with broad emissive bands and large Stokes shifts [53]. The discovery by Tang et al. of the lead-free halide Rb_2CuBr_3 scintillator highlighted the potential of 1D MHP with soft

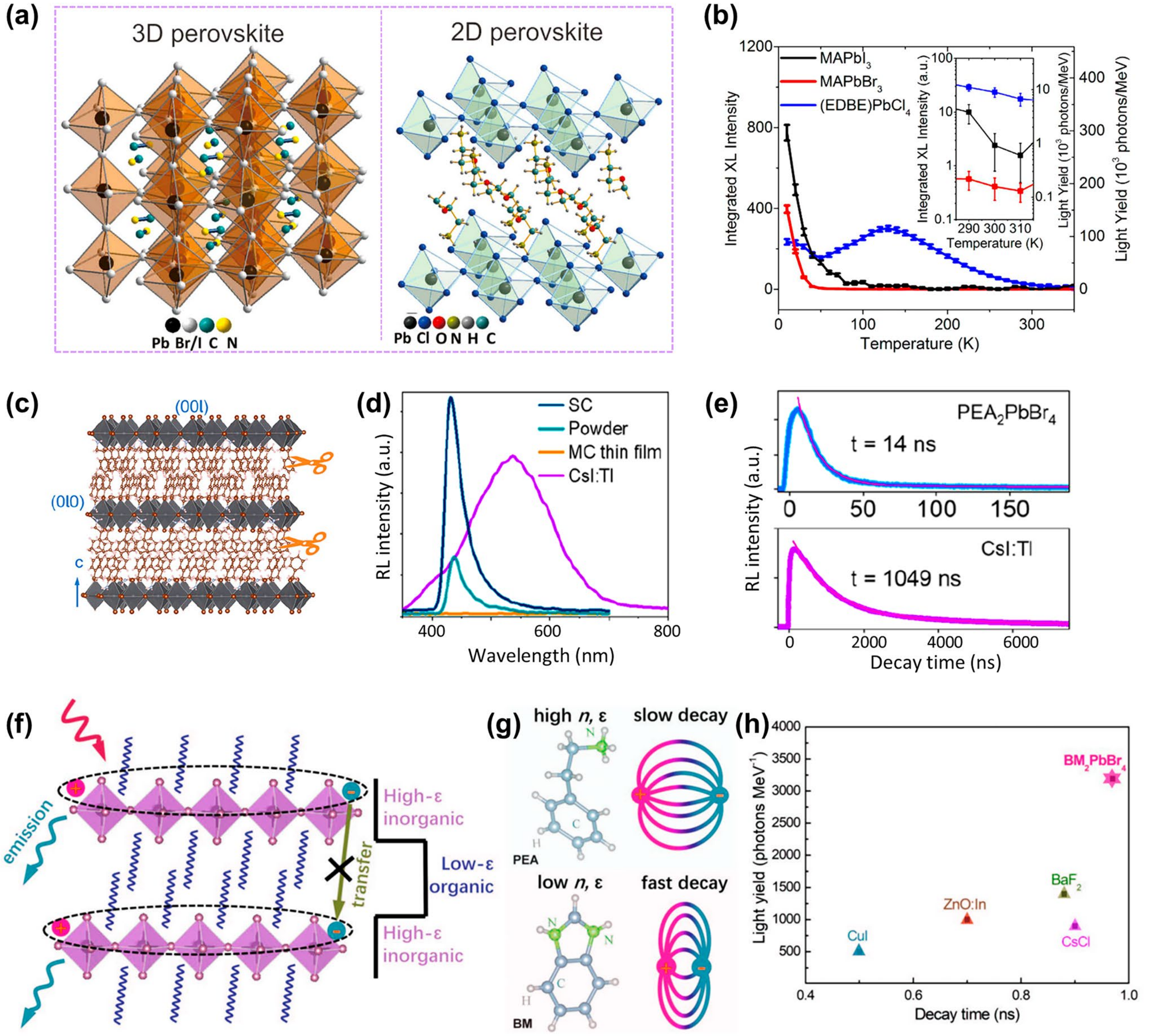

Fig. 3 Scintillator performances of 2D MHPs. **a** Crystal structure representation of MAPbX$_3$ (X = I, Br) 3D, and (EDBE)PbCl$_4$ 2D MHPs. **b** Temperature dependence of the light yields of MAPbI$_3$, MAPbBr$_3$, and (EDBE)PbCl$_4$ at various temperature [19]. **c** Crystal structure of the 2D layered (PEA)$_2$PbBr$_4$. **d** RL comparison of the (PEA)$_2$PbBr$_4$ SC, powder, and MC thin film and CsI: Tl SC under the same X-ray irradiation. **e** RL decay time comparison of (PEA)$_2$PbBr$_4$ SC and CsI:Tl [63]. **f** Crystal structures of 2D hybrid MHP with self-assembled 2D multiple quantum well structure. **g** Design strategy of enhancing exitonic dielectric confinement by choosing organic amines with low refraction index (n). **h** Comparison of the light yield of sub-nanosecond scintillators [64]

lattice structures to create STEs (Fig. 4a). These STEs not only exhibit a substantial Stokes shift of 85 nm (Fig. 4b) but also achieve an extraordinary PLQY of 98.6%, along with a record high light yield of ≈91,056 Ph MeV^{-1} (Fig. 4c).

Low-dimensional MHPs commonly exhibit STE emission due to their robust electron–phonon interactions. In these structure, photo-excited excitons possess significant binding energy, resulting in shared electron–hole bonds. Lei et al. developed the zero-dimensional hybrid cuprous halide [BAPMA]Cu$_2$Br$_5$, which promotes STEs formation via electron–phonon interaction, exhibiting a substantial Stokes shift of 244 nm and exceptional scintillator performances with a light yield of 43,744 Ph MeV^{-1} and a low detection threshold of 74 nGy$_{air}$ s^{-1}. Tang et al. [92] proposed an efficient ET mechanism within the quasi-2D perovskite structure to further reduce the self-absorption coefficient. They utilized the general formula $L_2A_{n-1}B_nX_{3n+1}$ for quasi-2D MHP, where large organic cations (L) segment the octahedral frame $[BX_6]^{2-}$, creating a "quantum well" that increases the electronic bandgap and exciton binding energy due to quantum and dielectric confinements. Consequently, the Stokes shift is successfully increased (Fig. 4d), and its self-absorption coefficient is reduced by threefold by controlling the phase distribution of varying n values (Fig. 4e). Furthermore, another representative STE emission family of low dimension MHP is alkali copper(I) perovskites, which has been demonstrated to be excellent scintillators with decent light yield and low detection limits, as evidenced by materials such as $Cs_3Cu_2I_5$ [41], $Cs_5Cu_3Cl_6I_2$ [85], $CsCu_2I_3$ [93], etc. For instance, Wu et al. [94] doped Tl^+ into $Cs_3Cu_2I_5$ single crystal (SC), achieving a light yield of 150,000 Ph MeV^{-1}, an extremely low afterglow of 0.17% at 10 ms, and low detection limit of 66.3 nGy_{air} s^{-1}. This scintillator also possesses a remarkable energy resolution of 3.4% at 662 keV and an ultrahigh light yield of 87,000 Ph MeV^{-1} under ^{137}Cs γ-ray irradiation.

Beyond low-dimensional MHPs, double perovskites also exhibit notable STE emissions. For instance, the large Stokes shift in the $Cs_2Ag_{0.6}Na_{0.4}In_{1-y}Bi_yCl_6$ scintillators contributes to high PLQY and light yield up to 39,000 ± 7,000 Ph MeV^{-1} [67]. In this case, the incorporation of Bi^{3+} into the lattice not only enhances the X-ray absorption efficiency but also modulates the luminescence properties. As the Bi^{3+} concentration increases, the PL peak shifts to longer wavelengths due to bandgap narrowing, resulting in a substantial Stokes shift. This shift is attributed to the formation of STEs, which minimize self-absorption and promote efficient light emission (Fig. 4f, g). Shi et al. [69] constructed a novel double-perovskite scintillator, Cs_2HfCl_6, exhibiting a high light yield of 21,700 Ph MeV^{-1}(Fig. 4h, i), a low detection limit of 55 nGy_{air} s^{-1}, and a high resolution of 11.2 lp mm^{-1}.

While STE emission effectively suppresses self-absorption by leveraging large Stokes shifts, its performance is inherently constrained by material-specific properties such as lattice softness and exciton-phonon coupling strength. For example, although the STE emission in low-dimensional MHPs can achieve high light yield, yet their emission wavelength and efficiency are still closely related to the material's dimensionality and composition, limiting design flexibility. To address this, researchers have further explored the strategy of doping luminescent ions, which introduces extrinsic activators to modulate ET pathways, thereby achieving self-absorption suppression in a broader range of material systems.

3.1.2.2 Doping Emitting Ions The introduction of emitting ions represents a strategic approach to mitigate self-absorption in scintillators, thereby enhancing their radiation detection efficiency and sensitivity. This methodology capitalizes on the modified energy levels and tailored absorption–emission profiles of dopants to optimize the scintillation process. Particularly, the incorporation of transition metal ions, notably Mn^{2+}, offers an alternative effective route to suppress self-absorption in MHPs scintillators, resulting in the enhancement of RL performances [95–100]. The key scintillation parameters of the Mn^{2+}-doped MHPs are summarized in Table 3.

Liang et al. [40] demonstrated the efficacy of Mn^{2+} activation in 2D perovskites by developing BA_2PbBr_4:Mn^{2+} scintillators. The Mn^{2+} ions act as activators, inducing a pronounced Stokes shift that reduces self-absorption losses, which otherwise decrease light output efficiency (Fig. 5b). Optimized BA_2PbBr_4: 10%Mn^{2+} achieved an exceptional X-ray light yield of up to 85,000 Ph MeV^{-1} (Fig. 5c) and low detection limits of 16 nGy_{air} s^{-1}. Further advancements by Chen et al. [123] revealed that Mn^{2+} ion doping significantly boosts the performance of 2D perovskite, phenylammonium cadmium chloride (PACC), achieving a quantum yield (PLQY) as high as 193%. In this case, Mn^{2+} ions integrated into the PACC structure act as ET mediators, facilitating Dexter ET from organic triplets to inorganic triplets, amplifying red phosphorescence. Moreover, Mn^{2+} ions effectively passivate deep trap states, curbing non-radiative decay of excitons and thereby enhancing overall luminescence efficiency. In addition to the X-ray detection, McCall et al. [124] extended Mn^{2+} doping applications to neutron imaging by developing $CsPb(Br/Cl)_3$:Mn^{2+} NCs. The as-obtained NCs exhibit an apparent large Stokes shift, which simultaneously improves PLQY and minimizes internal light loss (Fig. 5d–f). This breakthrough highlights Mn^{2+}'s versatility in addressing self-absorption challenges across diverse radiation detection modalities.

Additionally, lanthanide ions have garnered significant research attention due to their distinctive spectroscopic properties. These ions, owing to their numerous energy levels derived from the 4f electrons, exhibit a broad spectrum of emission bands. This characteristic enables the tailoring of

Table 2 Key scintillation parameters of the typical STE MHPs

Materials	Structural dimension	Emission wavelength (nm)	Stokes shift (nm)	Light yield (Ph MeV^{-1})	Decay time	Detection limitation	Resolution (lp mm^{-1})	Published year and Refs
Rb_2CuBr_3	1D	385	20	91,056	41,400 µs	121.56 $nGy_{air}\ s^{-1}$	–	2019 [4]
$Cs_2Ag_{0.6}Na_{0.4}In_{1-y}Bi_yCl_6$	2D	600	230	39,000 ± 7000	16 µs	19 $nGy_{air}\ s^{-1}$	4.4	2020 [67]
$[BAPMA]Cu_2Br_5$	0D	526	244	43,744	50.2 µs	74 $nGy_{air}\ s^{-1}$	15	2023 [68]
Cs_2HfCl_6	2D	447	227	21,700	–	55 $nGy_{air}\ s^{-1}$	11.2	2023 [69]
$Cs_5Cu_3Cl_6I_2$	1D	466	212	66,000	39 µs	11 $nGy_{air}\ s^{-1}$	27	2024 [49]
$CsPbCl_xBr_{3-x}:Yb^{3+}$	3D	1000	550	11,200	1242 µs	176.5 $nGy_{air}\ s^{-1}$		2023 [70]
$[DADPA]InCl_6{\cdot}H_2O:Sb^{3+}$	0D	554	196	51,875	2750 µs	98.3 $nGy_{air}\ s^{-1}$	25.15	2023 [71]
$CsMnCl_3$	3D	630	200	13,400	376 µs	470 $\mu Gy_{air}\ s^{-1}$	4.0	2022 [72]
$Cu_3Cu_2I_5$	0D	450	230	123,736	0.734 µs	183, 800 $nGy_{air}\ s^{-1}$	6.8	2022 [41]
$C_4H_{12}nCl_3$	0D	646	370	50,500	–	–	12.2	2022 [73]
$CsPbBr_3$	3D	515	150	15,800	–	120 $nGy_{air}\ s^{-1}$	12.5	2021 [38]
Cs_2AgI_3	1D	475	185	82,900	0.1928 µs	77.8 $nGy_{air}\ s^{-1}$	16.2	2022 [33]
Cs_2ZrCl_6	2D	440	190	49,400	83.55 µs	65 $nGy_{air}\ s^{-1}$	18	2022 [74]
Cs_2AgI_3	1D	500	190	27,000	0.288 µs	–	–	2021 [75]
$Cu_3Cu_2I_5:K^+$	0D	530	280	-	107.57 µs	63.5 $nGy_{air}\ s^{-1}$	5	2022 [76]
$Cs_3Cu_2I_5$:2% In^+	0D	450	227	70,169	–	3.58 $\mu Gy_{air}\ s^{-1}$	15	2023 [77]
$Cs_2NaGdCl_6:Tb^{3+}$	3D	470	205	39,100	–	41.32 $nGy_{air}\ s^{-1}$	10.75	2024 [78]
$Cs_2ScCl_5{\cdot}H_2O:Tb^{3+}$	0D	548	308	–	1516 µs	–	9.5	2024 [79]
$Cs2AgIn_{0.9}Bi_{0.1}Cl_6$	2D	550	230	32,000	–	87 $nGy_{air}\ s^{-1}$	12	2024 [80]
$[FMPPA]ZnBr_4$	0D	500	180	29,300 ± 600	2.64 µs	352 $nGy_{air}\ s^{-1}$	12.5	2024 [81]
$(C_{20}H_{20}P)_2SbCl_5$	0D	600	245	12,535	–	3160 $nGy_{air}\ s^{-1}$	30	2024 [82]
CsCdMnBiCl	2D	580	220	34,450	490.41 µs	183.6 $nGy_{air}\ s^{-1}$	16.7	2024 [83]
$Eu:CsCaCl_3$	3D	430	65	9,300	0.991 µs	213.8 $\mu Gy_{air}\ s^{-1}$	30.0	2024 [84]
$Cs_5Cu_3Cl_6I_2$	1D	470	170	19,865	41.09 µs	152 $mGy_{air}\ s^{-1}$	20	2024 [85]
$CsPbCl_3:Br_{0.02}$	3D	430	65	–	0.343 ns	–	4.0	2024 [86]
Cs_2TeCl_6	3D	575	180	38,523	4.88 µs	258 $nGy_{air}\ s^{-1}$	15.9	2024 [87]
$Cs_2NaTbCl_6$	3D	548	306	–	2360 µs	79.09 $nGy_{air}\ s^{-1}$	10	2024 [88]
$CsPb_2Br_5$	3D	700	320	24,160	–	162.3 $nGy_{air}\ s^{-1}$	21	2024 [89]
$Cs_3Cu_2Cl_5$	0D	510	195	95,000	112 µs	2.70 $\mu Gy_{air}\ s^{-1}$	105	2024 [90]
$Cs_2SnCl_6:Te^{4+}$	3D	600	235	–	3.82 µs	132 $nGy_{air}\ s^{-1}$	20	2023 [91]

the RL emission wavelengths, serving as versatile additional luminescent centers. By strategically incorporating lanthanide ions, the RL spectra can be strategically broadened or fine-tuned, effectively mitigating self-absorption phenomena within the scintillating matrix. This approach not only optimizes light yield but also enhances the material's adaptability across diverse applications requiring specific wavelength emissions (Fig. 6a, b) [125–129].

In 2017, Song et al. [130] reported a significant boost in the overall PLQY of lanthanide-doped $CsPbCl_3$ NCs over their undoped counterparts. This enhancement is largely attributed to the intrinsic luminescence of the lanthanide ions. Remarkably, even with ET from the excitons to the lanthanide ions, the PLQY of the excitonic emission in the $CsPbCl_3$ NCs matrix itself experiences an increase. As for the X-ray properties, Xu et al. [37] pioneered a strategy that entails doping lanthanide Eu^{3+} ions into $CsPbBr_3$ ceramic glass (CG) to effectively curb self-absorption phenomena. This approach achieves dual benefits: improved crystallinity/narrowed size distribution (enhancing spatial resolution) and introduction of Eu^{3+} red emission centers to suppress self-absorption (Fig. 6c, d). This innovative integration not only improves structural integrity but also optimizes the scintillation efficiency, highlighting the strategic value of rare-earth

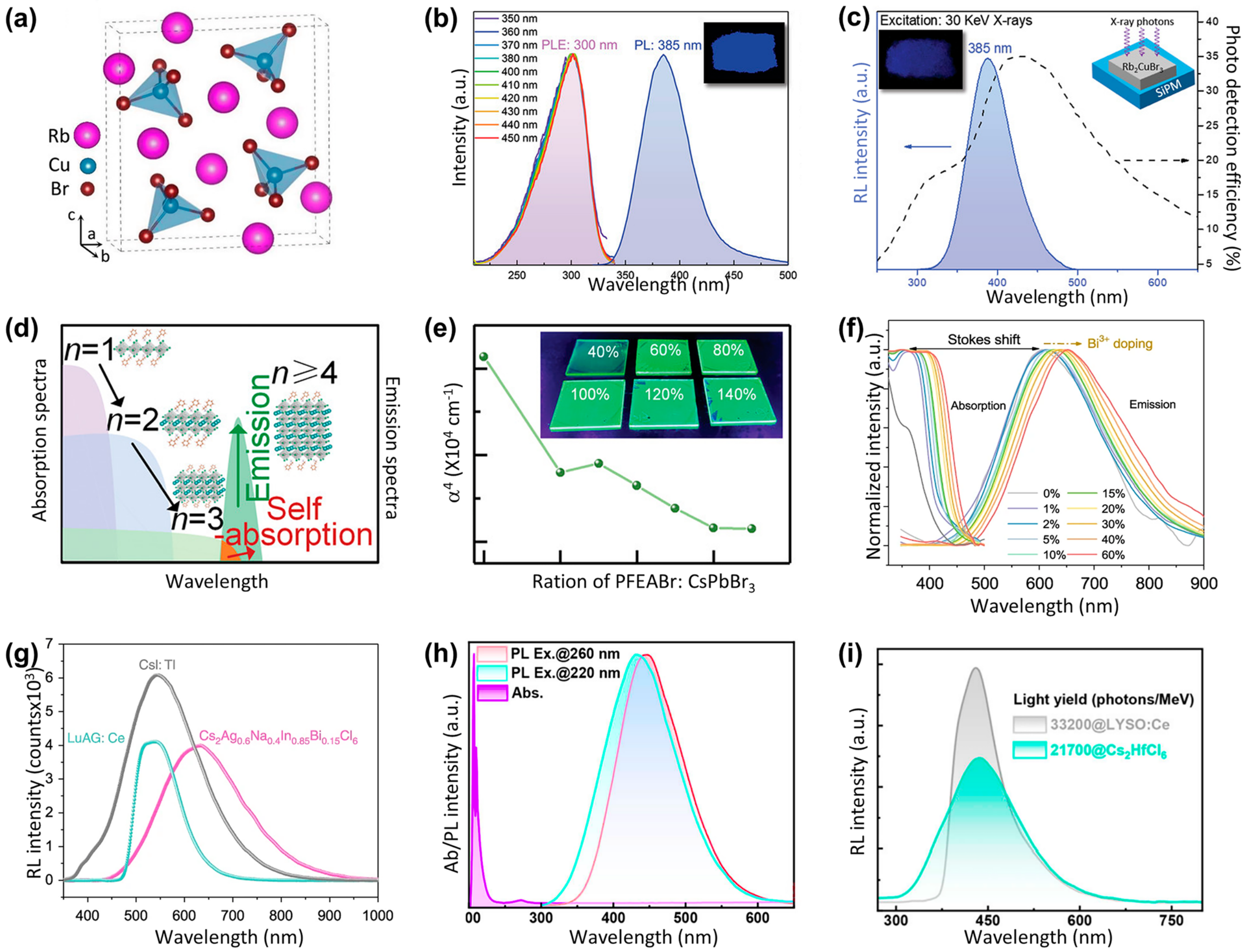

Fig. 4 Scintillator performances of STEs MHPs. **a** Crystal structure of Rb_2CuBr_3. **b** PL spectrum of Rb_2CuBr_3 under 300 nm excitation and PLE spectra monitored at emission wavelengths from 350 to 450 nm. **c** RL spectrum of Rb_2CuBr_3 under 30 keV X-ray excitation and wavelength-dependent photon detection efficiency of the silicon photomultiplier (SiPM). **d** ET in quasi-2D MHPs contributes to a larger Stokes shift. **e** The calculated self-absorption coefficient of the quasi-2D perovskite film [92]. **f** RL spectra of $Cs_2Ag_{0.6}Na_{0.4}In_{0.85}Bi_{0.15}Cl_6$, LuAG: Ce and CsI: Tl scintillators. **g** Stokes shift of $Cs_2Ag_{0.6}Na_{0.4}In_{1-y}Bi_yCl_6$ with different Bi^{3+} contents [67]. **h** Absorption and PL spectra of Cs_2HfCl_6. **i** RL spectra of Cs_2HfCl_6 film and LYSO: Ce [69]

doping in advancing scintillator technology. Song et al. [70] further revolutionized X-ray detection through Yb^{3+}-doped $CsPbCl_xBr_{3-x}$, leveraging quantum cutting to convert high-energy photons into multiple low-energy photons. This strategy led to a remarkable boost in the PLQY to an impressive 149%, accompanied by a substantial Stokes shift exceeding 550 nm (Fig. 6e). Finally, the scintillator achieved an exceptional light yield of approximately 11,2000 Ph MeV^{-1} (Fig. 6f), coupled with an impressively low detection limit of 176.5 nGy_{air} s^{-1}. This dramatic improvement is attributed to the quantum cutting phenomenon, wherein Yb^{3+} ions efficiently transmute a single high-energy photon into multiple lower-energy photons.

Despite the success of ion doping, their practical application still faces many challenges, including precise control of doping concentration, uniform distribution of ions, and energy matching between host matrix and activator ions. Over-reliance on specific dopants may also restrict material universality. To break through these bottlenecks, ET channel construction in heterostructured composites (e.g., perovskite-dye hybrids) has emerged as a versatile strategy, which will be discussed in the next section.

Table 3 Scintillation properties of the Mn^{2+}-doped MHPs

Materials	Emission wavelength (nm)	Stokes shift (nm)	Light yield (Ph MeV^{-1})	Decay time	Detection limitation	Imaging resolution (lp mm$^{-1)}$	Published year and references
$Cs_2CdBr_2Cl_2$:Mn^{2+}	495	210	64,950	70.74 µs	17.82 $\text{nGy}_{\text{air}}\ \text{s}^{-1}$	12.3	2023 [101]
BA_2PbBr_4:Mn^{2+}	610	222	85,000	727.83 µs	16 $\text{nGy}_{\text{air}}\ \text{s}^{-1}$	10.7	2022
$CsMnCl_3$	650	132	13,400	460.5 µs	470 $\mu\text{Gy}_{\text{air}}\ \text{s}^{-1}$	4.3	2023 [102]
$Cs_3Cu_2I_5$:Mn^{2+}	445	135	95,772	1.086 µs	–	–	2023 [103]
$Cs_3Cu_2I_5$:Mn^{2+}	565	185	65,000	–	49 $\text{nGy}_{\text{air}}\ \text{s}^{-1}$	11.8	2023 [104]
$Cs_2NaBiCl_6$:Mn^{2+}	586	67	28,350	1.22 ms	45.2 $\text{nGy}_{\text{air}}\ \text{s}^{-1}$	14.76	2023 [105]
Cs_2CdCl_4:Mn^{2+}	585	340	88,138	24.3 ms	31.04 $\text{nGy}_{\text{air}}\ \text{s}^{-1}$	16.1	2023 [106]
$Cs_3Cu_2I_5$:Mn^{2+}	442	132	67,000	–	–	–	2019 [107]
SS-/RR-1:Mn^{2+}	530	165	14,912	729 µs	58.1 $\text{nGy}_{\text{air}}\ \text{s}^{-1}$	–	2023 [108]
$Cs_7Cd_3Br_{13}$: Mn^{2+}/Pb^{2+}	576	248	41,000	125 ns	15.92 $\text{nGy}_{\text{air}}\ \text{s}^{-1}$	10.9	2023 [109]
$CsCdCl_3$:Mn^{2+}	605	315	–	7.92 ms	–	12.2	2023
$Cs_3Cu_2I_5$:Mn^{2+}	562	272	71,000	1.2 µs	127.5 $\text{nGy}_{\text{air}}\ \text{s}^{-1}$	16.2	2023 [110]
$CsCu_2I_3$:Mn^{2+}	580	250	32,000	58.92 ns	80.2 $\text{nGy}_{\text{air}}\ \text{s}^{-1}$	16.6	2023 [111]
$CsCdCl_3$:Mn^{2+}, Zr^{4+}	520	95	–	–	–	12.5	2023 [112]
DA_2PbBr_4:Mn^{2+}	620	365	35,292	–	108.17 $\mu\text{Gy}_{\text{air}}\ \text{s}^{-1}$	10	2023 [113]
$MAPbCl_3$:Mn^{2+}	600	260	451	1.5 ns	–	–	2020 [114]
$CsCdCl_3$:Mn^{2+}, Sb^{3+}	600	346	74,828	–	29.9 $\text{nGy}_{\text{air}}\ \text{s}^{-1}$	20	2024 [115]
Cs_2ZnBr_4:Mn^{2+}	526	161	15,600	255.90 µs	1.16 $\mu\text{Gy}_{\text{air}}\ \text{s}^{-1}$	5.06	2023 [116]
$Cs_4CdBi_2Cl_{12}$:Mn^{2+}	580	220	34,450	800 µs	183.6 $\text{nGy}_{\text{air}}\ \text{s}^{-1}$	16.7	2024 [83]
Cs_2SnF_6:Mn^{2+}	630	165	3,000	6.97 ms	0.72 $\mu\text{Gy}_{\text{air}}\ \text{s}^{-1}$	22	2022 [117]
$(C_{38}H_{34}P_2)MnBr_4$	517	157	80,000	318 µs	72.8 $\text{nGy}_{\text{air}}\ \text{s}^{-1}$	–	2019 [118]
$[TPPen]_2Mn_{0.9}Zn_{0.1}Br_4$	515	65	68,000	296.34 µs	204.1 $\text{nGy}_{\text{air}}\ \text{s}^{-1}$	11.2	2023 [119]
$(Br\text{-}BzTPP)_2MnBr_4$	534	171	80,100	300 µs	30 $\text{nGy}_{\text{air}}\ \text{s}^{-1}$	14.06	2024 [45]
$(Br\text{-}PrTPP)_2MnBr_4$	517	237	68,000	280 µs	45 $\text{nGy}_{\text{air}}\ \text{s}^{-1}$	12.78	2024 [120]
$(C_{25}H_{22}P)_2MnBr_4$	512	258	78,937	330 µs	108.2 $\text{nGy}_{\text{air}}\ \text{s}^{-1}$	25.61	2024
$(ETP)_2MnBr_4$	525	60	66,000	264 µs	1.7 $\mu\text{Gy}_{\text{air}}\ \text{s}^{-1}$	26.8	2024 [121]
HTP_2MnBr_4	520	155	38,000	318.11 µs	0.13 $\mu\text{Gy}_{\text{air}}\ \text{s}^{-1}$	17.28	2023 [122]

3.1.2.3 Developing Composite Materials The construction of ET channels by synthesizing the MHP-based composite materials leverages the synergistic interaction between different components to facilitate efficient ET. 2020, Sergio Brovelli et al. [131] devised a strategy where $CsPbBr_3$ NCs act as sensitizers for an organic emitter (perylene dyad 1) (Fig. 7a). The organic emitter is specifically designed to have a large Stokes shift between its absorption and emission spectra (Fig. 7b). This strategic design ensures minimal overlap between the emission spectrum of the sensitizer and its absorption spectrum, thereby reducing self-absorption (Fig. 7c). By efficiently transferring energy from the $CsPbBr_3$ NCs to the organic emitter, the composted scintillator achieves a light yield of 9,000 Ph MeV^{-1} and a fast emission lifetime of less than 4 ns. Building upon this foundation, Li et al. [132] further demonstrated the versatility of this approach (Fig. 7d). By incorporating organic dyes, pyrromethene 597 (PM597 organic dye) for example, into purified $CsPbBr_3$ nanowires (NWs), they achieved effective ET, leading to a 60 nm red-shift in RL and accelerated RL recombination rates (Fig. 7e). Consequently, the light yield was enhanced by approximately 4.1 times compared to pure perovskite NWs scintillators. This approach yielded a low detection limit of 152 $\text{nGy}_{\text{air}}\ \text{s}^{-1}$ and an impressive resolution of 11.5 lp mm^{-1}.

Beyond mere composite formation, optimizing the ET process through refinement of fabrication techniques is essential. Yang et al. [133] designed multi-site ZnS(Ag)-$CsPbBr_3$ heterostructures to modulate the ET process (Fig. 7f, g). They found that external energy from ZnS(Ag) can effectively transfer to $CsPbBr_3$ based on the non-radiative Förster resonance energy transfer (FRET), which is crucial for inhibiting photon self-absorption. This efficient

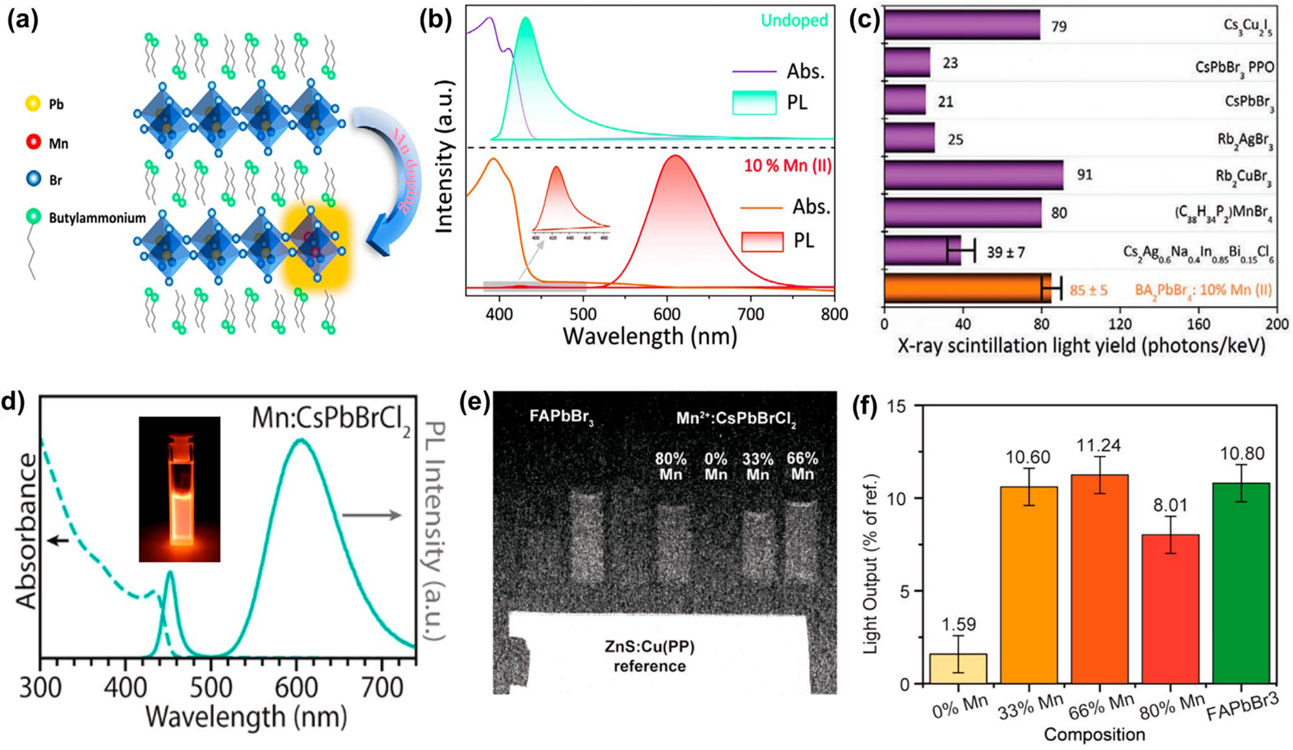

Fig. 5 Scintillator performance of Mn^{2+}-doped MHPs. **a** Schematic diagram of Mn^{2+}-doped BA_2PbBr_4. **b** Absorption and PL spectra of undoped and 10% Mn^{2+}-doped BA_2PbBr_4. **c** Comparison of the X-ray scintillation light yield of BA_2PbBr_4:10% Mn^{2+} with several previously reported MHP scintillators [40]. **d** Absorption and PL spectra of $CsPb(BrCl)_3$: Mn^{2+} NCs. **e** Radiograph of $CsPbBrCl_2$: Mn^{2+} NC under fast neutron irradiation as compared with $FAPbBr_3$ NCs and a commercial ZnS: Cu screen. **f** Light output performance of $FAPbBr_3$ NCs [124]

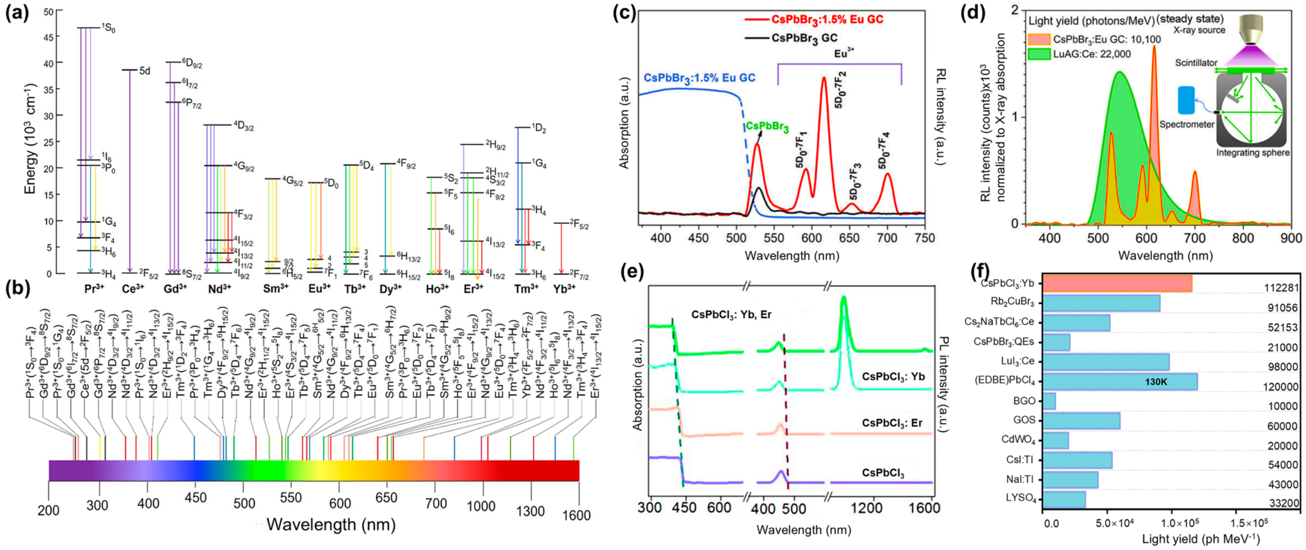

Fig. 6 Lanthanide-doped MHP scintillators. **a** Partial 4f-energy level diagram for trivalent lanthanide activators. **b** Main luminescent transitions of the lanthanide activators in the electromagnetic spectrum [129]. **c** RL spectra of $CsPbBr_3$ CG, $CsPbBr_3$: Eu^{3+} CG under X-ray excitation. **d** Steady-state light yield calculation of $CsPbBr_3$: Eu^{3+} CG, commercial LuAG: Ce. **e** Absorption spectra, visible emission spectra and near-infrared emission spectra ($\lambda_{ex} = 365$ nm) of lanthanide-free and -doped $CsPbCl_3$. **f** Comparison of the light output between $CsPbCl_3$: $Yb.^{3+}$ scintillators and several typical scintillators [70]

© The authors

https://doi.org/10.1007/s40820-025-01772-7

FRET process resulted in a light yield of 40,000 Ph MeV^{-1} for the heterostructure (IH)-type $CsPbBr_3$ scintillator, which is significantly higher than the 30,000 Ph MeV^{-1} for the physically mixed (PM)-type $CsPbBr_3$ scintillators. Finally, the IH-type scintillator exhibits a short radioluminescence (RL) decay time of 36 ns and a high spatial resolution of 30 lp mm^{-1}, enabling high-speed X-ray imaging at 200 frames s^{-1}.

3.1.3 Enhancing Crystallinity

Effectively enhancing the crystallinity of MHP is also considered at a significantly for improving their light yield. By refining the crystal growth process and reducing defects, such as grain boundaries and impurities, the scintillator material becomes more efficient at converting incoming radiation into detectable light. This is because better crystallinity minimizes non-radiative recombination events, which can otherwise lead to energy loss without photon emission. Consequently, a more uniform and defect-free crystal structure allows for a higher probability of radiative recombination, resulting in an increased number of photons being produced per unit of energy deposited, thereby enhancing the overall light yield and sensitivity of the MHP scintillator. By employing a secondary annealing process, amorphous clusters are given sufficient time to rearrange, thereby eliminating amorphous clusters. For instance, Huang et al. [136] demonstrated the effectiveness of solvent annealing in enhancing the crystallinity and grain size of organometal trihalide perovskite, specifically methylammonium lead trihalide perovskite $(CH_3NH_3)PbX_3$. Liu et al. [137] also demonstrated that by using the two-stage annealing strategy to improve the crystallinity of $CH_3NH_3PbI_3$ films. However, conventional annealing risks material decomposition or grain aggregation, which may degrade device performance.

Furthermore, site engineering has also been demonstrated to enhance the crystallinity of MHP, as it involves strategically manipulating the chemical composition and structure of the MHP material. By carefully selecting and incorporating specific ions or molecules into the MHP lattice, the crystal quality can be improved; defects can be reduced. Zhang et al. [134] proposed an innovative approach to enhance crystallinity of hybrid organic–inorganic perovskite, CH_3NH_3I, through a strategic A-site management technique (Fig. 8a). In this case, the strategy involves the introduction of an A-site placeholder cation, $NH_4{}^+$, to offset the deficient methylammonium (MA^+) precipitation by occupying the cavity of Pb-I framework, thereby promoting to offset the precipitation rate discrepancy between the inorganic PbI_2 and the organic MA^+ components. The enhanced intensity and reduced full-width at half-maximum of the (110) diffraction peak from 0.18° to 0.13° indicate that $NH_4{}^+$ addition significantly improves the MHP's crystal quality and preferred orientation (Fig. 8b), and then result in the reduction in defect density and prolonged carrier lifetime. This strategy is also demonstrated to be universal for other mixed-cation MHP systems, providing a significant advancement in the synthesis of high-quality MHP materials. Yuan et al. [138] reported that the introduction of rubidium ions (Rb^+) into the precursor solution significantly boosts the crystalline quality of phenylethylammonium (PEA^+)-based Ruddlesden–Popper (RP) MHPs. It is demonstrated that the added Rb^+ ions are found to accumulate at the crystal growth front, forming a Rb^+-rich region that acts as a mild inhibitor, slowing down the absorption and diffusion of organic cations and thus improving the crystalline quality. Wang et al. illustrated that adopting an impurity doping strategy also significantly improves the crystallinity of lead-free MHP $Cs_2AgIn_xBi_{1\text{-}x}Cl_6$. Through meticulous adjustment of the In^{3+} to Bi^{3+} ratio, they fabricated $Cs_2AgIn_{0.9}Bi_{0.1}Cl_6$ MHP films with exceptional scintillation properties, with a remarkable light yield of up to 32,000 Ph MeV^{-1} and an impressive X-ray detection sensitivity down to 87 nGy$_{air}$ s^{-1}. In 2021, Yang et al. [37] successfully showed that integrating lanthanide ions, specifically Eu^{3+} ions, into a $CsPbBr_3$ glass–ceramic (GC) matrix significantly enhances the crystallization process (Fig. 8c), leading to a more homogeneous dispersion of the $CsPbBr_3$ CG (Fig. 8d, e). This uniform distribution not only mitigates light scattering but also boosts the photoluminescence intensity of the $CsPbBr_3$ CG. Ultimately, this finding revealed that the $CsPbBr_3$: 1.5%Eu^{3+} CG scintillator achieved an impressive estimated light yield of 10,000 Ph MeV^{-1}, highlighting a substantial advancement in scintillator performance by site engineering.

Further optimization of the crystallinity can be also achieved through controlling the nucleation process. Kuang et al. [135] developed a high-quality microcrystalline thick film of mixed-cation perovskite $MA_{0.42}FA_{0.58}PbI_3$ by manipulation the nucleation process.

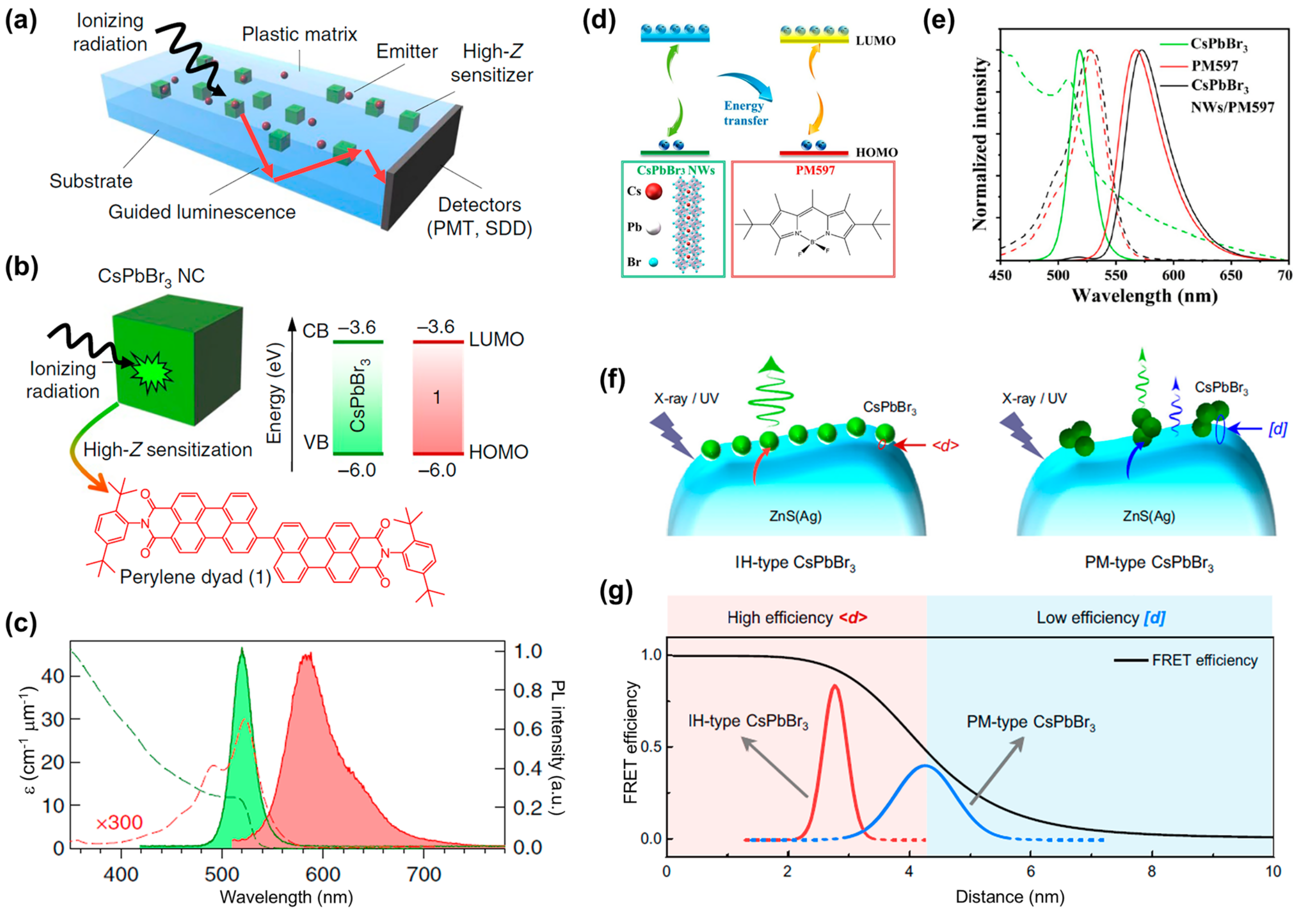

Fig. 7 ET strategies for MHP scintillators. **a** Schematic depiction of composited scintillator for constructing the ET process. **b** Sketch of a $CsPbBr_3$ NCs sensitizing the perylene dyad 1. **c** Molar extinction coefficient and PL spectra of $CsPbBr_3$ NCs and perylene dyad 1 [131]. **d** Diagram of ET between the $CsPbBr_3$ NWs and PM597 organic dye molecules. **e** The optical absorption and PL spectra of $CsPbBr_3$ NWs, PM597 organic dye, and $CsPbBr_3$ NWs/PM597 organic dye [132]. **f** Schematic of two kinds of structural configurations, IH-type $CsPbBr_3$ and PM-type $CsPbBr_3$. **g** Calculated FRET efficiency of IH-type $CsPbBr_3$ and PM-type $CsPbBr_3$ scintillator [133]

They utilized an ultrasound-assisted crystallization method combined with a hot pressing technique for the crystallization control (Fig. 8f). Ultrasound ensured homogeneous nucleation of microcrystals, while subsequent hot pressing eliminated grain boundaries and voids through plastic deformation. This dual approach enhanced carrier mobility and mobility lifetime products by 13-fold and 18-fold, respectively, ultimately achieving exceptional detector sensitivity (1.16×10^{6} μC Gyair^{-1} cm^{-2}) and ultralow detection limits (37.4 nGyair s^{-1}).

3.2 Response Time Modulation

Scintillators are materials that convert high-energy radiation into visible light, and their decay time is a critical parameter affecting the response dynamics and overall performance of detection systems. The decay rate of the luminescence center is primarily determined by the transition of the magnetic dipole moment from the excited state back to the ground state. This rate can be augmented by nonradiative quenching or ET processes that divert from the excited state. In the simplest case of exponential decay, the emission intensity $I(t)$ can be expressed as $I(t)=\exp(-t/\tau)$, where τ is the decay time. It is noteworthy that in practical scenarios, the decay time of the scintillator is sometimes approximated by a simple 1/e or 1/10 decay time, which is

© The authors

https://doi.org/10.1007/s40820-025-01772-7

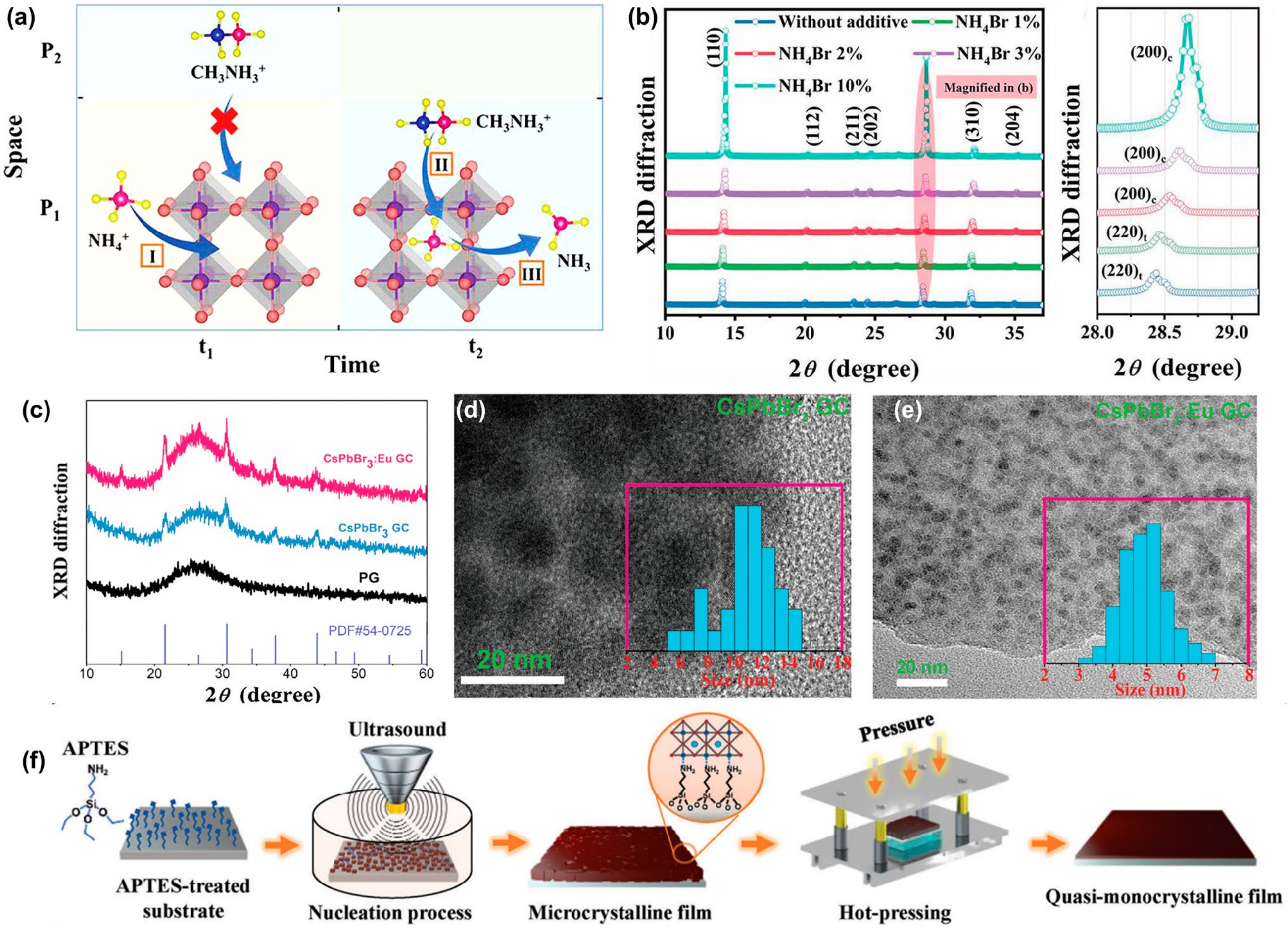

Fig. 8 Crystalline enhancement strategies for MHP scintillators. **a** Schematic diagram of the A-site management strategy. **b** XRD patterns of MA-based MHP films with varying NH_4Br concentrations [134]. **c** XRD patterns of precursor glass (PG), $CsPbBr_3$ and $CsPbBr_3$: Eu^{3+} CG. TEM images of **d** $CsPbBr_3$ and **e** $CsPbBr_3$: 1.5%Eu.$^{3+}$ CG [37]. **f** Schematic illustration of the fabrication process for MHP microcrystalline film via ultrasound-assisted crystallization and hot pressing [135]

the duration for the light intensity post-high-energy excitation to drop to 1/e or 1/10 of its initial value. In the realm of X-ray detection, the significance of both rapid and delayed response times cannot be overstated [20]. Rapid response times are crucial for applications demanding high temporal resolution, particularly in high-definition dynamic and real-time X-ray imaging scenarios. Conversely, delayed response times offer distinct advantages in specific detection scenarios, such as non-destructive testing in complex environments, including nuclear radiation dosimetry and the examination of intricate structures. In this section, the MHP scintillators in both fast and delayed response time detection are comprehensively discussed.

3.2.1 *Fast Response Time*

A rapid decay time is an extremely desirable trait for advanced radiographic technologies such as Time-of-Flight Positron Emission Tomography (TOF-PET) and real-time X-ray imaging. In TOF-PET, where the precise timing of photon detection from positron annihilation is crucial, a swift decay of the scintillation signal significantly enhances image resolution and SNR. By capturing and differentiating the arrival times of these photons with high precision, the spatial resolution of PET scans improves, allowing for more accurate localization of the radiotracer within the body, thereby increasing diagnostic accuracy and efficiency. In the field of real-time X-ray imaging, including applications in medical surgeries, industrial inspection, and airport security, a fast response from the scintillator enables continuous and rapid image updates, essential for capturing dynamic processes in real time. It minimizes motion artifacts and enhances image clarity and contrast, allowing for immediate and accurate assessments by medical professionals and inspectors. Furthermore, in applications requiring high frame rates, such as cardiovascular imaging, a swift decay ensures no residual signal between frames, preventing image blurring and ensuring crisp, continuous imaging. Thus, the development and implementation of scintillators with fast decay times are pivotal advancements driving the evolution of these sophisticated imaging technologies, enhancing diagnostic precision, and treatment effectiveness. Generally, decay time is an intrinsic property of scintillating materials, which is determined by the material's composition and structure. Previous work has established that high carrier mobility and short carrier lifetimes, which are desirable for fast scintillation response, are predominantly found in lead-based MHP materials. Therefore, we summarized the recent reported lead-based MHPs as scintillators and the corresponding strategies to further optimize light yield, decay time.

In 2018, Heo et al. [21] revolutionized a $CsPbBr_3$-based X-ray detector by incorporating the $CsPbBr_3$ NCs with methyl methacrylate (MMA) and a photo-initiator, boasting superior spatial resolution (9.8 lp mm^{-1} at an MTF of 0.2), rapid response times of approximately 200 ns, and comparable stability under intense X-ray exposures exceeding 40 Gy_{air} s^{-1}. Simultaneously, Liu et al. [58] reported the as-obtained $CsPbBr_3$ NCs via solution method, exhibiting a very fast response ($\tau = 44.6$ ns) upon ^{137}Cs source excitation, making them ideal for dynamic real-time X-ray imaging. To optimize the decay time or light yield, researchers have also delved into the exploration of fabrication processes for further refinement. For instance, Xu et al. [22] doped $CsPbBr_3$ NCs with lanthanide ions, Lu^{3+}, which resulted in a significant increase in the internal quantum efficiency from 25.67 to 65.7%. Consequently, the optimized $CsPbBr_3$:Lu^{3+} NCs exhibit a fast decay time ($\tau = 27$ ns). This enhancement is attributed to the effective improvement in the crystallinity of $CsPbBr_3$ NCs and the enhanced X-ray absorption efficiency. Lee et al. [139] proposed a biphasic MHP scintillator formed by introducing $CsPb_2Br_5$ into $CsPbBr_3$ to improve the scintillator behaviors. This approach mitigated surface defects on $CsPbBr_3$, thereby enhancing photostability, hydrophobicity, thermal resilience, and luminescence. This optimized dual-phase material exhibited a PLQY of 65.2%, a swift response time of 2.93 ns, a remarkable light yield of 19,200 Ph MeV^{-1}, and an outstanding spatial resolution of 8.19 lp mm^{-1}. Aside from $CsPbBr_3$, there are also other emerging fast decay time scintillators, such as organic–inorganic hybrid MHPs. In 2019, Mykhaylyk et al. [140] demonstrated that $MAPbBr_3$ exhibits rapid and intense scintillation at cryogenic temperatures (50–130 K). At 77 K, the material achieved a light yield of 90,000 ± 18,000 Ph MeV^{-1}, which further increased to 116,000 ± 23,000 Ph MeV^{-1} at 8 K. Notably, the decay components feature ultrafast (sf) and slow (ss) components of 0.1 ns and 1 ns, respectively, indicating the potential for achieving high temporal resolution. Muhammad et al. [141] advanced the field by optimizing the synthesis process for $MAPbBr_3$ SCs, yielding millimeter-sized crystals with high quality. The optimized crystals displayed a remarkable scintillation response with a dominant ultrafast decay component of 0.52 ns (82.2%) and a secondary component of 1.80 ns (17.8%), emphasizing the pivotal role of synthesis optimization in boosting the scintillation properties of MHPs.

Additionally, 2D lead-based MHPs and their derivatives have garnered significant attention due to their unique layered structures, which are beneficial in reducing non-radiative recombination and potentially enabling faster response times. For instance, $(PEA)_2PbBr_4$ scintillator stands out as an optimal scintillator, combining high light yield with rapid nanosecond decay times. Pioneering the use of $(PEA)_2PbBr_4$ as a scintillator, Kishimoto et al. [142] demonstrated a light yield of 10,000 Ph MeV^{-1} and a swift fluorescence decay time of merely 9.9 ns. Utilizing a 0.9-mm-thick $(PEA)_2PbBr_4$ crystal as an X-ray detector, they successfully detected nuclear resonance scattering in N61i through synchrotron radiation, achieving a temporal resolution of 0.7 ns and a high detection efficiency of 24%. This study underscores the potential of 2D lead-based MHPs scintillators in sub-nanosecond time-resolved X-ray measurements. Building on this foundation, the library of 2D lead-based MHPs as scintillator materials was improved research. For example, Liu et al. [72] successfully synthesized 2D lead-based MHPs $(C_4H_{12}N)_2PbBr_4$ (BA_2PbBr_4), which exhibited a fast decay time of 2.66 ns and demonstrated a high resolution of approximately 1 lp mm^{-1} in neutron imaging. Mohammed et al. [66] introduced the organic–inorganic hybrid MHP $(C_4H_9NH_3)_2PbBr_4$ (BPB) as a scintillator for both fast neutron and X-ray detection. The hydrogen-rich organic component in BPB acts as a fast neutron converter, generating detectable recoil protons, while the heavy atom-rich inorganic part efficiently deposits the energy of charged recoil protons and provides a large X-ray cross section. The as-obtained BPB scintillator had a decay time of 10.3 ns and showcased high-resolution imaging of about 1 lp mm^{-1} in neutron imaging and 17.3 lp mm^{-1} in X-ray imaging. Liu et al. [63] employed an airflow-controlled solvent evaporation system to grow inch-sized 2D $(PEA)_2PbBr_4$ SCs, which demonstrated a high light yield of 73,226 Ph MeV^{-1} and a rapid response time of 14 ns. Recently, Niu et al. [64] designed a 2D lead-based MHPs by intercalating benzimidazole (BM) with a low dielectric constant between $[PbBr_6]^{2-}$ layers. The resulting BM_2PbBr_4 single crystal SCs exhibited a remarkably large exciton binding energy of 360.3 ± 4.8 meV, leading to an ultrafast emission decay time of 0.97 ns, which is the smallest among all MHP materials. The material's theoretical coincidence time resolution was calculated to be 65.1 picoseconds (ps), indicating its potential for high-speed imaging applications.

3.2.2 Delayed Response Time

Delayed imaging detection is an indirect imaging technique that involves the temporary storage of incident radiation energy and its subsequent release under external stimulation, such as pressure, temperature, or laser, resulting in delayed mechanical luminescence (ML), thermally stimulated luminescence (TSL), and photo-stimulated luminescence (PSL) (Fig. 9a). These luminescence phenomena are special in that, after the excitation light source is removed, the scintillator materials can maintain a certain level of luminescence in a dark room under external stimuli, giving delayed imaging detection potential applications in long-term optical information storage. Thus, delayed response time of the scintillator ensures that the scintillator material continues to emit light after the X-ray source is off, effectively extending the imaging time window. In 2020, Xiaogang Liu et al. [143] synthesized $NaLuF_4$: Tb^{3+} NCs that exhibited persistent luminescence lasting for several days after X-ray irradiation was stopped. By combining the persistent X-ray luminescence performance with advanced computer graphics, they developed high-resolution 3D X-ray luminescence emission imaging technology, demonstrating the ability to overcome spatial detection constraints by leveraging the temporal dimension and achieve more precise acquisition of detection data from intricate geometries (Fig. 9b).

Xia et al. [144] achieved a significant breakthrough by first observing X-ray storage phenomena in MHPs, $CsCdCl_3$: Mn^{2+}, R^{4+} (R = Ti, Zr, Hf and Sn), after X-ray irradiation. It is demonstrated that X-ray storage capability can be effectively improved via site occupy manipulation and heterovalent substitution (Fig. 9c). Heterovalent substitution in Cd sites by R^{4+} broadens trap distributions and enhanced X-PersL performance. Finally, the integration of optimized storage scintillators onto flexible substrates has paved the way for 3D X-ray imaging under thermal stimulation (100 °C heating treatment) (Fig. 9d), effectively surpassing the constraints of traditional flat panel detectors. This work also demonstrates that the effective manipulation of trap centers through the introduction of impurity ions substitution can significantly enhance RL storage capacities. Subsequently, the strategic co-doping Dy^{3+} and Ag^{+} ions in $Cs_2NaLuCl_6$ crystals by occupying Na lattice sites showcases notable X-PersL characteristics, highlighting the effectiveness of this approach [74, 146]. Moreover, the Tb^{3+}-doped $Cs_2NaScCl_6$ SC exhibits an exceptional X-PersL lasting up to 12 h upon X-ray excitation termination, allowing it to be used in a radiation storage battery which has a linear scaling capacity with radiation does or intensity. These work demonstrated that the effective construction of trap centers through the introduction of impurity ions substitution has significantly enhanced RL storage capacities, leading to improved delayed detection performance and opening new avenues for flexible 3D X-ray imaging under thermal stimulation.

Beyond thermal stimulation for releasing these captured carriers, near-infrared (980 nm) laser and pressure stimuli can also be employed to release the captured carrier, giving rise to phenomena such as PSL and ML. Consequently, by evaluating the optical properties, such as the intensity of PSL or pressure-induced luminescence, equivalent success in detection has been achieved. In 2023, Wang et al. [145] developed lanthanide ions (Ho^{3+})-doped $NaLuF_4$ NCs as a delayed X-ray scintillator. It was developed that X-ray irradiation generates trapping centers in $NaLuF_4$: Ho^{3+} NCs, leading to ML upon mechanical stimulation after X-ray exposure (Fig. 9e). Additionally, the ML intensity correlates linearly with the X-ray dose, facilitating the detection of delayed X-ray does radiation. Furthermore, it has been

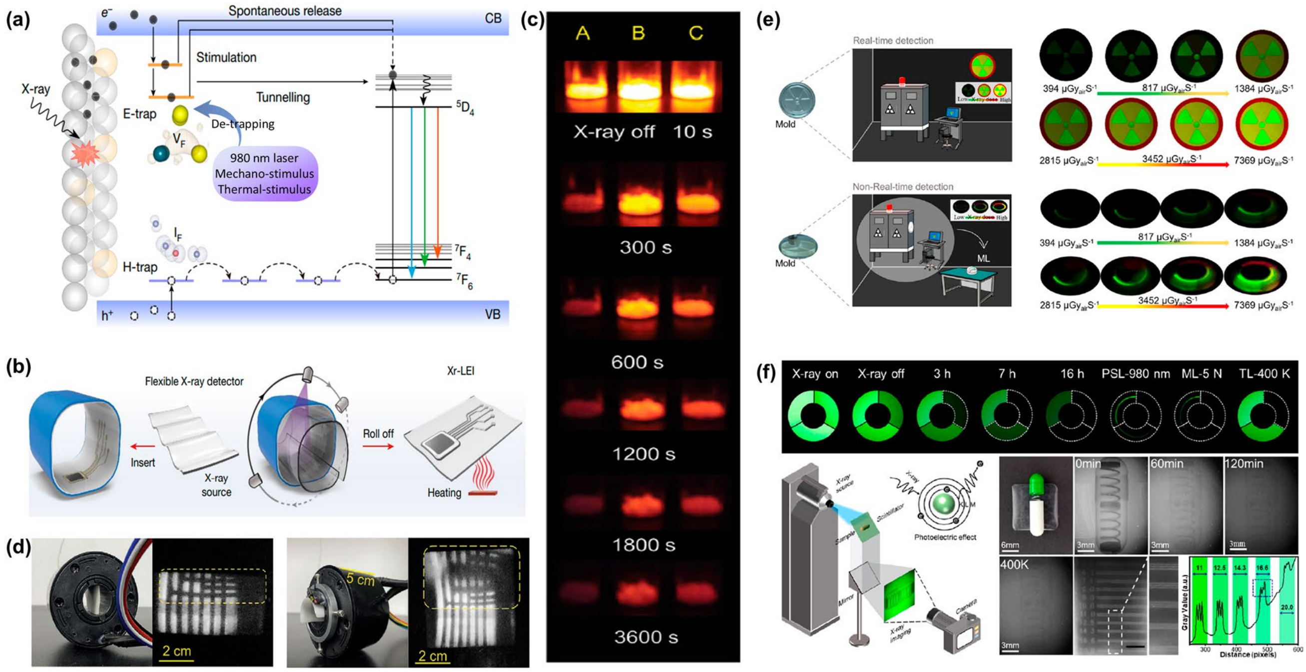

Fig. 9 Delayed X-ray performance of the scintillators. **a** Mechanism diagram of X-ray-induced multi stimulus-induced de-trapping process. **b** Schematic diagram showing non-destructive inspection of 3D curved objects enabled by X-PersL behavior of the scintillators. **c** X-PersL photographs of A) $CsCdCl_3$: 5%Mn^{2+}, B) $CsCdCl_3$: 5%Mn^{2+}, 0.1%Zr^{4+}, and C) $CsCdCl_3$: 5%Mn^{2+}, 0.1%Ti^{4+}. **d** TSL images of annulus electric conduction link using the flat panel (left) and curved panel $CsCdCl_3$: 5%Mn^{2+}, 0.1%Zr^{4+}@PDMS film (5 cm × 2.5 cm). The image read out temperature is 100 °C [144]. **e** Schematic diagram and photographs of the as-obtained $NaLuF_4$: Ho^{3+} NCs or real-time and delayed-time (ML) of X-ray dose detection [145]. **f** Photographs of the time-dependent X-PersL, PSL, and TSL features of the as-obtained $NaLuF_4$: Tb.$^{3+}$ NCs [109]

demonstrated that the delayed X-ray information can also be read out by thermal stimulation or 980 nm laser irradiation, endowing the system with multimodal readout capabilities (Fig. 9f) [109]. However, it is important to note that ML or PSL behavior has not yet been fully realized for perovskite scintillator due to their relatively low trap capture efficiency compared to fluorides. Future work should also focus on enhancing trap capture efficiency to improve the readout methods and accuracy of delayed X-ray detection.

3.3 Trade-off between Light Yield and Response Time

The optimization of MHP scintillators necessitates a nuanced balance between enhancing light yield and modulating response time, as strategies targeting one parameter often impose trade-offs on the other. This inherent trade-off arises from the fundamental physical mechanisms governing radiative recombination, carrier dynamics, and ET pathways. For instance, nanostructuring (e.g., QDs or nanoplatelets) and layered structures improve light yield by suppressing non-radiative recombination through quantum confinement, yet their high surface-to-volume ratio introduces surface defects that act as charge traps, which prolong carrier lifetimes by trapping charges [147]. These traps will delay the radiative recombination process, increasing response time. Similarly, STE-based scintillators (such as $Cu_3Cu_2I_5$) leverage large Stokes shifts (> 200 nm) to minimize self-absorption, achieving light yields exceeding 123,000 Ph MeV^{-1}. However, the soft lattice and strong exciton-phonon coupling responsible for STE formation also result in broad emission bands and slow recombination kinetics (0.734 μs) [4, 148]. The decay times of STE-dominated materials typically range from micros to millis (Table 2), rendering them unsuitable for applications requiring nanosecond-scale temporal resolution. Doping with activators (e.g., Mn^{2+} or lanthanide ions) or constructing ET channels (e.g., MHP-dye composites) effectively reduces self-absorption by decoupling absorption and emission spectra. For instance, Mn^{2+}-doped BA_2PbBr_4 achieves a light yield of 85,000 Ph MeV^{-1} but inherits the millisecond-scale decay time

© The authors https://doi.org/10.1007/s40820-025-01772-7

(727 μs) characteristic of Mn^{2+}'s $^4T_1 \rightarrow {}^6A_1$ transition [40]. Similarly, ET to organic dyes red-shifts emission but introduces additional recombination pathways governed by the dye's intrinsic lifetime, which may still lag behind pure MHP systems. Conversely, delayed detection methods (e.g., thermally/mechanically stimulated luminescence) enable high-resolution 3D imaging by extending the temporal window for signal acquisition. Materials like $CsCdCl_3$:Mn^{2+}, Zr^{4+} exhibit persistent luminescence for hours post-irradiation [144] facilitating complex geometry imaging. However, these systems inherently prioritize spatial resolution over speed, rendering them incompatible with real-time applications. Overall, the optimization of MHP scintillators constitutes an inherently multidimensional challenge, necessitating careful consideration of application-specific performance requirements. These requirements may include but are not limited to high-speed imaging capabilities, high-sensitivity detection thresholds, or delayed response characteristics in time-resolved detection systems. As such, future work must adopt a strategic approach to parameter optimization that carefully balances these competing demands while addressing the diverse operational requirements of modern X-ray detection technologies.

4 Radioluminescent Engineering Strategies

The integration of RL light engineering techniques into X-ray imaging technology, which is crucial for enhancing both resolution and contrast, represents a sophisticated and complex field. It revolves around the efficient manipulation and optimization of light conversion from X-rays to visible signals. Key aspects include the development of stacked techniques, the exploitation of the waveguide effect, and polarized RL; the enhancement of transparency and the innovation of flexible films are summarized as follows.

4.1 Stacked Technique

Traditional techniques rely on single-energy X-ray sources, forming images based on the degree of X-ray absorption by materials. However, this approach lacks the ability to provide information on the chemical composition or density within objects, limiting its accuracy and effectiveness in specific applications. To address this limitation, researchers have developed a stacked technique for multi-energy X-ray imaging (MEXI), which analyzes the attenuation of X-rays at various energy levels within an object [73]. Stacked scintillators combine layers of scintillator with distinct X-ray absorption characteristics and luminescent properties, enabling simultaneous detection across multiple energy spectra.

In 2022, Yang et al. [73] pioneered a multilayer stacked scintillator for large-area multispectral flat panel X-ray imaging (FPXI) (Fig. 10a). This method overcomes the limitations of traditional energy integration imaging by providing spectral information and enhancing image contrast. Here, the scintillator layers are carefully designed to have different X-ray absorption capabilities and RL wavelengths. The top layer is responsive to low-energy X-rays, emitting long-wavelength lights, while the bottom layer absorbs high-energy X-rays and produces short-wavelength lights (Fig. 10b). A prototype four-layer scintillator ($FAPbI_3$/$C_4H_{12}NMnCl_3$/$(C_8H_{20}N)_2MnBr_4$/$Cs_3Cu_2I_5$; Fig. 10c) successfully resolved a "bone muscle" phantom, demonstrating energy-dependent feature discrimination (Fig. 10d). Subsequently, Mohammed et al. [149] advanced the above strategy by devising a top filter bottom (TFB) sandwich architecture (Fig. 10e), incorporating quartz as a strategic filter. The layer filters strategically remove the energy range where the absorption tails of the upper and lower scintillators intersect, thereby ensuring a clearer distinction between their emission signatures. Illustratively, X-ray images obtained at varying voltages demonstrate the efficacy of the TFB design, where each layer effectively discriminates between low- and high-energy radiation through their characteristic luminescence, enabling the differentiation of material composition and achieving a resolution of approximately 18 lp mm^{-1}. Xiaoming Li et al. [150] further refined a TFB structure through meticulous modulation of scintillators, an innovation that not only elevates the performance of scintillating materials but also powerfully demonstrates the broad applicability of this technique. Recent advances by Mohammed et al. extended this paradigm to a six-layer MEXI system with interlayer optical filters (Fig. 10f) [93]. By strategically implementing interlayer filters, they ensure that the X-ray beam is tailored to pass only specific visible wavelengths to the respective scintillators, thereby maintaining non-overlapping RL. This critical design element allows each scintillator layer to capture unique, spectral signatures of the imaged object, enhancing both the clarity and precision of the data and achieving 22 lp mm^{-1} resolution across

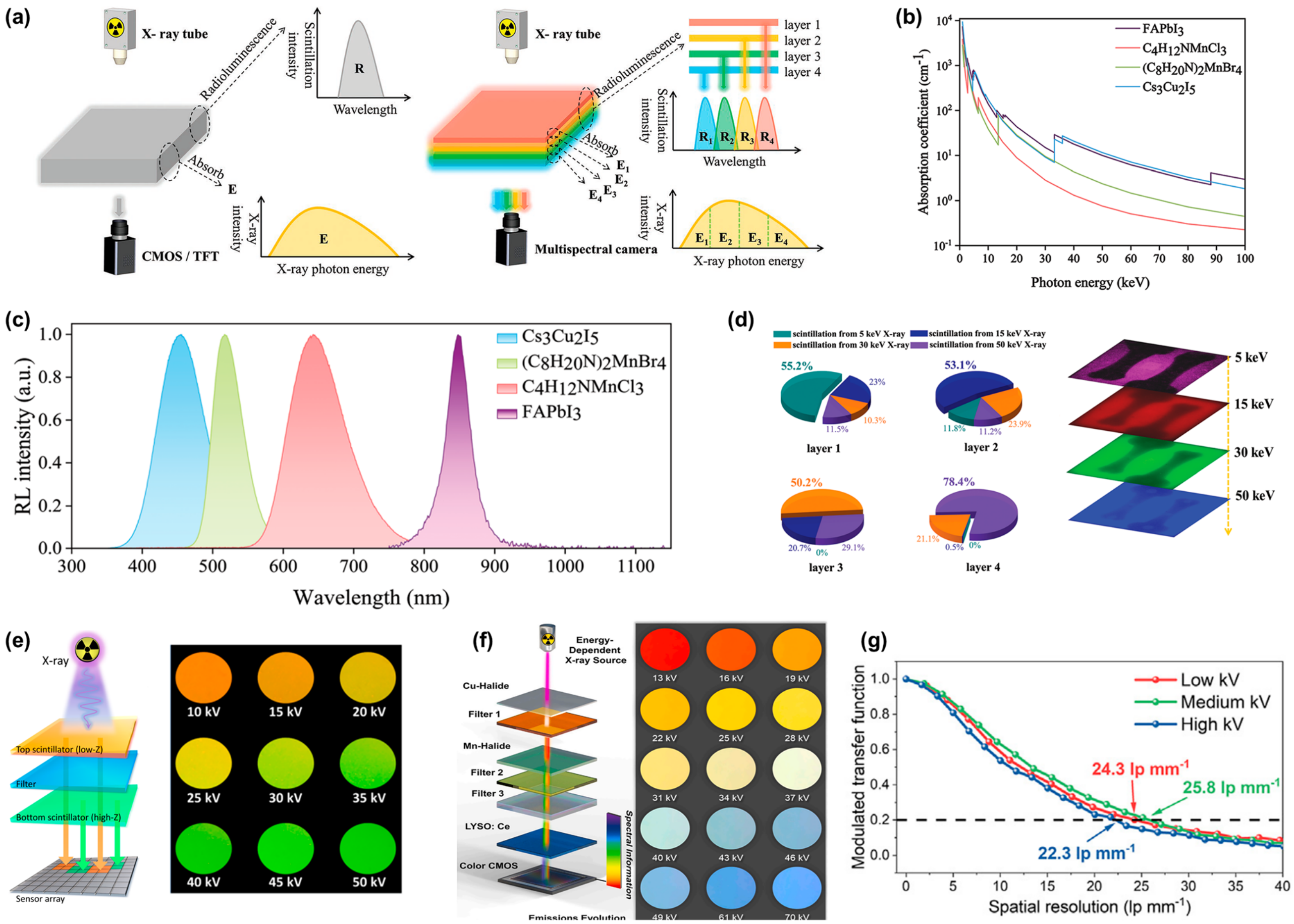

Fig. 10 Scintillator performances of stacked MHPs. **a** Schematic of a conventional energy-integrated X-ray imaging system and large-area multi-energy FPXI system based on stacked multilayer scintillators. **b** X-ray absorption coefficients of $FAPbI_3$, $C_4H_{12}NMnCl_3$, $(C_8H_{20}N)_2MnBr_4$ and $Cs_3Cu_2I_5$. **c** RL spectra of $FAPbI_3$, $C_4H_{12}NMnCl_3$, $(C_8H_{20}N)_2MnBr_4$, and $Cs_3Cu_2I_5$ scintillators. **d** The proportion of the four energy X-rays contributing to the light emitted by each scintillator and the corresponding multi-energy X-ray images at four energy channels at 5, 15, 30, and 50 keV [73]. **e** Schematic of the working principle and the corresponding color evolution of the TFB sandwich structure scintillator [149]. **f** Schematic of the working principle and the corresponding color evolution of the MEXI system featuring a six-layered architecture scintillator. **g** MTF curves of the MEXI system under low-, medium-, and high X-ray tube voltages [93]

low-to-high X-ray doses (Fig. 10g). However, increasing the number of layers can lead to mutual excitation between layers, which may affect the accurate discrimination of X-ray energy. To mitigate this, Yang et al. [151] proposed a strategy for a multi-energy X-ray detector based on quantum-cutting perovskite scintillators. By using Yb^{3+}-doped $CsPbCl_3$ NCs in the top layer, this design induced a 570 nm absorption–emission shift and > 100% photoluminescence PLQY, suppressing crosstalk while pairing with STE-based scintillators ($CsAgCl_2$/$Cs_3Cu_2I_5$) in lower layers. The resultant non-overlapping RL spectra significantly improved material discrimination, particularly for density-similar substances.

While stacked scintillator architectures achieve multi-energy discrimination through material stratification, parallel advancements in direct detection paradigms offer distinct approaches. Tang et al. [152] developed a vertical matrix perovskite detector with electrodes aligned parallel to the X-ray beam. Low-energy photons deposited energy in shallow layers, while high-energy photons penetrated deeper regions. Using $MAPbBr_3$ SCs with five vertically stacked electrodes and machine learning-derived conversion matrices, the system achieved single-shot density gradation imaging, distinguishing soft tissues from high-density composites with 0.81×10^5 μC Gy_{air}^{-1} cm^{-3} sensitivity and 0.82 μGy_{air} s^{-1} detection limits. Additionally, Shabbir et al.

© The authors
https://doi.org/10.1007/s40820-025-01772-7

[153] developed a solution-processed $Cs_{0\cdot1}FA_{0\cdot9}PbI_3$ perovskite thin-film detector for broadband multi-energy X-ray detection. The n-i-p diode architecture ($SnO_2/Cs_{0.1}FA_{0.9}PbI_3/$Spiro-OMeTAD/Au) exhibited 6×10^4 μC Gy^{-1} cm^{-2} sensitivity in hard X-rays (> 10 keV) with < 5 ms response times, and 5×10^3 μC Gy^{-1} cm^{-2} sensitivity in soft X-rays (0.1–10 keV) with 60 dB SNR at 1.2 keV.

4.2 Waveguide Effect

Waveguide effect, a physical phenomenon that controls the direction of photon propagation, has been proved to play a significant role in enhancing imaging resolution. By restricting lateral photon diffusion, it boosts the signal collection efficiency within the imaging system, thereby markedly improving resolution. Based on the principle of total internal reflection, where light incident at an angle greater than the critical angle on the interface between two media is reflected entirely within the higher refractive index medium, the waveguide effect enables light to propagate along interfaces without leakage (Fig. 11a). In X-ray scintillators, the design of nanostructures or microstructures with specific orientations facilitates the effective transmission and confinement of photons, thereby reducing lateral spread and enhancing imaging resolution.

In 2003, Eijk [157] laid the groundwork by suggesting the use of pixelated scintillator arrays embedded within a tailored matrix to hinder inter-pixel photon leakage, aiming to enhance spatial resolution. Building on this insight, Tang et al. [155] achieved a significant breakthrough by fabricating a $Cs_3Cu_2I_5$ array scintillator. They ingeniously integrated $Cs_3Cu_2I_5$ into an anodic aluminum oxide (AAO) matrix via a facile hot pressing process (Fig. 11b). The nanostructured AAO matrix is pivotal in constraining lateral light diffusion, thereby drastically reducing photon crossover between pixels. Notably, the fabricated $Cs_3Cu_2I_5$-AAO scintillator exhibits superior spatial resolution (10.4 lp mm^{-1}) (Fig. 11c). Yang et al. [158] further enhanced the resolution of the $Cs_3Cu_2I_5$ scintillator by optimizing the $Cs_3Cu_2I_5$-AAO fabrication process. This approach enables precise control over the length of the $Cs_3Cu_2I_5$ NWs by adjusting the pore depth of the AAO matrix, offering tunability in size. As a result, they achieved high-resolution imaging with a spatial resolution of 20 lp mm^{-1}. Zhang et al. [156] prepared pixelated $CsPbBr_3$-AAO array scintillation screens by adsorbing synthesized $CsPbBr_3$ NCs into the array voids of AAO via negative pressure filling. This method achieved an ultra-high spatial resolution of 211 lp mm^{-1}(Fig. 11d, e), further demonstrating the versatility of the AAO template approach for different pixelated MHPs scintillators. In addition to the aforementioned method of using an AAO template for alignment, Mohammed recently proposed the fabrication of a pixelated scintillator array through the integration of the low-temperature melting of manganese halide compounds within an aluminum-clad capillary template [154]. The as-obtained pixelated scintillator achieves remarkable spatial resolutions of 60.8 and 51.7 lp mm^{-1} at a MTF of 0.2, for 0.5 and 1 mm thicknesses, respectively (Fig. 11f).

Despite numerous accomplishments, the above processes often entail heating or melting, which can potentially harm the delicate perovskite crystal structure, subsequently compromising the scintillator's performance. Consequently, exploring alternative methods to safeguard the crystal integrity remains a pressing pursuit. Recently, Wang et al. [85] devised an innovative one-step in situ strategy for the growth of $Cs_5Cu_3Cl_6I_2$ QDs within AAO matrix, yielding a scintillator in the form of a $Cs_5Cu_3Cl_6I_2$@AAO array scintillator. This approach has led to the development of a pixelated scintillator array and boasts a spatial resolution of approximately 20 lp mm^{-1} and a remarkable detection sensitivity of 0.152 Gy s^{-1}.

4.3 Chiral Circularly Polarized Luminescence (CPL)

CPL materials exhibit differential intensities between left- and right-handed circularly polarized light, a trait pivotal for enhancing the resolution in imaging technologies (Fig. 12a). Conventional imaging techniques often suffer from inter-pixel crosstalk due to the isotropic propagation of light, which hampers significant improvements in resolution. The integration of CPL materials introduces a novel paradigm by generating light of a specific chirality that can be precisely controlled, thereby mitigating crosstalk and augmenting image contrast and resolution.

In recent years, advancements in organic–inorganic hybrid halide materials have propelled CPL research forward, with these materials boasting high PLQY and substantial circular polarization efficiencies (glum). Moreover, they have shown immense promise in the realm of X-ray detection and imaging. In 2022, Li et al. [159]

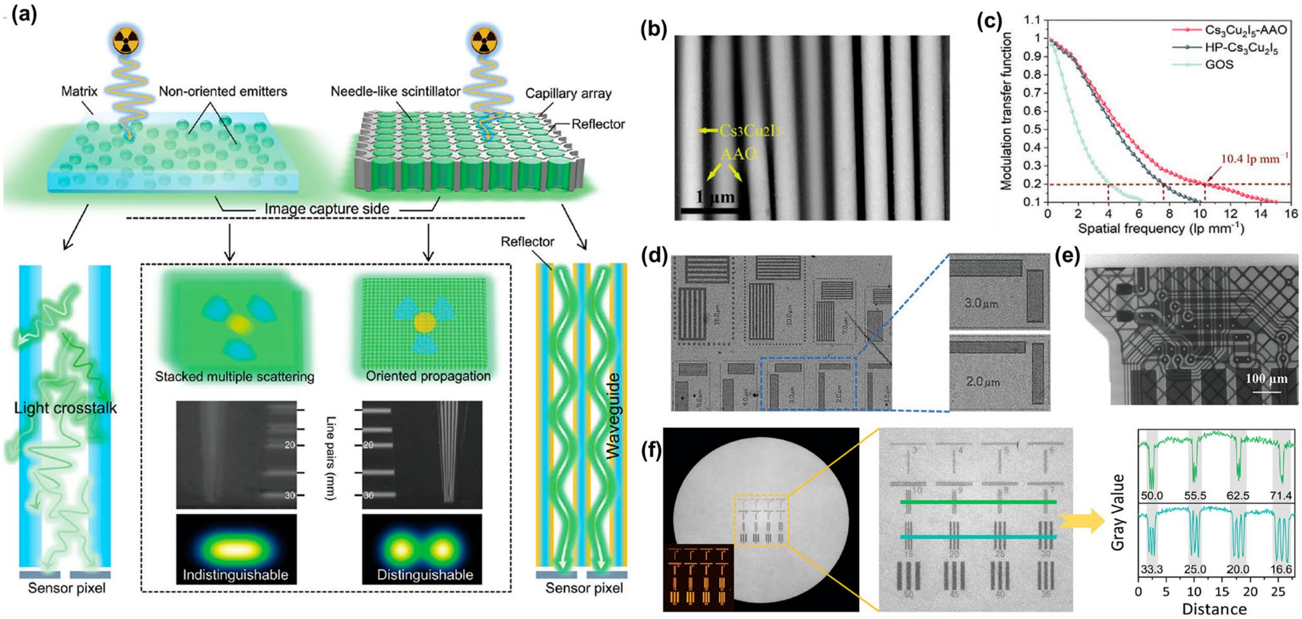

Fig. 11 Scintillator performances of waveguided MHPs. **a** Light propagation mechanisms and results of conventional nonstructured scintillators and structured capillary needle-like array scintillators in X-ray imaging [154]. **b** Cross-sectional SEM image of $Cs_3Cu_2I_5$-AAO scintillator. **c** The MTF values of $Cs_3Cu_2I_5$-AAO, HP-$Cs_3Cu_2I_5$, and GOS [155]. **d** Spatial resolution of the pixelated $CsPbBr_3$-AAO arrays scintillation. **e** X-ray imaging of memory card with the pixelated $CsPbBr_3$-AAO arrays [156]. **f** X-ray image of a microresolution chart. The right one is the gray value profiles along the cyan and green lines extracted from the X-ray image of the microresolution chart [154]

presented a pioneering strategy to enhance X-ray imaging clarity by employing chiral MHP scintillators that emit circularly polarized radioluminescence (CPRL). These scintillators, exemplified by (R-3AP)$PbBr_3Cl\cdot H_2O$ (R-3APP) and (S-3AP)$PbBr_3Cl\cdot H_2O$ (S-3APP) (Fig. 12b), showcase the distinctive attribute of circular polarization in its RL response to X-ray irradiation. To demonstrate the CPRL enhanced the imaging quality, they constructed a simple matrix that showcased the optical differences between traditional and chiral scintillators by using a homemade polarized light collecting system (Fig. 12c). Notably, the RL intensity of S-3APP and R-3APP displays a significant polarization dependence (Fig. 12d), suggesting that the RL is intrinsically polarized with asymmetric oscillations along the propagation direction. Finally, they assembled a series of chiral scintillators by alternating left-handed and right-handed crystals. Under X-ray exposure, this assembly exhibited a distinct contrast resolution, indicating a unique light propagation pattern for each crystal (Fig. 12e). This work successful demonstrated of the concept of chiral scintillators herein opens an avenue to controlling the RL propagation, potentially minimizing the optical crosstalk that has plagued the scintillator field for a long time.

Building on this foundation, Wang et al. [160] introduced chiral organic–inorganic hybrid Mn^{2+} halide clusters with exceptional PLQY and CPL characteristics. These clusters, designated (R/S-3-aminopyrrolidine dihydrochloride)$_6$(Mn_3Cl_{12})(Cl)$_6$ (R/S-1) and (R/S-1,2-diaminopropane dihydrochloride)$_3$(Mn_3Cl_{12})(R/S-2), were instrumental in advancing X-ray imaging applications, achieving high detection sensitivity and resolution. They also demonstrated that the directional arrangement of chiral ligands within these clusters was key to amplifying the CPL effect, underscoring the significance of structural design in enhancing material performance. Alexander et al. [161] synthesized chiral Mn^{2+} bromide hybrids that emit bright green CPL with near-unity PLQY and a high dissymmetry factor. These hybrids, combining $[MnBr_4]^{2-}$ anions with N/O–H bond-free cations, showcased excellent optical selectivity and a strong linear response to X-ray dose rate, positioning them as cost-effective candidates for CPL X-ray imaging.

In addition to indirect X-ray detection, Luo et al. [162] further expanded the horizons of self-powered direct X-ray

© The authors

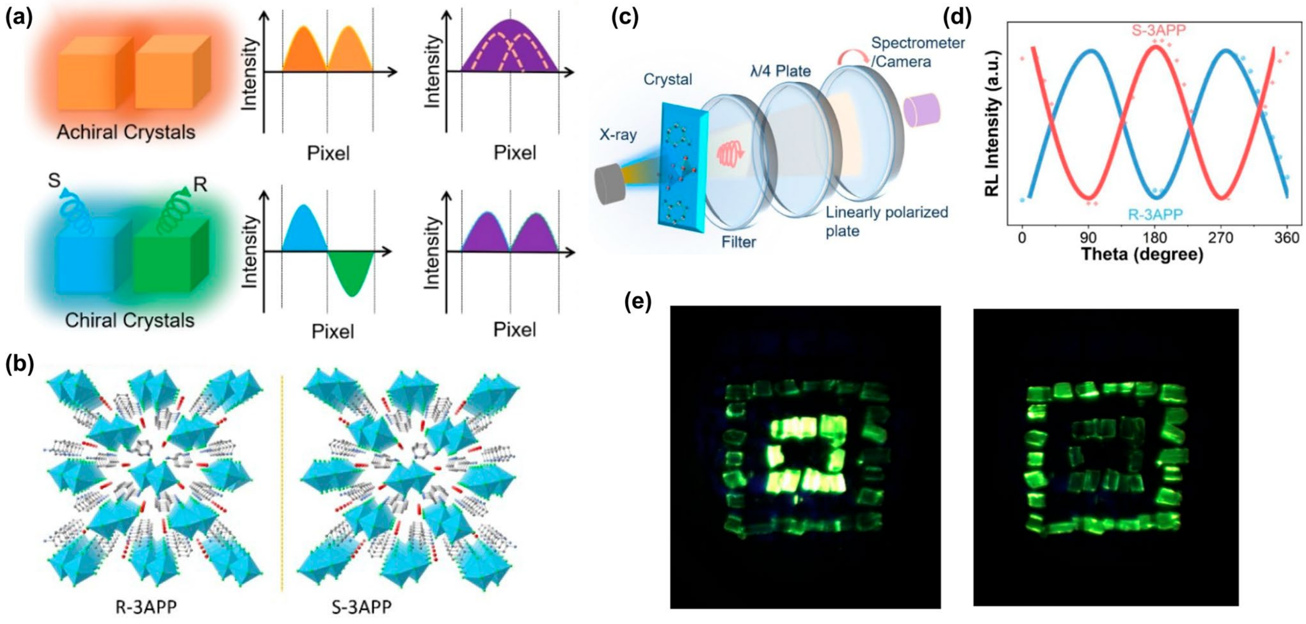

Fig. 12 Scintillator performances of CPL MHPs. **a** Conceptual illustration of the minimization of optical crosstalk by CPRL. **b** The crystal structures of R-3APP and S-3APP. **c** Schematic illustration of the experimental setup for verifying the CPRL measurement. **d** The polarization-dependent RL of chiral S-3APP and R-3APP. **e** The left-handed and right-handed RL emission crystals show bright and dark changes when rotating the linearly polarized plate [159]

detection with the development of a 2D lead-free double perovskite, R-MPA)$_4$AgBiI$_8$. This perovskite, which crystallizes in a polar space group at room temperature based on the introduction of chiral cations, results in a polar bulk photovoltaic effect under X-ray excitation, with an open-circuit voltage of 0.36 V. Without any external bias, the sensitivity and detection limit of the X-ray detection are measured to be of 46.3 μC Gy^{-1} cm^{-2} and 85 nGy$_{air}$ s^{-1}, respectively. Furthermore, under an applied bias of 50 V, the sensitivity is successfully enhanced to 946 μC Gy^{-1} cm^{-2}. This work represents a landmark in the advancement of "green" radiation detectors based on the CPL effect.

4.4 Enhancing Transparency

MHP SC scintillators have important application prospects in X-ray imaging, but due to their inherent impurity defects and the presence of polycrystalline interfaces, their transparency is low, which affects imaging resolution. Impurity defects are one of the common problems in perovskite materials, and their presence can scatter light, reducing the transparency of the material. Additionally, the presence of polycrystalline interfaces is also an important factor that affects the transparency of perovskite materials, as the interfaces can scatter light, reducing the transparency of the material. As a consequence, the resolution of imaging systems is compromised, with scattered light blurring the definition of image edges, reducing contrast, and thereby compromising the fine detail and sharpness of the final image [163, 164]. Therefore, improving the transparency of MHP SC scintillators is the key to improving the X-ray imaging resolution.

Recently, innovative research has suggested an approach to tackle the transparency issues by using the perovskite QDs as the scintillator. The key lies in the unique properties of these QDs, particularly their quantum size effect, which suppresses light scattering based on the Rayleigh scattering law. [165]. For instance, Ouyang et al. [166] developed a transparency X-ray scintillator by directly dispersing surface-modifying CsPbBr$_3$ NCs in a transparent polybutylmethacrylate (PBMA) matrix (Fig. 13a), achieving 99.2% PLQY, 70% visible transparency. This solution-processed scintillator screen exhibits high-contrast visualization at ultralow doses (4.6 μGy$_{air}$ s^{-1}). This universal dispersion approach demonstrates material-agnostic applicability, where transparent scintillators with tailored properties can be fabricated through rational selection of perovskite compositions (e.g., $CsPbX_3$, $Cs_3Cu_2I_5$) or transparent matrices (e.g., epoxy, PMMA, PVDF), establishing a versatile paradigm for radiation scintillators [55, 167, 168]. However, the direct integration of perovskite QDs into the transparent matrix is challenged by their propensity to aggregate during composite fabrication. Such aggregation can cause inconsistencies in light emission and scattering, leading to non-uniform light distribution within the film.

To overcome these limitations, Gu et al. [169] devised a vacuum-assisted "suction filtration" strategy to fabricate 30-µm-thick $CsPbBr_3$ NC films (Fig. 13b). This involved filtering perovskite NC solutions through PVDF membranes to form dense, uniform scintillator layers, followed by polystyrene (PS) gap-filling and transfer onto quartz substrates (Fig. 13c), with film thickness precisely tunable by adjusting NC solution concentration. This film not only has high density but also exhibits excellent transparency (Fig. 13d), with transparency exceeding 80% at a thickness of 30 µm. Using this ultrathin transparent perovskite scintillator film, the researchers successfully achieved a spatial resolution of approximately 862 nm, which is the highest resolution recorded to date for perovskite scintillators used in X-ray microscopy imaging. Additionally, Xu et al. [22, 38] developed a chemical anchoring strategy through one-step in situ growth of $CsPbBr_3$ QDs within transparent matrices. Here, $CsBr/PbBr_2$ precursors in DMF were mixed with PMMA colloids, forming intermediate clusters, and then polymer pre-curing and DMF evaporation triggered heterogeneous nucleation of perovskite NCs at these clusters, yielding a MHP film with uniformly dispersed perovskite NCs (Fig. 13e, f). This approach eliminates the light scattering caused by traditional physical blending, resulting in a homogeneous composite with high spatial resolution of 12.5 lp mm^{-1}. The universality of this methodology is further validated by its successful extension to copper-based perovskite $Cs_3Cu_2I_5$ [171]. The resulting scintillator achieves a record—high resolution of 14.3 lp mm^{-1} while maintaining comparable transparency. The perovskite QDs can also be grown from a transparent glassy network [22] and then yielded scintillators with an impressive spatial resolution of about 16.8 lp mm^{-1} and a rapid decay time of 27 ns. A crucial innovation in the above works lies in the nucleation inhibition strategy that suppresses crystal agglomeration and Ostwald ripening, ensuring uniform QD distribution. However, the pursuit of transparency introduces an inherent trade-off: The matrix materials, while enhancing light transmission, exhibit parasitic X-ray absorption. This energy loss mechanism reduces the scintillation light yield compared to perovskite single crystal.

To address the light yield transparency trade-off, transparent polycrystalline ceramics have emerged as a promising solution. For instance, Xia et al. [170] introduced an innovative technique, seed crystal-induced cold sintering (SCS) (Fig. 13g), for the fabrication of transparent MHP ceramic scintillators (Fig. 13h). This method yielded large-area, < 001 > -textured TPP_2MnBr_4 ceramics, and the textured poled samples atop surface direction exhibited enhanced linear transmittance for the visible light spectrum compared to the one at lateral surface direction. Finally, the as-obtained TPP_2MnBr_4 ceramics showcase exceptional performance with a light yield of approximately $78{,}000 \pm 2{,}000$ Ph MeV^{-1}. The scintillators demonstrated a remarkable energy resolution of 17% for high-energy γ-rays (662 keV) and a high-resolution X-ray imaging of 15.7 lp mm^{-1}. Building on these advancements, Xia et al. [172] further developed a melt-quenching method using a stoichiometric mixture of ethyltriphenylphosphonium bromide (ETPBr) and $MnBr_2$ as raw materials at a relatively low temperature of 200 °C to fabricate $(ETP)_2MnBr_4$-based polycrystalline ceramics. The resulting scintillator demonstrated high transparency (over 80% in the 500–800 nm range), a high light yield of $\approx 35{,}000 \pm 2{,}000$ Ph per MeV, a low detection limit of 10^3nGy s^{-1}, and a competitive spatial resolution of 13.4 lp mm^{-1} for X-ray imaging.

Overall, the quest to enhance transparency in MHP scintillators has driven significant innovations, from embedding QDs in transparent matrices to developing advanced polycrystalline ceramics. Each approach offers unique advantages, such as improved spatial resolution and light yield, while addressing critical challenges like light scattering and parasitic absorption. These advancements collectively pave the way for high-performance scintillators that can meet the stringent demands of modern X-ray imaging technologies, promising clearer, more detailed images with reduced radiation doses.

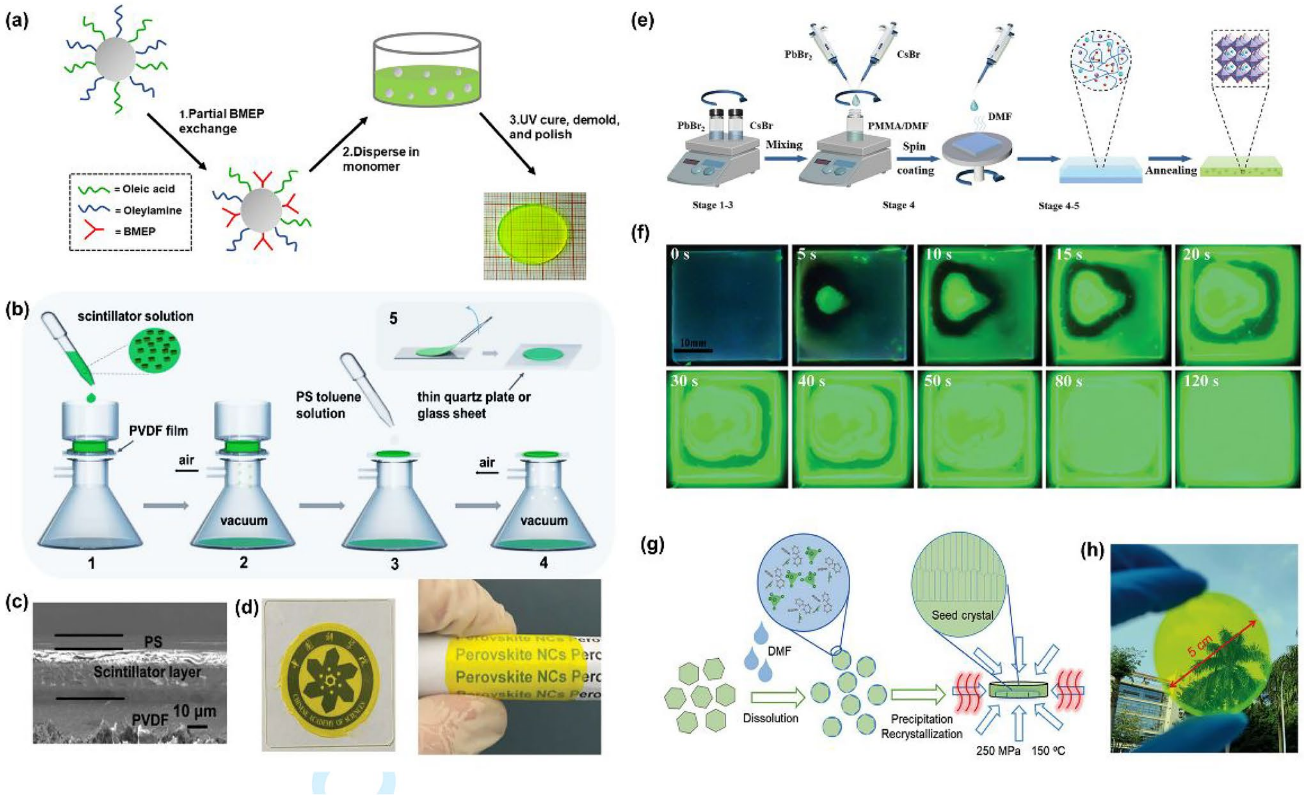

Fig. 13 Development of the transparent MHP scintillator. **a** Schematic diagram of the surface modification and polymerization process for preparing the $CsPbBr_3$/PBMA nanocomposites [166]. **b** Scheme of the scintillator film synthesis procedure by the suction filtration method and the corresponding **c** SEM and **d** optical images [169]. **e** Schematic diagram of the in situ growth of $CsPbBr_3$-based polymer–ceramics. **f** Photographs of the one-step in situ growth of $CsPbBr_3$ QDs from transparency matrix under UV illumination [38]. **g** Fabrication process of TPP_2MnBr_4 ceramic scintillator via the SCS process. **h** Photographs of as-obtained TPP_2MnBr_4 ceramic scintillator [170]

4.5 Curved Scintillator Imaging

Traditional imaging methodologies, predominantly grounded in planar imaging, have proved their efficacy in a wide array of applications. However, when it comes to non-destructive testing of intricate, curved, or anisotropic structures, the limitations of planar imaging become apparent, particularly at the edges. In planar imaging, the quality of the image decreases from the center to the edge due to the angle at which photons hit the outer pixels, a phenomenon known as vignetting. Typically, a series of optical lenses are employed to combat vignetting, but this approach results in a bulkier and more complex optical system. In response to these challenges, the development of curved imaging technology based on flexible scintillators has emerged as a promising solution. Curved scintillator imaging technology simplifies the imaging system and mitigates the vignetting effect at the edges, thereby excelling in non-destructive testing of complex structures. Gelinck et al. [173] proposed a concept of flexible imaging technology with a high-resolution curved image sensor made directly on a thin plastic substrate using organic photodetectors (OPD). As a proof of concept, the curved digital detector, combined with a flexible scintillator, demonstrates more uniform image quality. Moreover, Wang et al. [160] utilized the Monte Carlo method to elucidate the imaging performance of flexible $CsPbBr_3$ detectors, theoretically substantiating their superior performance over conventional NaI and CsI-based flat panel detectors in terms of resolution, peak-to-total ratio, and total efficiency (Fig. 14a). However, despite the promising theoretical framework, there has been a notable absence of tangible device or experimental progress in this area.

Until 2021, Xu et al. [38] introduced a novel approach, fabricating flexible MHP QDs-based scintillator materials through in situ crystallization within polymers. The obtained polymer–ceramic film showcases remarkable flexibility,

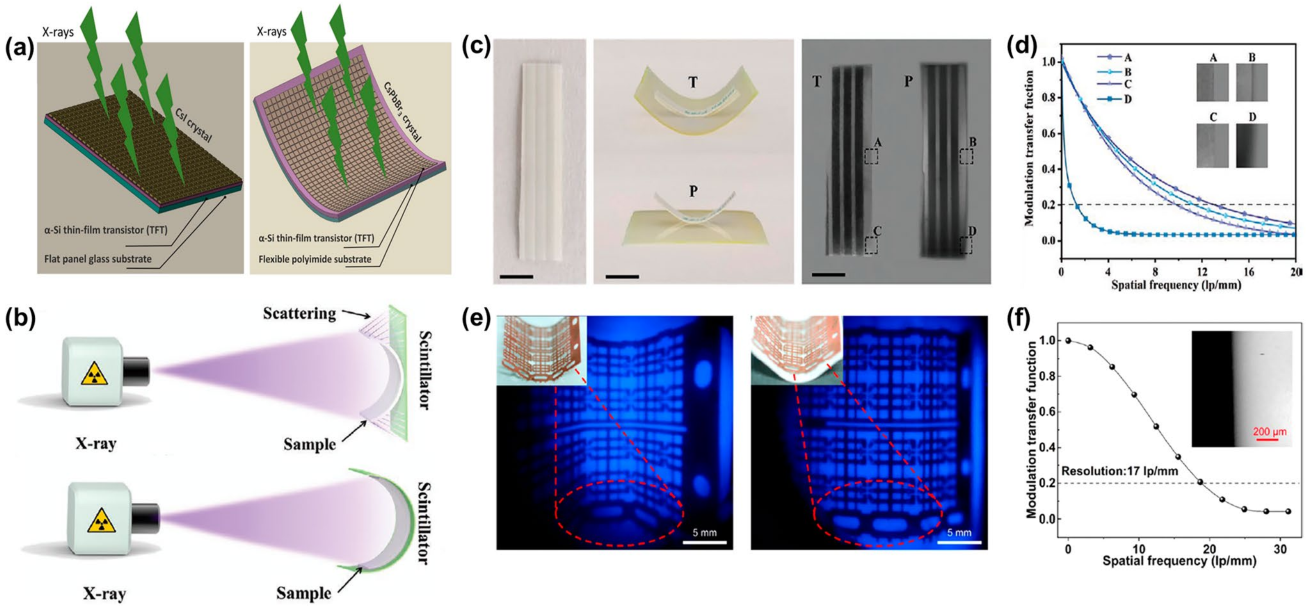

Fig. 14 Scintillator performances of curved MHPs. **a** Detector structure sketches: fat panel glass substrate and a flexible polyimide substrate [160]. **b** The diagram of the X-ray imaging under flat and bending states. **c** The difference of the corresponding indirect X-ray imaging ways, and the corresponding X-ray images of a bend target with the attached and projection imaging, respectively, and **d** their corresponding MTF of the specified location (A, B, C, and D) of the target [38]. **e** X-ray images of flexible copper grid taken by flexible $Cs_2Cu_2I_5$ film under flat and bending states. **f** MTF of the flexible $Cs_2Cu_2I_5$ film [174]

enduring bending to 90° without fracture, enabling X-ray detection on curved surfaces (Fig. 14b), as opposed to conventional projection imaging. This bypasses the scattering issue inherent in projection imaging for non-planar targets due to the gap between the target and scintillator. A comparison of imaging qualities using the attached (T) versus projection (P) methods (Fig. 14c), using a flexible circuit board, shows marked differences, particularly at locations A, B, C, and D. The MTF analysis highlights a substantial resolution disparity, with C achieving 9.5 lp mm^{-1} and D at 1.98 lp mm^{-1}, underscoring the superior spatial resolution performance of curved scintillator imaging in non-planar X-ray detection (Fig. 14d). Subsequently, we achieved in situ crystallization of $Cs_3Cu_2I_5$ perovskite within a PVDF/PMMA polymer matrix and on cellulose paper, fabricating copper-based perovskite flexible scintillators [171]. This enabled successful high-resolution imaging, thereby further affirming the significance of flexible scintillators for the detection of non-planar objects, highlighting their potential in versatile imaging applications. Additionally, Zhang et al. [175] demonstrated that in situ fabricated (TBA)CuX_2/PVDF flexible films were efficient scintillation screens for flexible X-ray imaging, with the spatial resolution of 166 μm achieved.

In addition to the in situ growth of MHP from a flexible matrix to form a flexible scintillator, other methods, such as directly combining MHP with a polymer matrix, have been explored. However, these methods often suffer from the issue of particle aggregation. To address this challenge, Omar F. Mohammed et al. [174] proposed a solution involving the addition of ethylacetate (EA). By incorporating EA, a highly uniform flexible $Cs_2Cu_2I_5$ film can be fabricated through either the spin-coating or blade-coating method. The presence of EA effectively inhibits the aggregation of $Cs_2Cu_2I_5$ particles, resulting in a highly uniform flexible scintillator film that exhibits nearly 100% PLQYs (Fig. 14e). These films have demonstrated very promising scintillation properties, including a low detection limit of 48.6 nGy$_{air}$ s^{-1} and an X-ray imaging resolution of 17 lp mm^{-1} (Fig. 14f). Moreover, Wu et al. [176] proposed that the $(BTPP)_2MnCl_4$@PDMS flexible scintillation screens achieve a high spatial resolution of 14.1 lp mm^{-1} and realize high-quality imaging results of non-planar objects. Xiao et al. reported a novel 2D RP phase Cs_2CdCl_4: Mn^{2+}, with the cooperation of PDMS matrix, which shows a high light

© The authors

yield up to 88,138 Ph MeV^{-1} and a high spatial resolution of 16.1 lp mm^{-1}. Overall, the development of flexible scintillator materials has revolutionized X-ray imaging, particularly for non-planar targets, by offering high light yields and exceptional spatial resolutions.

5 Conclusions and Perspectives

To sum up, MHP scintillators have emerged as a transformative class of materials for high-resolution X-ray detection, distinguished by their exceptional X-ray attenuation capabilities, near-unity luminescence efficiency, tunable emission spectra, and ultrafast decay kinetics. These intrinsic advantages, coupled with their structural versatility and cost-effective processability, have driven unprecedented advancements in radiation detection technologies. Diverging from prior reviews, this work provides a systematic framework for understanding and optimizing MHP scintillators through two complementary lenses: intrinsic property modulation and RL engineering strategies. First, we elucidate the fundamental luminescence mechanisms governing MHP scintillators—excitonic recombination, STE emission, TADF, and LPRL—and correlate these processes with material design principles. Subsequently, the paper meticulously reviews strategies to boost the light yield of MHP scintillators, such as employing confinement effects, improving crystalline, and reducing self-absorption. Concurrently, response time modulation is addressed, highlighting the critical balance between rapid decay (e.g., nanosecond decay time for real-time angiography) and delayed luminescence (e.g., trap-mediated storage for 3D tomographic imaging). Beyond intrinsic properties, we pioneer discussions on innovative light management architectures, such as stacked scintillators for multi-energy spectral discrimination, pixelated waveguide arrays to suppress optical crosstalk, and CPRL for contrast-enhanced imaging. The integration of flexible MHP composites further expands their applicability to curved surfaces and complex geometries. However, numerous critical challenges remain unresolved for practical implementation, following the technical roadmap presented there (Fig. 15); we discuss the research challenges that must be resolved to enable successful industrial application and identify some technologies that need to developed to address these challenges.

(1) The pursuit of practical applications of MHP scintillators demands urgent resolution of environmental concerns, as lead-based systems, despite their superior light yield and ultrafast decay times—pose significant ecological risks due to inherent lead toxicity. Recent advances in lead-free alternatives, such as Mn^{2+}/Cu^{+}-activated perovskites (e.g., $Cs_3Cu_2I_5$, Rb_2CuBr_3) [4, 158], demonstrate promising ultrahigh light yields, yet their decay times generally lag behind lead-based counterparts due to distinct recombination mechanisms: Strong spin–orbit coupling in lead-based MHPs enables fast radiative transitions, whereas lead-free systems predominantly rely on STE emission with inherently prolonged lifetimes. This fundamental trade-off among light yield, toxicity mitigation, and temporal response necessitates application-specific optimization. For instance, medical CT imaging prioritizes sub-10 ns decay and high resolution, while security screening may tolerate slower kinetics (> 50 ns) for enhanced environmental safety. Therefore, future research must implement a holistic strategy for parameter optimization that systematically reconciles competing performance metrics while addressing the multifaceted operational requirements of next-generation X-ray detectors across diverse applications.

(2) Suppressing defect formation is critical for optimizing the performance of MHP SCs and NCs. However, achieving efficient defect engineering remains a significant challenge. This stems from the intrinsically low formation energy and uncontrolled nucleation kinetics during solution-based synthesis of MHPs, which promote the formation of structural defects such as lead vacancies, halide interstitials, and grain boundaries. These defects result in high defect densities in synthesized scintillators, severely degrading key performance metrics, including light yield, response speed, and environmental stability. Studying the nucleation of MHP, including the critical nucleation pathways and pinpoint defect origins (e.g., twinning, dislocations), can guiding rational control over scintillator fabrication. Therefore, further work should also be focused on the using some advanced technique, such as liquid-cell in situ TEM or SEM technique, for monitoring the detailed nucleation process of MHP. Complementing experimental efforts, machine learning and artificial intelligence, driven material design, offer transformative potential. Future research should prioritize the integration of machine learning and AI-driven approaches, specifically by combining perovskite crystal databases (e.g., Materials Project) with graph neural networks (GNNs). This methodology can systematically predict

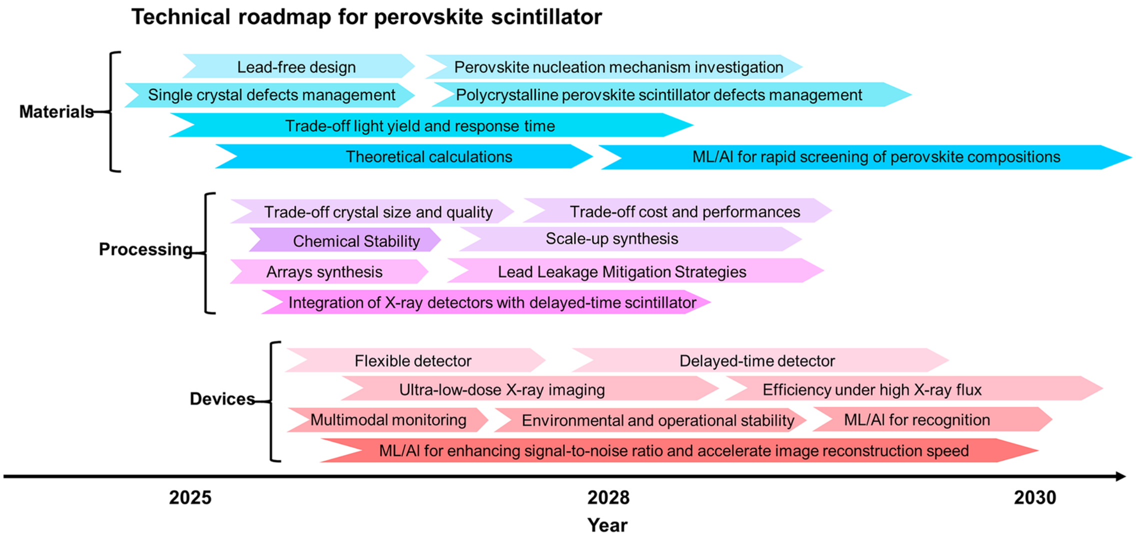

Fig. 15 Technical roadmap of perovskite scintillators over the next five years. ML, mechanical learning; Al, artificial intelligence

perovskite compositions that optimize both formation energy and defect tolerance metrics, ultimately enabling accelerated design of high-performance scintillators with tailored functional properties.

(3) Current efforts to enhance MHP through above-mentioned chemical engineering or light management methods primarily focus on the preparation of films, MCs or NCs. For films, the presence of numerous crystal interfaces and defects at these interfaces can lead to reduced light yield and increased light scattering losses. For MCs or NCs, researchers mainly use a method of combining them with polymers to prepare so-called uniform films for scintillator screens. However, MCs can cause significant aggregation issues and light scattering losses, while NCs, due to their high surface area, have enormous surface defects that lead to a noticeable reduction in light yield. More importantly, when combined with polymers, the absorption of X-rays or other high-energy rays (such as α or β rays) by the polymers can also result in the absorption of a portion of the radiation energy, further reducing the light yield. These size limitations not only affect the optical performance of MHP materials but also limit their efficiency and reliability in practical applications. Therefore, developing new preparation methods and technologies to simultaneously reduce interface grains, minimize light scattering losses, and enhance light yield is a crucial direction for current research. Additionally, the preparation of MHP SCs can effectively address the issues mentioned above. However, current strategies for enhancing MHP SCs X-ray behaviors are still limited. Future research should focus on optimizing crystal growth protocols (e.g., Bridgman methods) and hybrid architectures (e.g., perovskite-polymer/CG composites) to enhance light yield and suppress scattering.

(4) The operational stability of MHP scintillators faces critical challenges from environmental stressors (moisture/heat) and irradiation-induced degradation. While hygroscopicity-driven defect proliferation remains a primary failure mechanism, current research primarily focuses on encapsulation strategies using polymer matrices (e.g., PMMA/PVDF) or in situ synthesis of MHPs NCs to enhance environmental resistance. However, these approaches predominantly assess PL stability while critically overlooking radiation tolerance under high-dose X-ray exposure. A fundamental limitation arises from radiation-polymer interactions: High-energy photons (X/β-rays) induce bond cleavage in organic matrices, generating free radicals that accelerate material degradation. Recent advancements like in situ growth of MHPs QDs in glass networks (MHPs CG) address polymer limitations but introduce new vulnerabilities—radiation-induced structural disordering in glass compromises long-term imaging reliability. Therefore, future efforts must concurrently pursue two pathways: (i) radiation-hardened encapsulation systems resistant to cumulative radiation damage and (ii) development of intrinsically stable perovskite architectures through defect engineering and composition optimization, with mandatory validation under high radiation doses irradiation.

(5) MHP scintillators' delayed X-ray detection capability enables offline imaging in complex geometries (e.g., radioactive pipelines) or hazardous environments (e.g., nuclear accident sites) through carrier trap-mediated energy storage. However, the inherent carrier trap recombination dynamics introduce prolonged decay time characteristics (ranging from minutes to hours), which inevitably compromise imaging quality through progressive signal blurring and spatial resolution degradation. This challenge requires developing advanced light management methods coupled with image processing algorithms that strategically compromise between delayed detection capacity and imaging resolution enhancement. Moreover, current methods for reading out the light signals to achieve delayed detection primarily involve pressure, laser, and heating techniques. To bridge this implementation gap, future research must prioritize the integration of MHPs scintillators with compact detector for delayed signal extraction and temporal–spatial correlation processing.

(6) Machine learning and artificial intelligence are revolutionizing the field of X-ray detection by reducing image SNR and accelerating image recognition speed, significantly enhancing production efficiency and detection accuracy. On the one hand, deep learning-based image denoising algorithms, such as convolutional neural networks (CNNs) and generative adversarial networks (GANs), can automatically identify and remove noise from images while preserving important structural information, thereby improving the SNR of images. Adaptive filtering techniques, along with data augmentation and regularization methods, further enhance the robustness and generalization capabilities of image processing. On the other hand, deep learning models can rapidly extract key features from images, and optimized lightweight network architectures combined with hardware acceleration technologies enable real-time processing of X-ray images, driving the automation of the entire workflow from image acquisition to diagnostic result generation. Future work should focus on integrating these technologies to further enhance detection precision and efficiency while addressing computational complexity and model interpretability challenges.

Acknowledgements This work was financially supported by the National Nature Science Foundation of China (NSFC) (U2241236, 1220041913, 52473253), the National Key Research and Development Program of China (2022ZDZX0007), Fundamental Research Open Subject Grant Program of Yantai Advanced Materials and Green Manufacturing Laboratory of Shandong Province (AMGM2024F15), Yunnan Major Scientific and Technological Projects (202402AB080011).

Author Contributions Ting Wang, Xiaoping Ouyang, Guoqiang Zeng, and Xuhui Xu contributed substantially to content discussions. Ting Wang prepared the original manuscript draft. Ting Wang and Xuhui Xu assisted in Fig. preparation. Yang Yang, Zhi Yang, Tianchi Wang, Hao Li, Lulu Han, and Yu Xue participated in manuscript revision.

Declarations

Conflict of Interest The authors declare no interest conflict. They have no known competing financial interests or personal relationships that could have appeared to influence the work reported in this paper.

Open Access This article is licensed under a Creative Commons Attribution 4.0 International License, which permits use, sharing, adaptation, distribution and reproduction in any medium or format, as long as you give appropriate credit to the original author(s) and the source, provide a link to the Creative Commons licence, and indicate if changes were made. The images or other third party material in this article are included in the article's Creative Commons licence, unless indicated otherwise in a credit line to the material. If material is not included in the article's Creative Commons licence and your intended use is not permitted by statutory regulation or exceeds the permitted use, you will need to obtain permission directly from the copyright holder. To view a copy of this licence, visit http://creativecommons.org/licenses/by/4.0/.

References

1. X. Ou, X. Chen, X. Xu, L. Xie, X. Chen et al., Recent development in X-ray imaging technology: future and challenges. Research **2021**, 9892152 (2021). https://doi.org/10.34133/2021/9892152
2. Y. Wu, J. Feng, Z. Yang, Y. Liu, S. Liu, Halide perovskite: a promising candidate for next-generation X-ray detectors. Adv. Sci. **10**(1), 2205536 (2023). https://doi.org/10.1002/advs.202205536
3. J. Liu, B. Shabbir, C. Wang, T. Wan, Q. Ou et al., Flexible, printable soft-X-ray detectors based on all-inorganic perovskite quantum dots. Adv. Mater. **31**(30), e1901644 (2019). https://doi.org/10.1002/adma.201901644
4. B. Yang, L. Yin, G. Niu, J.-H. Yuan, K.-H. Xue et al., Lead-free halide Rb_2CuBr_3 as sensitive X-ray scintillator. Adv. Mater. **31**(44), 1904711 (2019). https://doi.org/10.1002/adma.201904711
5. Q. Zhou, W. Li, J. Xiao, A. Li, X. Han, Low-dimensional metal halide for high performance scintillators. Adv. Funct. Mater. **34**(38), 2402902 (2024). https://doi.org/10.1002/adfm.202402902
6. Y.C. Kim, K.H. Kim, D.Y. Son, D.N. Jeong, J.Y. Seo et al., Printable organometallic perovskite enables large-area,

low-dose X-ray imaging. Nature **550**(7674), 87–91 (2017). https://doi.org/10.1038/nature24032

7. K. Dong, T. Jiang, G. Chen, H. Cui, S. Wang et al., Light management in 2D perovskite toward high-performance optoelectronic applications. Nano-Micro Lett. **17**(1), 131 (2025). https://doi.org/10.1007/s40820-024-01643-7
8. S. Tsuda, K. Saito, Spectrum–dose conversion operator of NaI(Tl) and CsI(Tl) scintillation detectors for air dose rate measurement in contaminated environments. J. Environ. Radioact. **166**, 419–426 (2017). https://doi.org/10.1016/j.jenvrad.2016.02.008
9. V.V. Nagarkar, T.K. Gupta, S. Miller, Y. Klugarman, M.R. Squillante et al., Structured CsI(Tl) scintillators for X-ray imaging applications. In 1997 IEEE nuclear science symposium conference record. November 9-15, 1997, Albuquerque, NM, USA. IEEE, (1997), 226–230
10. C. Greskovich, S. Duclos, Ceramic scintillators. Annu. Rev. Mater. Sci. **27**, 69–88 (1997). https://doi.org/10.1146/annurev.matsci.27.1.69
11. C. Michail, V. Koukou, N. Martini, G. Saatsakis, N. Kalyvas et al., Luminescence efficiency of cadmium tungstate ($CdWO_4$) single crystal for medical imaging applications. Crystals **10**(6), 429 (2020). https://doi.org/10.3390/cryst10060429
12. C. Michail, I. Valais, I. Seferis, N. Kalyvas, S. David et al., Measurement of the luminescence properties of Gd_2O_2S: Pr, Ce, F powder scintillators under X-ray radiation. Radiat. Meas. **70**, 59–64 (2014). https://doi.org/10.1016/j.radmeas.2014.09.008
13. S. Blahuta, B. Viana, A. Bessière, E. Mattmann, B. LaCourse, Luminescence quenching processes in Gd_2O_2S: Pr^{3+}, Ce^{3+} scintillating ceramics. Opt. Mater. **33**(10), 1514–1518 (2011). https://doi.org/10.1016/j.optmat.2011.02.040
14. G. Borghi, B.J. Peet, V. Tabacchini, D.R. Schaart, A 32 mm × 32 mm × 22 mm monolithic LYSO: Ce detector with dual-sided digital photon counter readout for ultrahigh-performance TOF-PET and TOF-PET/MRI. Phys. Med. Biol. **61**(13), 4929 (2016). https://doi.org/10.1088/0031-9155/61/13/4929
15. D.N. ter Weele, D.R. Schaart, P. Dorenbos, Comparative study of Co-doped and non Co-doped LSO: Ce and LYSO: Ce scintillators for TOF-PET. IEEE Trans. Nucl. Sci. **62**(3), 727–731 (2015). https://doi.org/10.1109/TNS.2015.2431295
16. H. Wu, Y. Ge, G. Niu, J. Tang, Metal halide perovskites for X-ray detection and imaging. Matter **4**(1), 144–163 (2021). https://doi.org/10.1016/j.matt.2020.11.015
17. S. Yakunin, M. Sytnyk, D. Kriegner, S. Shrestha, M. Richter et al., Detection of X-ray photons by solution-processed lead halide perovskites. Nat. Photonics **9**(7), 444–449 (2015). https://doi.org/10.1038/nphoton.2015.82
18. K. Shibuya, M. Koshimizu, Y. Takeoka, K. Asai, Scintillation properties of $C_6H_{13}NH_3)_2PbI_4$: exciton luminescence of an organic/inorganic multiple quantum well structure compound induced by 20 MeV protons. Nucl. Instrum. Meth. Phys. Res. Sect. B Beam Interact. Mater. At. **194**(2), 207–212 (2002). https://doi.org/10.1016/S0168-583X(02)00671-7
19. M.D. Birowosuto, D. Cortecchia, W. Drozdowski, K. Brylew, W. Lachmanski et al., X-ray scintillation in lead halide perovskite crystals. Sci. Rep. **6**, 37254 (2016). https://doi.org/10.1038/srep37254
20. F. Zhou, Z. Li, W. Lan, Q. Wang, L. Ding et al., Halide perovskite, a potential scintillator for X-ray detection. Small Meth. **4**(10), 2000506 (2020). https://doi.org/10.1002/smtd.202000506
21. J.H. Heo, D.H. Shin, J.K. Park, D.H. Kim, S.J. Lee et al., High-performance next-generation perovskite nanocrystal scintillator for nondestructive X-ray imaging. Adv. Mater. (2018). https://doi.org/10.1002/adma.201801743
22. H. Zhang, Z. Yang, M. Zhou, L. Zhao, T. Jiang et al., Reproducible X-ray imaging with a perovskite nanocrystal scintillator embedded in a transparent amorphous network structure. Adv. Mater. **33**(40), 2102529 (2021). https://doi.org/10.1002/adma.202102529
23. H. Li, Y. Zhang, M. Zhou, H. Ding, L. Zhao et al., A solar-blind perovskite scintillator realizing portable X-ray imaging. ACS Energy Lett. **7**(9), 2876–2883 (2022). https://doi.org/10.1021/acsenergylett.2c01440
24. G.E. Eperon, K.H. Stone, L.E. Mundt, T.H. Schloemer, S.N. Habisreutinger et al., The role of dimethylammonium in bandgap modulation for stable halide perovskites. ACS Energy Lett. **5**(6), 1856–1864 (2020). https://doi.org/10.1021/acsenergylett.0c00872
25. E. Oksenberg, A. Merdasa, L. Houben, I. Kaplan-Ashiri, A. Rothman et al., Large lattice distortions and size-dependent bandgap modulation in epitaxial halide perovskite nanowires. Nat. Commun. **11**(1), 489 (2020). https://doi.org/10.1038/s41467-020-14365-2
26. K. Kim, H. Kim, J. Park, Bandgap modulation of Cs_2AgInX_6 (X = Cl and Br) double perovskite nano- and microcrystals *via* Cu^{2+} doping. ACS Omega **6**(41), 26952–26958 (2021). https://doi.org/10.1021/acsomega.1c03290
27. F. Ruf, P. Rietz, M.F. Aygüler, I. Kelz, P. Docampo et al., The bandgap as a moving target: reversible bandgap instabilities in multiple-cation mixed-halide perovskite solar cells. ACS Energy Lett. **3**(12), 2995–3001 (2018). https://doi.org/10.1021/acsenergylett.8b01857
28. Z. Wang, J. Qiu, X. Wang, Z. Zhang, Y. Chen et al., Two-dimensional light-emitting materials: preparation, properties and applications. Chem. Soc. Rev. **47**(16), 6128–6174 (2018). https://doi.org/10.1039/c8cs00332g
29. A. Xie, F. Maddalena, M.E. Witkowski, M. Makowski, B. Mahler et al., Library of two-dimensional hybrid lead halide perovskite scintillator crystals. Chem. Mater. **32**(19), 8530–8539 (2020). https://doi.org/10.1021/acs.chemmater.0c02789
30. A. Wibowo, M.A.K. Sheikh, L.J. Diguna, M.B. Ananda, M.A. Marsudi et al., Development and challenges in perovskite scintillators for high-resolution imaging and timing applications. Commun. Mater. **4**, 21 (2023). https://doi.org/10.1038/s43246-023-00348-5

31. M. Moszynski, M. Kapusta, M. Mayhugh, D. Wolski, S.O. Flyckt, Absolute light output of scintillators. IEEE Trans. Nucl. Sci. **44**(3), 1052–1061 (1997). https://doi.org/10.1109/23.603803
32. S. Liu, F. Jiang, E. Song, P. Li, W. Liu et al., Controllable preparation and enhanced luminescence of Tb^{3+}-activated transparent gadolinium-rich silicate glass ceramic scintillator. Ceram. Int. (2025). https://doi.org/10.1016/j.ceramint.2025.01.413
33. T. He, Y. Zhou, X. Wang, J. Yin, L. Gutiérrez-Arzaluz et al., High-performance copper-doped perovskite-related silver halide X-ray imaging scintillator. ACS Energy Lett. **7**(8), 2753–2760 (2022). https://doi.org/10.1021/acsenergylett.2c01484
34. E. Auffray, G. Dosovitskiy, A. Fedorov, I. Guz, M. Korjik et al., Irradiation effects on $Gd_3Al_2Ga_3O_{12}$ scintillators prospective for application in harsh irradiation environments. Radiat. Phys. Chem. **164**, 108365 (2019). https://doi.org/10.1016/j.radphyschem.2019.108365
35. W. Yan, B. Duan, Z. Zhu, Y. Song, G. Song et al., Organic–inorganic hybrid perovskite scintillator for high-resolution X-ray imaging. Nucl. Instrum. Meth. Phys. Res. Sect. B Beam Interact. Mater. At. **546**, 165159 (2024). https://doi.org/10.1016/j.nimb.2023.165159
36. V. Dormenev, K.T. Brinkmann, D. Kazlou, M. Moritz, R.W. Novotny et al., Scintillation properties of garnets and oxyorthosilicates with different dopants. IEEE Trans. Nucl. Sci. **70**(7), 1392–1397 (2023). https://doi.org/10.1109/TNS.2023.3275642
37. F. Maddalena, A. Xie, X.Y. Chin, R. Begum, M.E. Witkowski et al., Deterministic light yield, fast scintillation, and microcolumn structures in lead halide perovskite nanocrystals. J. Phys. Chem. C **125**(25), 14082–14088 (2021). https://doi.org/10.1021/acs.jpcc.1c03392
38. W. Chen, M. Zhou, Y. Liu, X. Yu, C. Pi et al., All-inorganic perovskite polymer–ceramics for flexible and refreshable X-ray imaging. Adv. Funct. Mater. **32**(2), 2107424 (2022). https://doi.org/10.1002/adfm.202107424
39. Y. Li, L. Chen, B. Liu, P. Jin, R. Gao et al., Scintillation performance of two-dimensional perovskite $(BA)_2PbBr_4$ microcrystals. J. Mater. Chem. C **9**(47), 17124–17128 (2021). https://doi.org/10.1039/D1TC04072C
40. W. Shao, X. Wang, Z. Zhang, J. Huang, Z. Han et al., Highly efficient and flexible scintillation screen based on manganese (II) activated 2D perovskite for planar and nonplanar high-resolution X-ray imaging. Adv. Opt. Mater. **10**(6), 2102282 (2022). https://doi.org/10.1002/adom.202102282
41. N. Li, Z. Xu, Y. Xiao, Y. Liu, Z. Yang et al., Flexible, high scintillation yield $Cu_3Cu_2I_5$ film made of ball-milled powder for high spatial resolution X-ray imaging. Adv. Opt. Mater. **10**(5), 2102232 (2022). https://doi.org/10.1002/adom.202102232
42. J.J. van Blaaderen, L.A. van den Brekel, K.W. Krämer, P. Dorenbos, Scintillation and optical characterization of $CsCu_2I_3$ single crystals from 10 to 400 K. Chem. Mater. **35**(22), 9623–9631 (2023). https://doi.org/10.1021/acs.chemmater.3c01810
43. P. Ran, X. Chen, Z. Chen, Y. Su, J. Hui et al., Metal halide CsCu2I3 flexible scintillator with high photodiode spectral compatibility for X-ray cone beam computed tomography (CBCT) imaging. Laser Photonics Rev. **18**(1), 2300743 (2024). https://doi.org/10.1002/lpor.202300743
44. R. Zhang, H. Xie, W. Liu, K. Zhan, H. Liu et al., High-efficiency narrow-band green-emitting manganese(II) halide for multifunctional applications. ACS Appl. Mater. Interfaces **15**(40), 47238–47249 (2023). https://doi.org/10.1021/acsami.3c09518
45. Z. Gong, J. Zhang, X. Deng, M.-P. Ren, W.-Q. Wang et al., Near-unity broadband emissive hybrid manganese bromides as highly-efficient radiation scintillators. Aggregate **5**(5), e574 (2024). https://doi.org/10.1002/agt2.574
46. B. Su, J. Jin, K. Han, Z. Xia, Ceramic wafer scintillation screen by utilizing near-unity blue-emitting lead-free metal halide $(C_8H_20N)_2Cu_2Br_4$. Adv. Funct. Mater. **33**(5), 2210735 (2023). https://doi.org/10.1002/adfm.202210735
47. M. Zhou, H. Jiang, T. Hou, S. Hou, J. Li et al., Inch-size and thickness-adjustable hybrid manganese halide single-crystalline films for high resolution X-ray imaging. Chem. Eng. J. **490**, 151823 (2024). https://doi.org/10.1016/j.cej.2024.151823
48. F. Zhang, Y. Zhou, Z. Chen, M. Wang, Z. Ma et al., Thermally activated delayed fluorescence zirconium-based perovskites for large-area and ultraflexible X-ray scintillator screens. Adv. Mater. **34**(43), 2204801 (2022). https://doi.org/10.1002/adma.202204801
49. H. Wu, Q. Wang, A. Zhang, G. Niu, M. Nikl et al., One-dimensional scintillator film with benign grain boundaries for high-resolution and fast X-ray imaging. Sci. Adv. **9**(30), eadh1789 (2023). https://doi.org/10.1126/sciadv.adh1789
50. Y. Zhou, J. Chen, O.M. Bakr, O.F. Mohammed, Metal halide perovskites for X-ray imaging scintillators and detectors. ACS Energy Lett. **6**(2), 739–768 (2021). https://doi.org/10.1021/acsenergylett.0c02430
51. A. Jana, S. Cho, S.A. Patil, A. Meena, Y. Jo et al., Perovskite: Scintillators, direct detectors, and X-ray imagers. Mater. Today **55**, 110–136 (2022). https://doi.org/10.1016/j.mattod.2022.04.009
52. C. Thalhammer, Improving the light yield and timing resolution of scintillator-based detectors for positron emission tomography. IEEE Trans. Neural Networks Learn. Syst. (2015). https://doi.org/10.1109/tnnls.2023.3323131
53. M. Nikl, A. Yoshikawa, Recent R&D trends in inorganic single-crystal scintillator materials for radiation detection. Adv. Opt. Mater. **3**(4), 463–481 (2015). https://doi.org/10.1002/adom.201400571
54. Y. Wang, M. Li, Z. Chai, Y. Wang, S. Wang, Perovskite scintillators for improved X-ray detection and imaging. Angew. Chem. **135**(38), e202304638 (2023). https://doi.org/10.1002/ange.202304638
55. A. Anand, M.L. Zaffalon, A. Erroi, F. Cova, F. Carulli et al., Advances in perovskite nanocrystals and nanocomposites for

scintillation applications. ACS Energy Lett. **9**(3), 1261–1287 (2024). https://doi.org/10.1021/acsenergylett.3c02763

56. J. Ye, D. Gaur, C. Mi, Z. Chen, I.L. Fernández et al., Strongly-confined colloidal lead-halide perovskite quantum dots: from synthesis to applications. Chem. Soc. Rev. **53**(16), 8095–8122 (2024). https://doi.org/10.1039/D4CS00077C
57. W. Chen, Y. Liu, Z. Yuan, Z. Xu, Z. Zhang et al., X-ray radioluminescence effect of all-inorganic halide perovskite CsPbBr$_3$ quantum dots. J. Radioanal. Nucl. Chem. **314**(3), 2327–2337 (2017). https://doi.org/10.1007/s10967-017-5562-x
58. Q. Chen, J. Wu, X. Ou, B. Huang, J. Almutlaq et al., All-inorganic perovskite nanocrystal scintillators. Nature **561**(7721), 88–93 (2018). https://doi.org/10.1038/s41586-018-0451-1
59. Y. Zhang, R. Sun, X. Ou, K. Fu, Q. Chen et al., Metal halide perovskite nanosheet for X-ray high-resolution scintillation imaging screens. ACS Nano **13**(2), 2520–2525 (2019). https://doi.org/10.1021/acsnano.8b09484
60. W. Ma, T. Jiang, Z. Yang, H. Zhang, Y. Su et al., Highly resolved and robust dynamic X-ray imaging using perovskite glass-ceramic scintillator with reduced light scattering. Adv. Sci. **8**(15), e2003728 (2021). https://doi.org/10.1002/advs.202003728
61. H. Zhang, Z. Yang, M. Zhou, L. Zhao, T. Jiang, H. Yang, Y. Xue, J. Qiu, Reproducible X-ray imaging with a perovskite nanocrystal scintillator embedded in a transparent amorphous network structure. Adv. Mater. (2021). https://doi.org/10.1002/adma.202102529
62. Y. Li, Y. Lei, H. Wang, Z. Jin, Two-dimensional metal halides for X-ray detection applications. Nano-Micro Lett. **15**(1), 128 (2023). https://doi.org/10.1007/s40820-023-01118-1
63. B. Jia, D. Chu, N. Li, Y. Zhang, Z. Yang et al., Airflow-controlled crystallization for a multi-inch 2D halide perovskite single-crystal scintillator for fast high-resolution X-ray imaging. ACS Energy Lett. **8**(1), 590–599 (2023). https://doi.org/10.1021/acsenergylett.2c02196
64. M. Xia, Z. Xie, H. Wang, T. Jin, L. Liu et al., Sub-nanosecond 2D perovskite scintillators by dielectric engineering. Adv. Mater. **35**(18), e2211769 (2023). https://doi.org/10.1002/adma.202211769
65. M.A. Kuddus Sheikh, F. Maddalena, D. Kowal, M. Makowski, S. Mahato et al., Effect of dual-organic cations on the structure and properties of 2D hybrid perovskites as scintillators. ACS Appl. Mater. Interfaces **16**(19), 25529–25539 (2024). https://doi.org/10.1021/acsami.4c01741
66. W. Shao, Q. Li, T. He, Y. Zhang, M. Niu et al., Synergy of organic and inorganic sites in 2D perovskite for fast neutron and X-ray imaging. Adv. Funct. Mater. **33**(40), 2301767 (2023). https://doi.org/10.1002/adfm.202301767
67. W. Zhu, W. Ma, Y. Su, Z. Chen, X. Chen et al., Low-dose real-time X-ray imaging with nontoxic double perovskite scintillators. Light Sci. Appl. **9**, 112 (2020). https://doi.org/10.1038/s41377-020-00353-0
68. Y.-H. Liu, N.-N. Wang, M.-P. Ren, X. Yan, Y.-F. Wu et al., Zero-dimensional hybrid cuprous halide of [BAPMA] Cu$_2$Br$_5$ as a highly efficient light emitter and an X-ray scintillator. ACS Appl. Mater. Interfaces **15**(16), 20219–20227 (2023). https://doi.org/10.1021/acsami.3c00206
69. F. Zhang, Y. Zhou, Z. Chen, X. Niu, H. Wang et al., Large-area X-ray scintillator screen based on cesium hafnium chloride microcrystals films with high sensitivity and stability. Laser Photonics Rev. **17**(5), 2200848 (2023). https://doi.org/10.1002/lpor.202200848
70. L. Zi, J. Song, N. Wang, T. Wang, W. Li et al., X-ray quantum cutting scintillator based on CsPbCl$_x$Br$_3$_x: Y^{b3}+ single crystals. Laser Photonics Rev. **17**(5), 2200852 (2023). https://doi.org/10.1002/lpor.202200852
71. D.-Y. Li, Y.-B. Shang, Q. Liu, H.-W. Zhang, X.-Y. Zhang et al., 0D hybrid indium halide as a highly efficient X-ray scintillation and ultra-sensitive fluorescent probe. Mater. Horiz. **10**(11), 5004–5015 (2023). https://doi.org/10.1039/D3MH00536D
72. S. Wang, W. Huang, X. Liu, S. Wang, H. Ye et al., Ruddlesden–popper perovskite nanocrystals stabilized in mesoporous silica with efficient carrier dynamics for flexible X-ray scintillator. Adv. Funct. Mater. **33**(3), 2210765 (2023). https://doi.org/10.1002/adfm.202210765
73. P. Ran, L. Yang, T. Jiang, X. Xu, J. Hui et al., Multispectral large-panel X-ray imaging enabled by stacked metal halide scintillators. Adv. Mater. **34**(42), e2205458 (2022). https://doi.org/10.1002/adma.202205458
74. X. Wang, X. Zhang, S. Yan, H. Liu, Y. Zhang, Nearly-unity quantum yield and 12-hour afterglow from a transparent perovskite of Cs$_2$NaScCl$_6$: Tb. Angew. Chem. Int. Ed. **134**(40), e202210853 (2022). https://doi.org/10.1002/ange.202210853
75. Z. Zhang, Q. Han, J.W. Lau, B. Xing, Lanthanide-doped upconversion nanoparticles meet the needs for cutting-edge bioapplications: recent progress and perspectives. ACS Mater. Lett. **2**(11), 1516–1531 (2020). https://doi.org/10.1021/acsmaterialslett.0c00377
76. L. Han, B. Sun, C. Guo, G. Peng, H. Chen et al., Photophysics in zero-dimensional potassium-doped cesium copper chloride Cs$_3$Cu$_2$Cl$_5$ nanosheets and its application for high-performance flexible X-Ra$_y$ detection. Adv. Opt. Mater. **10**(6), 2102453 (2022). https://doi.org/10.1002/adom.202102453
77. W. Chen, T. Wang, T. Wang, J. Yu, S. Yao et al., Customizable scintillator of Cs$_3$Cu$_2$I$_5$: 2% In$^+$ @Paper for large-area X-ray imaging. Adv. Sci. **10**(34), e2304957 (2023). https://doi.org/10.1002/advs.202304957
78. V. Naresh, P.-R. Cha, N. Lee, Cs$_2$NaGdCl$_6$: Tb^{3+}—A highly luminescent rare-earth double perovskite scintillator for low-dose X-ray detection and imaging. ACS Appl. Mater. Interfaces **16**(15), 19068–19080 (2024). https://doi.org/10.1021/acsami.3c17301
79. W. Li, L. Yuan, H. Wu, Y. Jin, Tb^{3+}-doped a zero-dimensional all-inorganic metal halide perovskite scintillator Cs$_2$ScCl$_5$·H$_2$O for X-ray imaging. Opt. Mater. **157**, 116130 (2024). https://doi.org/10.1016/j.optmat.2024.116130
80. J. Shi, Z. Wang, L. Xu, J. Wang, Z. Da et al., *In situ* growth of lead-free double perovskite micron sheets in polymethyl

© The authors

methacrylate for X-ray imaging. Adv. Opt. Mater. **12**(22), 2400691 (2024). https://doi.org/10.1002/adom.202400691

81. Y.-Y. Wang, W.-T. Song, X.-R. Yao, X.-Y. Chen, M.-T. Cheng et al., A new polar lead-free hybrid halide X-ray scintillator. Adv. Opt. Mater. **12**(22), 2400190 (2024). https://doi.org/10.1002/adom.202400190
82. T. Feng, Z.-A. Zhou, Y.-N. An, L. Chen, Y. Fu et al., Large-area transparent antimony-based perovskite glass for high-resolution X-ray imaging. ACS Nano **18**(26), 16715–16725 (2024). https://doi.org/10.1021/acsnano.4c01761
83. J. Li, Q. Hu, J. Xiao, Z.-G. Yan, High-stability double perovskite scintillator for flexible X-ray imaging. J. Colloid Interface Sci. **671**, 725–731 (2024). https://doi.org/10.1016/j.jcis.2024.05.203
84. Y. Zhang, K. Li, L. Niu, J. Ren, X. Liu et al., Eu^{2+} doped cesium alkaline earth chloride nanocrystals in glass for X-ray imaging. Ceram. Int. **50**(17), 31673–31679 (2024). https://doi.org/10.1016/j.ceramint.2024.05.475
85. W. Bu, Y. Yan, P. Liu, T. Wang, S. Wang et al., *In-situ* growth of $Cs_5Cu_3Cl_6I_2$ nanocrystals within AAO arrays for X-ray imaging. Chem. Eng. J. **492**, 151908 (2024). https://doi.org/10.1016/j.cej.2024.151908
86. Y. Zhang, M. Shen, B. Cheng, W. Ma, X. Huang et al., Ultrafast scintillation at room temperature achieved in $CsPbCl_3$-based single crystals through Br over-doping. J. Mater. Chem. C **12**(20), 7169–7175 (2024). https://doi.org/10.1039/D4TC00880D
87. J.-A. Lai, P. Wang, B. Zheng, T. Xuan, D. Wu et al., Enhanced performance in cesium tellurium chlorine by hafnium alloying for X-ray computed tomography imaging. Adv. Opt. Mater. **12**(17), 2303297 (2024). https://doi.org/10.1002/adom.202303297
88. Y. Wang, C. Wang, L. Men, Q. Hu, J. Xiao, Colloidal synthesis of hollow double perovskite nanocrystals and their applications in X-ray imaging. Inorg. Chem. **63**(12), 5734–5742 (2024). https://doi.org/10.1021/acs.inorgchem.4c00280
89. J. Qiu, H. Zhao, Z. Mu, J. Chen, H. Gu et al., Turning nonemissive $CsPb_2Br_5$ crystals into high-performance scintillators through alkali metal doping. Nano Lett. **24**(8), 2503–2510 (2024). https://doi.org/10.1021/acs.nanolett.3c04455
90. W. Xiang, D. Shen, X. Zhang, X. Li, Y. Liu et al., Transparent and planar $Cs_3Cu_2Cl_5$ crystals for micrometer-resolution X-ray imaging screen. ACS Appl. Mater. Interfaces **16**(4), 4918–4924 (2024). https://doi.org/10.1021/acsami.3c15764
91. M. Wang, X. Qing, T. Du, C. Wu, X. Han, $Te4^+$-doped Cs_2SnCl_6 scintillator for flexible and efficient X-ray imaging screens. J. Mater. Chem. C **12**(6), 2241–2246 (2024). https://doi.org/10.1039/D3TC03818A
92. N. Liu, J. Luo, Q. Guo, P. Du, L. Gao et al., Reduced self-absorption of quasi-2D perovskites and their application in color conversion layers. Adv. Opt. Mater. **11**(1), 2202118 (2023). https://doi.org/10.1002/adom.202202118
93. T. Haposan, A. Arramel, P.Y.D. Maulida, S. Hartati, A.A. Afkauni et al., All-inorganic copper-halide perovskites for large-Stokes shift and ten-nanosecond-emission scintillators. J. Mater. Chem. C **12**(7), 2398–2409 (2024). https://doi.org/10.1039/D3TC03977C
94. S. Cheng, M. Nikl, A. Beitlerova, R. Kucerkova, X. Du et al., Ultrabright and highly efficient all-inorganic zero-dimensional perovskite scintillators. Adv. Opt. Mater. **9**(13), 2100460 (2021). https://doi.org/10.1002/adom.202100460
95. W.J. Mir, Y. Mahor, A. Lohar, M. Jagadeeswararao, S. Das et al., Postsynthesis doping of Mn and Yb into $CsPbX_3$ (X = Cl, Br, or I) perovskite nanocrystals for downconversion emission. Chem. Mater. **30**(22), 8170–8178 (2018). https://doi.org/10.1021/acs.chemmater.8b03066
96. V. Pinchetti, A. Anand, Q.A. Akkerman, D. Sciacca, M. Lorenzon et al., Trap-mediated two-step sensitization of manganese dopants in perovskite nanocrystals. ACS Energy Lett. **4**(1), 85–93 (2019). https://doi.org/10.1021/acsenergylett.8b02052
97. W. Liu, Q. Lin, H. Li, K. Wu, I. Robel et al., Mn^{2+}-doped lead halide perovskite nanocrystals with dual-color emission controlled by halide content. J. Am. Chem. Soc. **138**(45), 14954–14961 (2016). https://doi.org/10.1021/jacs.6b08085
98. S. Das Adhikari, A.K. Guria, N. Pradhan, Insights of doping and the photoluminescence properties of Mn-doped perovskite nanocrystals. J. Phys. Chem. Lett. **10**(9), 2250–2257 (2019). https://doi.org/10.1021/acs.jpclett.9b00182
99. S. Paul, E. Bladt, A.F. Richter, M. Döblinger, Y. Tong et al., Manganese-doping-induced quantum confinement within host perovskite nanocrystals through ruddlesden–popper defects. Angew. Chem. Int. Ed. **59**(17), 6794–6799 (2020). https://doi.org/10.1002/anie.201914473
100. G. Huang, C. Wang, S. Xu, S. Zong, J. Lu et al., Postsynthetic doping of $MnCl_2$ molecules into preformed $CsPbBr_3$ perovskite nanocrystals *via* a halide exchange-driven cation exchange. Adv. Mater. **29**(29), 1700095 (2017). https://doi.org/10.1002/adma.201700095
101. H. Xu, W. Liang, Z. Zhang, C. Cao, W. Yang et al., 2D perovskite Mn^{2+}-doped $Cs_2CdBr_2Cl_2$ scintillator for low-dose high-resolution X-ray imaging. Adv. Mater. **35**(26), e2300136 (2023). https://doi.org/10.1002/adma.202300136
102. K. Li, W. Zhang, L. Niu, Y. Ye, J. Ren et al., Lead-free cesium manganese halide nanocrystals embedded glasses for X-ray imaging. Adv. Sci. **10**(4), 2204843 (2023). https://doi.org/10.1002/advs.202204843
103. D.J. Kiebala, R. Style, D. Vanhecke, C. Calvino, C. Weder et al., Sub-micrometer mechanochromic inclusions enable strain sensing in polymers. Adv. Funct. Mater. **33**(50), 2304938 (2023). https://doi.org/10.1002/adfm.202304938
104. B. Wang, X. Ouyang, X. He, Z. Deng, Y. Zhou et al., High-resolution X-ray imaging of Mn enhanced lead-free halide scintillators in pixelated array structures. Adv. Opt. Mater. **11**(17), 2300388 (2023). https://doi.org/10.1002/adom.202300388
105. N. Varnakavi, R. Rajavaram, K. Gupta, P.-R. Cha, N. Lee, Scintillation performance of Mn(II)-doped $Cs_2NaBiCl_6$ double perovskite nanocrystals for X-Ra_y imaging applications. Adv. Opt. Mater. **12**(9), 2301868 (2024). https://doi.org/10.1002/adom.202301868

106. C. Wang, Z.-G. Yan, Y. Wang, J. Zhu, C. Peng et al., All-inorganic ruddlesden–popper perovskite Cs_2CdCl_4: Mn for low-dose and flexible X-ray imaging. ACS Mater. Lett. **6**(4), 1429–1438 (2024). https://doi.org/10.1021/acsmaterialslett.3c01665

107. P. Pei, R. Wei, B. Wang, J. Su, Z. Zhang et al., An advanced tunable multimodal luminescent La_4GeO_8: Eu^{2+}, Er^{3+} phosphor for multicolor anticounterfeiting. Adv. Funct. Mater. **31**(31), 2102479 (2021). https://doi.org/10.1002/adfm.202102479

108. M.P. Davydova, L. Meng, M.I. Rakhmanova, Z. Jia, A.S. Berezin et al., Strong magnetically-responsive circularly polarized phosphorescence and X-ray scintillation in ultrarobust Mn(II)–organic helical chains. Adv. Mater. **35**(35), 2303611 (2023). https://doi.org/10.1002/adma.202303611

109. H. Tang, Z. Jia, Y. Xu, Y. Liu, Q. Lin, Enhanced photoluminescence quantum yield of metal halide perovskite microcrystals for multiple optoelectronic applications. Small **20**(4), 2304336 (2024). https://doi.org/10.1002/smll.202304336

110. Z. Wang, Y. Wei, C. Liu, Y. Liu, M. Hong, Mn^{2+}-activated $Cs_3Cu_2I_5$ nano-scintillators for ultra-high resolution flexible X-Ra_y imaging. Laser Photonics Rev. **17**(6), 2200851 (2023). https://doi.org/10.1002/lpor.202200851

111. L. Li, Z. Fan, J. Zhang, D. Fan, X. Liu et al., Yellow emissive $CsCu_2I_3$ nanocrystals induced by Mn^{2+} for high-resolution X-ray imaging. Inorg. Chem. **62**(49), 19848–19855 (2023). https://doi.org/10.1021/acs.inorgchem.3c03724

112. J. Barrio, A. Pedersen, S.C. Sarma, A. Bagger, M. Gong et al., FeNC oxygen reduction electrocatalyst with high utilization penta-coordinated sites. Adv. Mater. **35**(14), e2211022 (2023). https://doi.org/10.1002/adma.202211022

113. J.-X. Zheng, Z.-A. Zhou, T. Feng, H. Li, C.-H. Sun et al., Hydrophobic long-chain two-dimensional perovskite scintillators for underwater X-ray imaging. Rare Met. **43**(1), 175–185 (2024). https://doi.org/10.1007/s12598-023-02421-x

114. N. Kawano, M. Akatsuka, H. Kimura, D. Nakauchi, T. Kato et al., Scintillation properties of Mn-doped methylammonium lead chloride crystals. J. Mater. Sci. Mater. Electron. **32**(10), 12903–12910 (2021). https://doi.org/10.1007/s10854-020-04480-7

115. X. Li, H. Guo, Y. Li, C. Lin, L. Xie, Enhancing persistent radioluminescence in perovskite scintillators through trap defect modulation. Mater. Chem. Front. **8**(13), 2539–2548 (2024). https://doi.org/10.1039/D4QM00039K

116. B. Su, K. Han, Z. Xia, Mn^{2+}-doped Cs_2ZnBr_4 scintillator for X-ray imaging. J. Mater. Chem. C **11**(24), 8052–8061 (2023). https://doi.org/10.1039/D2TC04249E

117. K.E. Yorov, W.J. Mir, X. Song, L. Gutiérrez-Arzaluz, R. Naphade et al., Mn^{4+}-doped fluoride nanocrystals enable high-resolution red-emitting X-ray imaging screens. ACS Mater. Lett. **4**(11), 2273–2281 (2022). https://doi.org/10.1021/acsmaterialslett.2c00746

118. L.-J. Xu, X. Lin, Q. He, M. Worku, B. Ma, Highly efficient eco-friendly X-ray scintillators based on an organic manganese halide. Nat. Commun. **11**(1), 4329 (2020). https://doi.org/10.1038/s41467-020-18119-y

119. J. Jin, K. Han, Y. Hu, Z. Xia, Zn^{2+} doping in organic manganese(II) bromide hybrid scintillators toward enhanced light yield for X-ray imaging. Adv. Opt. Mater. **11**(14), 2300330 (2023). https://doi.org/10.1002/adom.202300330

120. J. Zhang, X. Wang, W.-Q. Wang, X. Deng, C.-Y. Yue et al., Near-unity green luminescent hybrid manganese halides as X-ray scintillators. Inorg. Chem. **63**(5), 2647–2654 (2024). https://doi.org/10.1021/acs.inorgchem.3c03924

121. X. Wang, X. Zhang, Y. Liu, Y. Zhang, Shape-on-demand synthesis of luminescent $(ETP)_2MnBr_4$ glass scintillator. Chem. Eng. J. **483**, 149239 (2024). https://doi.org/10.1016/j.cej.2024.149239

122. Y. Xu, Z. Li, G. Peng, F. Qiu, Z. Li et al., Organic cation design of manganese halide hybrids glass toward low-temperature integrated efficient, scaling, and reproducible X-ray detector. Adv. Opt. Mater. **11**(13), 2300216 (2023). https://doi.org/10.1002/adom.202300216

123. S. Wang, S. Feng, R. Li, J. Jin, J. Wu et al., Multiexciton generation from a 2D organic-inorganic hybrid perovskite with nearly 200% quantum yield of red phosphorescence. Adv. Mater. **35**(18), e2211992 (2023). https://doi.org/10.1002/adma.202211992

124. F. Montanarella, K.M. McCall, K. Sakhatskyi, S. Yakunin, P. Trtik et al., Highly concentrated, zwitterionic ligand-capped Mn^{2+}: $CsPb(Br_xCl_{1-x})_3$ nanocrystals as bright scintillators for fast neutron imaging. ACS Energy Lett. **6**(12), 4365–4373 (2021). https://doi.org/10.1021/acsenergylett.1c01923

125. F. Wang, X. Liu, Multicolor tuning of lanthanide-doped nanoparticles by single wavelength excitation. Acc. Chem. Res. **47**(4), 1378–1385 (2014). https://doi.org/10.1021/ar5000067

126. Y. Wu, W. Wu, Combinations of superior inorganic phosphors for level-tunable information hiding and encoding. Adv. Opt. Mater. **9**(17), 2100281 (2021). https://doi.org/10.1002/adom.202100281

127. B. Liu, C. Li, P. Yang, Z. Hou, J. Lin, 808-nm-light-excited lanthanide-doped nanoparticles: rational design, luminescence control and theranostic applications. Adv. Mater. **29**(18), 1605434 (2017). https://doi.org/10.1002/adma.201605434

128. G. Gao, A. Turshatov, I.A. Howard, D. Busko, R. Joseph et al., Up-conversion fluorescent labels for plastic recycling: a review. Adv. Sustain. Syst. **1**(5), 1600033 (2017). https://doi.org/10.1002/adsu.201600033

129. L. Lei, Y. Wang, A. Kuzmin, Y. Hua, J. Zhao et al., Next generation lanthanide doped nanoscintillators and photon converters. eLight **2**(1), 17 (2022). https://doi.org/10.1186/s43593-022-00024-0

130. G. Pan, X. Bai, D. Yang, X. Chen, P. Jing et al., Doping lanthanide into perovskite nanocrystals: highly improved and expanded optical properties. Nano Lett. **17**(12), 8005–8011 (2017). https://doi.org/10.1021/acs.nanolett.7b04575

131. M. Gandini, I. Villa, M. Beretta, C. Gotti, M. Imran et al., Efficient, fast and reabsorption-free perovskite nanocrystal-based sensitized plastic scintillators. Nat. Nanotechnol. **15**(6), 462–468 (2020). https://doi.org/10.1038/s41565-020-0683-8

132. Z. Wang, S. Li, G. Ren, S. Yao, D. Zhu et al., Flexible and reabsorption-free perovskite scintillators for low-dose X-ray detection and high-resolution imaging. ACS Photonics **11**(8), 3003–3011 (2024). https://doi.org/10.1021/acsphotonics.4c00117
133. Z. Yang, J. Yao, L. Xu, W. Fan, J. Song, Designer bright and fast $CsPbBr_3$ perovskite nanocrystal scintillators for high-speed X-ray imaging. Nat. Commun. **15**(1), 8870 (2024). https://doi.org/10.1038/s41467-024-53263-9
134. H. Si, Z. Zhang, Q. Liao, G. Zhang, Y. Ou et al., A-site management for highly crystalline perovskites. Adv. Mater. **32**(4), e1904702 (2020). https://doi.org/10.1002/adma.201904702
135. W.-G. Li, X.-D. Wang, Y.-H. Huang, D.-B. Kuang, Ultrasound-assisted crystallization enables large-area perovskite quasi-monocrystalline film for high-sensitive X-ray detection and imaging. Adv. Mater. **35**(31), 2210878 (2023). https://doi.org/10.1002/adma.202210878
136. Z. Xiao, Q. Dong, C. Bi, Y. Shao, Y. Yuan et al., Solvent annealing of perovskite-induced crystal growth for photovoltaic-device efficiency enhancement. Adv. Mater. **26**(37), 6503–6509 (2014). https://doi.org/10.1002/adma.201401685
137. J. Zhang, W. Liang, W. Yu, S. Yu, Y. Wu et al., A two-stage annealing strategy for crystallization control of $CH_3NH_3PbI_3$ films toward highly reproducible perovskite solar cells. Small **14**(26), 1800181 (2018). https://doi.org/10.1002/smll.201800181
138. S. Cui, J. Wang, H. Xie, Y. Zhao, Z. Li et al., Rubidium ions enhanced crystallinity for ruddlesden-popper perovskites. Adv. Sci. **7**(24), 2002445 (2020). https://doi.org/10.1002/advs.202002445
139. V. Naresh, S. Singh, H. Soh, J. Lee, N. Lee, Dual-phase $CsPbBr_3$–CsPb2Br5 perovskite scintillator for sensitive X-ray detection and imaging. Mater. Today Nano **23**, 100364 (2023). https://doi.org/10.1016/j.mtnano.2023.100364
140. V.B. Mykhaylyk, H. Kraus, M. Saliba, Bright and fast scintillation of organolead perovskite $MAPbBr_3$ at low temperatures. Mater. Horiz. **6**(8), 1740–1747 (2019). https://doi.org/10.1039/C9MH00281B
141. S. Mahato, M. Makowski, S. Bose, D. Kowal, M.A. Kuddus Sheikh et al., Improvement of light output of MAPbBr 3 single crystal for ultrafast and bright cryogenic scintillator. J. Phys. Chem. Lett. **15**(14), 3713–3720 (2024). https://doi.org/10.1021/acs.jpclett.4c00379
142. S. Kishimoto, K. Shibuya, F. Nishikido, M. Koshimizu, R. Haruki et al., Subnanosecond time-resolved X-ray measurements using an organic-inorganic perovskite scintillator. Appl. Phys. Lett. **93**(26), 261901 (2008). https://doi.org/10.1063/1.3059562
143. X. Ou, X. Qin, B. Huang, J. Zan, Q. Wu et al., High-resolution X-ray luminescence extension imaging. Nature **590**(7846), 410–415 (2021). https://doi.org/10.1038/s41586-021-03251-6
144. X. Zhou, K. Han, Y. Wang, J. Jin, S. Jiang et al., Energy-trapping management in X-ray storage phosphors for flexible 3D imaging. Adv. Mater. **35**(16), e2212022 (2023). https://doi.org/10.1002/adma.202212022
145. L. Lu, S. Peng, L. Zhao, M. Zhang, J. Xiao et al., Visualized X-ray dosimetry for multienvironment applications. Nano Lett. **23**(18), 8753–8760 (2023). https://doi.org/10.1021/acs.nanolett.3c02826
146. N. Zhang, R. Zhang, X. Xu, F. Wang, Z. Sun et al., X-ray-activated long afterglow double-perovskite scintillator for detection and extension imaging. Adv. Opt. Mater. **11**(16), 2300187 (2023). https://doi.org/10.1002/adom.202300187
147. W. Bian, Y. Lin, T. Wang, X. Yu, J. Qiu et al., Direct identification of surface defects and their influence on the optical characteristics of upconversion nanoparticles. ACS Nano **12**(4), 3623–3628 (2018). https://doi.org/10.1021/acsnano.8b00741
148. C. Wang, X. Mao, Z. Wang, X. Xu, W. Guo et al., Synthesis and exciton dynamics of a one-dimensional organic copper halide perovskite. J. Phys. Chem. C **126**(10), 4959–4964 (2022). https://doi.org/10.1021/acs.jpcc.1c10402
149. W. Shao, T. He, J.-X. Wang, Y. Zhou, P. Yuan et al., Transparent organic and metal halide tandem scintillators for high-resolution dual-energy X-ray imaging. ACS Energy Lett. **8**(6), 2505–2512 (2023). https://doi.org/10.1021/acsenergylett.3c00784
150. X. Hu, S. Luo, J. Leng, C. Wang, Y. Chen et al., Density-discriminating chromatic X-ray imaging based on metal halide nanocrystal scintillators. Sci. Adv. **9**(37), eadh5081 (2023). https://doi.org/10.1126/sciadv.adh5081
151. J. Hui, P. Ran, Y. Su, L. Yang, X. Xu et al., Stacked scintillators based multispectral X-ray imaging featuring quantum-cutting perovskite scintillators with 570 nm absorption-emission shift. Adv. Mater. **37**(10), e2416360 (2025). https://doi.org/10.1002/adma.202416360
152. J. Pang, S. Zhao, X. Du, H. Wu, G. Niu et al., Vertical matrix perovskite X-ray detector for effective multi-energy discrimination. Light Sci. Appl. **11**(1), 105 (2022). https://doi.org/10.1038/s41377-022-00791-y
153. B. Shabbir, J.C. Yu, T. Warnakula, R.A.W. Ayyubi, J.A. Pollock et al., Printable perovskite diodes for broad-spectrum multienergy X-ray detection. Adv. Mater. **35**(20), e2210068 (2023). https://doi.org/10.1002/adma.202210068
154. W. Shao, T. He, L. Wang, J.-X. Wang, Y. Zhou et al., Capillary manganese halide needle-like array scintillator with isolated light crosstalk for micro-X-ray imaging. Adv. Mater. **36**(21), 2312053 (2024). https://doi.org/10.1002/adma.202312053
155. X. Zhao, T. Jin, W. Gao, G. Niu, J. Zhu et al., Embedding $Cs_3Cu_2I_5$ scintillators into anodic aluminum oxide matrix for high-resolution X-Ra_y imaging. Adv. Opt. Mater. **9**(24), 2101194 (2021). https://doi.org/10.1002/adom.202101194
156. H. Li, H. Yang, R. Yuan, Z. Sun, Y. Yang et al., Ultrahigh spatial resolution, fast decay, and stable X-Ra_y scintillation screen through assembling $CsPbBr_3$ nanocrystals arrays in anodized aluminum oxide. Adv. Opt. Mater. **9**(24), 2101297 (2021). https://doi.org/10.1002/adom.202101297
157. W.E. van Eijk Carel, Inorganic scintillators in medical imaging. Phys. Med. Biol. **47**(8), R85–R106 (2002). https://doi.org/10.1088/0031-9155/47/8/201

158. J. Hui, P. Ran, Y. Su, L. Yang, X. Xu et al., High-resolution X-ray imaging based on solution-phase-synthesized $Cs_3Cu_2I_5$ scintillator nanowire array. J. Phys. Chem. C **126**(30), 12882–12888 (2022). https://doi.org/10.1021/acs.jpcc.2c03453
159. M. Li, Y. Wang, L. Yang, Z. Chai, Y. Wang et al., Circularly polarized radioluminescence from chiral perovskite scintillators for improved X-ray imaging. Angew. Chem. Int. Ed. **134**(37), e202208440 (2022). https://doi.org/10.1002/ange.202208440
160. M. Wang, X. Wang, B. Zhang, F. Li, H. Meng et al., Chiral hybrid manganese(ii) halide clusters with circularly polarized luminescence for X-ray imaging. J. Mater. Chem. C **11**(9), 3206–3212 (2023). https://doi.org/10.1039/D2TC05379A
161. M.P. Davydova, L. Meng, M.I. Rakhmanova, I.Y. Bagryanskaya, V.S. Sulyaeva et al., Highly emissive chiral Mn(II) bromide hybrids for UV-pumped circularly polarized LEDs and scintillator image applications. Adv. Opt. Mater. **11**(8), 2202811 (2023). https://doi.org/10.1002/adom.202202811
162. J. Wu, S. You, P. Yu, Q. Guan, Z.-K. Zhu et al., Chirality inducing polar photovoltage in a 2D lead-free double perovskite toward self-powered X-ray detection. ACS Energy Lett. **8**(6), 2809–2816 (2023). https://doi.org/10.1021/acsenergylett.3c00629
163. S. Cho, S. Kim, J. Kim, Y. Jo, I. Ryu et al., Hybridisation of perovskite nanocrystals with organic molecules for highly efficient liquid scintillators. Light Sci. Appl. **9**, 156 (2020). https://doi.org/10.1038/s41377-020-00391-8
164. T. Jiang, W. Ma, H. Zhang, Y. Tian, G. Lin et al., Highly efficient and tunable emission of lead-free manganese halides toward white light-emitting diode and X-ray scintillation applications. Adv. Funct. Mater. **31**(14), 2009973 (2021). https://doi.org/10.1002/adfm.202009973
165. Y. Wei, H. Ebendorff-Heidepriem, J. Zhao, Recent advances in hybrid optical materials: integrating nanoparticles within a glass matrix. Adv. Opt. Mater. **7**(21), 1900702 (2019). https://doi.org/10.1002/adom.201900702
166. J. Nie, C. Li, S. Zhou, J. Huang, X. Ouyang et al., High photoluminescence quantum yield perovskite/polymer nanocomposites for high contrast X-ray imaging. ACS Appl. Mater. Interfaces **13**(45), 54348–54353 (2021). https://doi.org/10.1021/acsami.1c15613
167. B. Wang, P. Li, Y. Zhou, Z. Deng, X. Ouyang et al., $Cs_3Cu_2I_5$ perovskite nanoparticles in polymer matrix as large-area scintillation screen for high-definition X-ray imaging. ACS Appl. Nano Mater. **5**(7), 9792–9798 (2022). https://doi.org/10.1021/acsanm.2c01996
168. A. Giuri, A.C. Chekkallur, M. Calora, R. Mastria, L. Martinazzoli et al., 3D printed ultra-fast plastic scintillators based on perovskite-photocurable polymer composite. Adv. Funct. Mater. **35**(12), 2417653 (2025). https://doi.org/10.1002/adfm.202417653
169. X. Wu, Z. Guo, S. Zhu, B. Zhang, S. Guo et al., Ultrathin, transparent, and high density perovskite scintillator film for high resolution X-ray microscopic imaging. Adv. Sci. **9**(17), e2200831 (2022). https://doi.org/10.1002/advs.202200831
170. K. Han, K. Sakhatskyi, J. Jin, Q. Zhang, M.V. Kovalenko et al., Seed-crystal-induced cold sintering toward metal halide transparent ceramic scintillators. Adv. Mater. **34**(17), e2110420 (2022). https://doi.org/10.1002/adma.202110420
171. X. Hao, L. Nie, X. Zhu, G. Zeng, C. Liu et al., High-resolution X-ray image from copper-based perovskite hybrid polymer. ACS Appl. Mater. Interfaces **16**(22), 29210–29216 (2024). https://doi.org/10.1021/acsami.4c03401
172. B. Li, Y. Xu, X. Zhang, K. Han, J. Jin et al., Zero-dimensional luminescent metal halide hybrids enabling bulk transparent medium as large-area X-ray scintillators. Adv. Opt. Mater. **10**(10), 2102793 (2022). https://doi.org/10.1002/adom.202102793
173. A.J.J.M. van Breemen, M. Simon, O. Tousignant, S. Shanmugam, J.-L. van der Steen et al., Curved digital X-ray detectors. NPJ Flex. Electron. **4**, 22 (2020). https://doi.org/10.1038/s41528-020-00084-7
174. Y. Zhou, X. Wang, T. He, H. Yang, C. Yang et al., Large-area perovskite-related copper halide film for high-resolution flexible X-ray imaging scintillation screens. ACS Energy Lett. **7**(2), 844–846 (2022). https://doi.org/10.1021/acsenergylett.2c00075
175. L. Lian, X. Wang, P. Zhang, J. Zhu, X. Zhang et al., Highly luminescent zero-dimensional organic copper halides for X-ray scintillation. J. Phys. Chem. Lett. **12**(29), 6919–6926 (2021). https://doi.org/10.1021/acs.jpclett.1c01946
176. W. Li, Y. Li, Y. Wang, Z. Zhou, C. Wang et al., Highly efficient and flexible scintillation screen based on organic Mn(II) halide hybrids toward planar and nonplanar X-ray imaging. Laser Photonics Rev. **18**(2), 2300860 (2024). https://doi.org/10.1002/lpor.202300860

Publisher's Note Springer Nature remains neutral with regard to jurisdictional claims in published maps and institutional affiliations.